Mathematical Modelling of Membrane Filtration

Armin Ulrich Krupp
Mansfield College
University of Oxford

A thesis submitted for the degree of
Doctor of Philosophy

Trinity 2017

Dedication

To my parents, Helga and Ulrich, without their selflessness, dedication, and support none of this would have been possible.

To Eric, Gerhard, Richard, and Sandra, for being my best friends.

To Maline, for making me happy.

Acknowledgements

I am not sure why my two supervisors Colin Please and Ian Griffiths decided to take me on as a DPhil student back in May 2013 and I suspect they have asked themselves this question many a time during the past four years. Whatever their reasons, I am glad they did, because I could not have hoped for more supportive, engaged, and dedicated supervisors (remember Skype meetings on New Year's eve or thesis-reading during your vacation?). They provided me with room to try out new ideas, encouragement when things were not working, and shared the joy and excitement when they did. For this and so much more, I am extremely grateful.

I would like to thank EPSRC, the Mathematical Institute, and my industrial sponsor, Pall Europe, for enabling this DPhil. Membrane filtration is not a topic immediately associated with applied mathematics, but I am glad that they had the courage to support a mathematician notwithstanding. In particular, I would like to thank Peter Levison for being a champion of our cause within Pall. I would like to thank Anil Kumar for the initiative, discussions, and feedback that made my first publication a reality. Thanks also go out to Mark Hurwitz, for discussions, insights, and the study groups.

Getting to Oxford would have never been possible without the support back in Munich and Cambridge. In particular, I would like to thank Andreas Bogner (formerly Würfl), Anusch Taraz, Carl-Friedrich Kreiner, and Martin Brokate, for showing me a path to mathematical research. I would like to thank Carola-Bibiane Schönlieb for posing and supervising my Part III essay, it taught me so much. I am sorry I joined the applied side.

To my friends from Munich, Anna, Lena, Martin, Markus, Saskia, Stefan, Tobi, who still make me feel at home even I though I only stayed for three years and left five years ago, and to my friends who are, or have been, in Oxford, Adrien, Ali C., Ali R., Alma, Atamli, Chloe, Citlali, Darren, Finn, Giles, Glenn, Hannah, Henriette, Ines, James, Jonathan, Lawrence, Luke, Marijn, Merel, Moritz, Nina, Shannon, and

Xiamyra, for making this place a new home. Here is also to my fellow members of Mansfield College Boat Club, I loved every single minute of it.

To Inga, for sharing the journey during school, university, and for encouraging me to go to Oxford. I am forever grateful for all the support, encouragement, and simply being there during those years.

Here is to Alexander, Felix, Matthias, Nikola, Ousmane, Thibaut, and Tim, you have made the last years special. And to Andreas and Daniel, I am so glad you came to the UK.

And most importantly, thank you, Maline. I could not have done it without you.

Abstract

In this thesis, we consider four different problems in membrane filtration, using a different mathematical approach in each instance.

We account for the fluid-driven deformation of a filtercake using nonlinear poroelasticity in Chapter 2. By considering feeds with very high and very low particle concentrations, we introduce a quasi-static caking model that provides a suitable approximation to the full model for the physically realistic concentration regimes. We illustrate the agreements and differences between our model and the existing conventional cake-filtration law.

In Chapter 3, we introduce a stochastic model for membrane filtration based on the quantised nature of the particles and show how it can be applied for feeds with different particle types and membranes with an interconnected pore structure. This allows us to understand the relation between the effects of clogging on the level of an individual pore and on the macroscopic level of the entire membrane. We conclude by explaining the transition between the discrete and continuous model based on the Fokker–Planck equation.

In Chapter 4, we consider the inverse problem of determining the underlying filtration law from the spreading speed of a particle-laden gravity current. We first couple the theory of gravity currents with the stochastic model developed in Chapter 3 to determine a filtration law from a given set of experiments. We then generalise this idea for the porous medium equation, where we show that the position of the front follows a power law for the conventional filtration laws, which allows us to infer the clogging law in certain instances.

We conclude the thesis by showing in Chapter 5 how we can combine experimental measurements for the clogging of a depth filter and simple fluid dynamics to accurately predict the pressure distribution in a multi-capsule depth filter during a filtration run.

Contents

List of Figures

Chapter 1

Introduction

1.1 Motivation

Separation, purification, and concentration tasks are integral to various industrial processes and are accomplished by a range of techniques including centrifugation, distillation, and membrane filtration [32]. Membranes are selective barriers where particles are retained either due to size exclusion effects, termed *steric effects*, or due to electrochemical repulsions [80]. Membrane filtration has become the method of choice in various applications for separations based on particle size and shape, with length scales ranging from a few nanometres in water desalination [78] to several microns in bioseparations [118]. This is not only due to its economic advantage over other separation techniques due to lower energy costs, but membrane filtration is, for example, also better suited to preserve the quality of the product in the food and beverage industry than other purification processes [25].

Membrane filters can be operated either in a *dead-end filtration* (also known as *normal-flow filtration*) configuration, where the *feed* flows orthogonally into the membrane, in *cross-flow filtration* configuration, where the feed flows parallel to the membrane, or in *direct-flow filtration* configuration, which is a combination of the two previous modes, see figure 1.1. The filtered liquid is termed *permeate*, the retained liquid *retentate*. Direct-flow filtration and especially cross-flow filtration offer several benefits compared to normal-flow filtration when operated at the right conditions [38]. Nevertheless, normal-flow setups are widely used, especially when the concentration of particles in the feed is low, since this method is cheaper, simpler to operate, and more energy efficient [17]. For industrial operations, large membrane areas are required and so membranes are arranged into more complex configurations, see figure 1.2, and then operated as normal-, cross-, or direct-flow filtration [87].

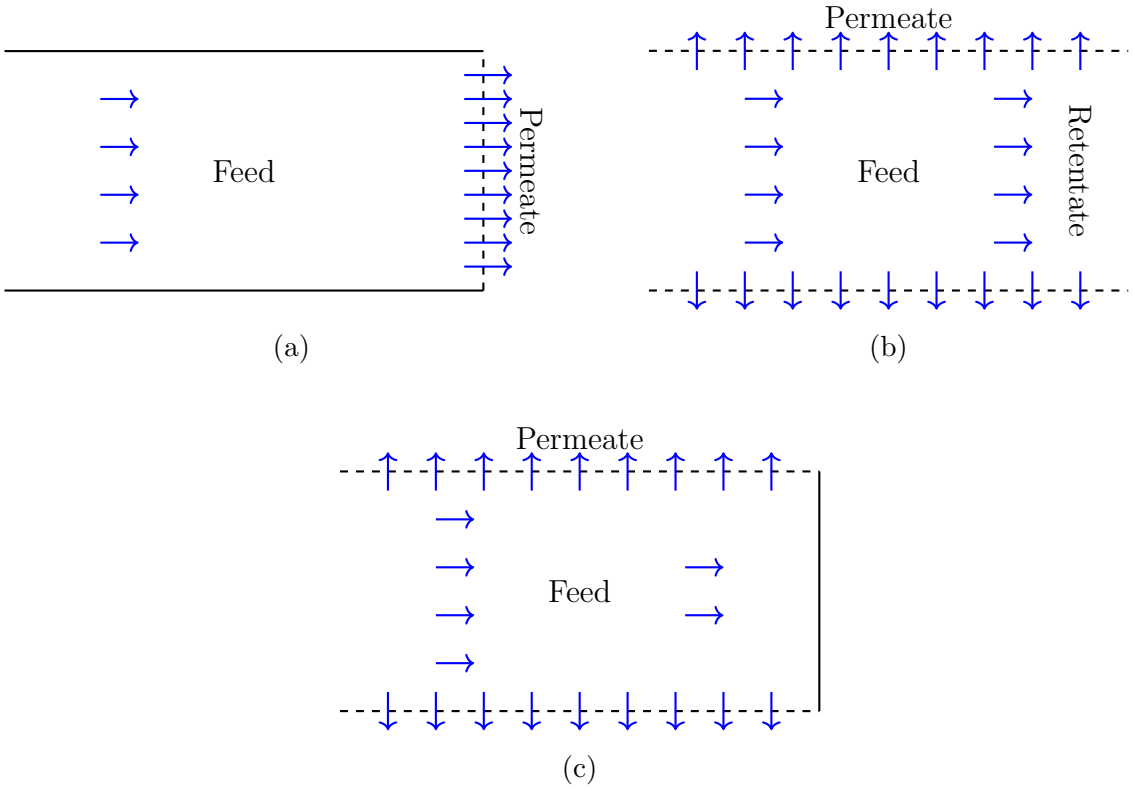

Figure 1.1: Schematics of (a) normal-flow, (b) cross-flow, and (c) direct-flow configurations. Impermeable walls are indicated by solid lines, membranes are indicated by dashed lines.

The main problem in membrane filtration is *fouling*, sometimes also referred to as *clogging*. Fouling denotes the process where particles are retained by the membrane, thereby increasing the resistance of the membrane. This in turn leads to a less effective filtration operation so that eventually the device has to be replaced. As fouling is common to all modes of filtration and membrane housings, it is being actively studied within the academic community by characterising different types of fouling, understanding the causes of fouling, and finding ways to reduce its impact on the efficiency of the filtration process. While certain module geometries aggravate fouling [103] or offer opportunities for improving the filter performance [52, 53], fouling is particularly pronounced in dead-end filtration, where the entire feed has to pass the membrane. We therefore study primarily simple dead-end filtration setups in this thesis but expect the underlying insights and results to be transferable to more complex geometries.

The processes underlying particle retention by membranes are complex, with dif-

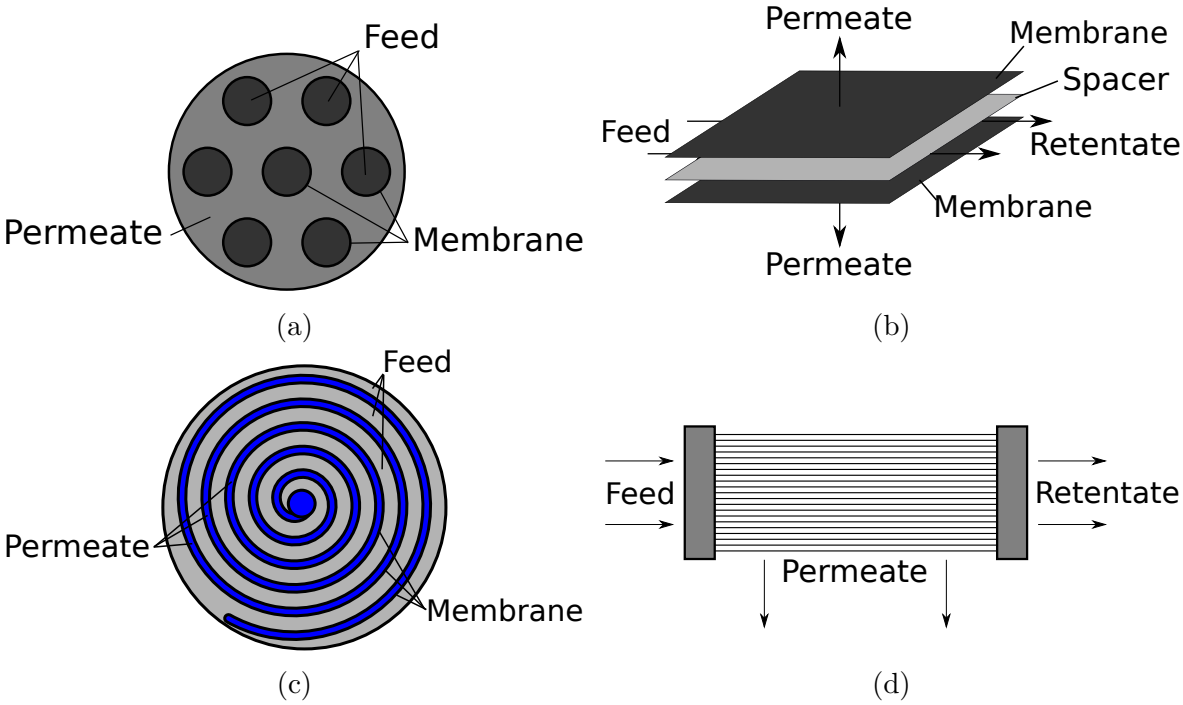

Figure 1.2: Schematics of four different membrane modules typically used in industrial applications to increase the membrane area per volume. The tubular configuration (a), cross-section, allows for membrane areas of up to 300 m^2/m^3, the plate and frame configuration (b) for up to 400 m^2/m^3, the spiral wound module (c), cross-section, for up to up to 1000 m^2/m^3, and the hollow fibre module (d) for up to 30000 m^2/m^3 [87].

ferent mechanisms, length-scales, and objects of various sizes and shapes being involved amongst others [113]. The key to improving membrane filtration lies therefore in finding appropriate models that are simple enough to allow for insights yet sophisticated enough to capture the relevant mechanisms. The simplest model for membrane filtration describes the membrane as a plate of uniform depth with cylindrical holes and the particles as spheres of uniform size. It allows for four different blocking mechanisms, where the particles can: (i) constrict the pores internally, (ii) seal the pores completely, (iii) seal the pores only partially, or, (iv) form an additional resistive layer, the *filtercake*; these mechanisms are termed *standard*, *complete*, and *intermediate blocking* and *cake filtration* respectively and were developed by Hermans and Bredée [49]; for an illustration see figure 1.3. The processed volume V as a function of time t for these four different blocking mechanisms in constant-pressure normal-flow filtration can be derived by simple geometric considerations, the resulting equations

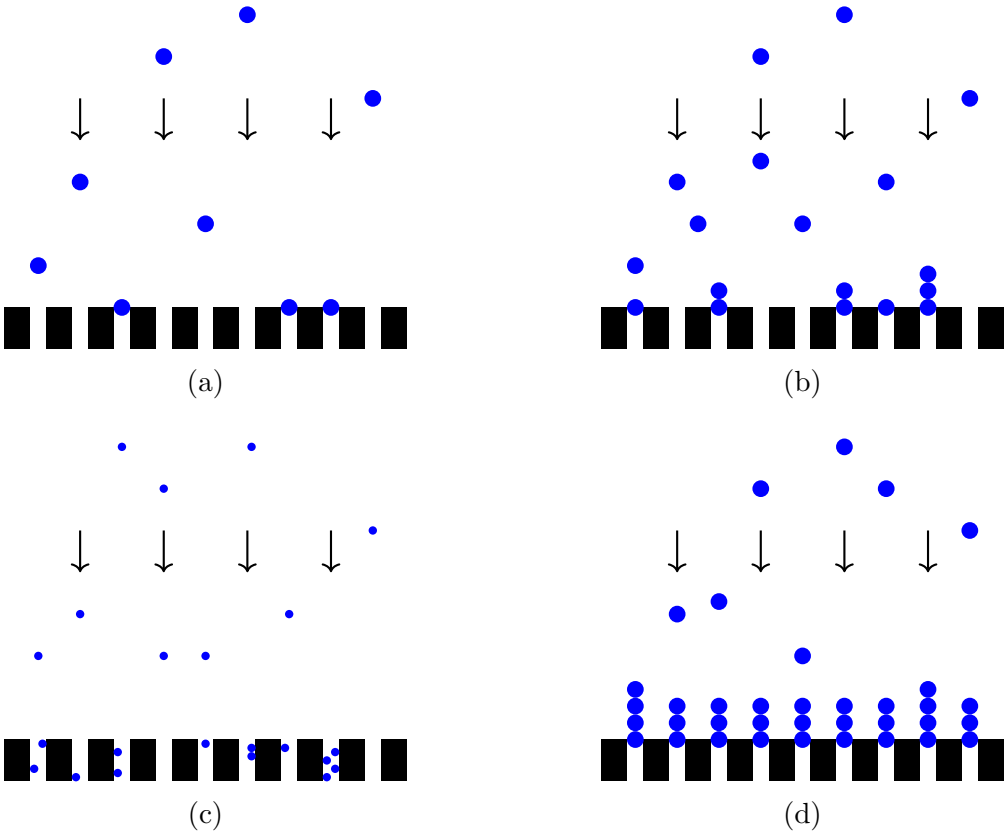

Figure 1.3: Schematics for the four blocking mechanisms: (a) complete blocking, (b) intermediate blocking, (c) standard blocking, and (d) caking. The difference between intermediate blocking and caking lies in the fact that particles stacked on top of other particles increase the resistance in the caking model but not in the intermediate model.

have been summarised by Hermia [50] as

$$\frac{\mathrm{d}^2 t}{\mathrm{d}V^2} = -c(n)\left(\frac{\mathrm{d}t}{\mathrm{d}V}\right)^n, \tag{1.1}$$

where $n = 0, 1, 3/2, 2$ for cake filtration, intermediate blocking, standard blocking, and complete blocking respectively; the constant $c(n)$ depends on properties of the feed and membrane. An equation that quantifies the decrease in permeability of a membrane due to fouling is called a *filtration law*; we will refer to the four filtration laws arising from (1.1) as the *conventional filtration laws*.

While the four different blocking mechanisms are derived by making rather simplistic assumptions about the pore geometry and the retention mechanisms, they are often sufficient to describe the measured decline in flux during a *constant-pressure filtration* run or the increase in pressure during a *constant-flow-rate filtration* run, where the pressure across the membrane or the flux through it is kept constant. For

example, Gironès et al. [42] modelled bovine serum albumin (BSA) filtration on silicon nitride microsieves using the complete-blocking law. De Lara and Benavente [33] observed cake filtration during BSA filtration with a polymeric membrane and standard blocking on a ceramic membrane, which is validated by SEM micrographs. Li et al. [79] reported best fits of cake filtration to the ultrafiltration of sodium alginate (SA) and intermediate blocking when subjecting SA to microfiltration. Finally, Bowen and Gan [21] found best fits of standard blocking to BSA separation, which is a common observation on the filtration of very dilute suspensions [65].

While the basic filtration laws are suitable to explain some experiments, they fail to explain other experiments, as detailed in Chapter 3. One resolution to this problem is to enhance the complexity of a filtration law by accounting for specific mechanisms, such as the compression of the filtercake. However, it is equally important to provide insight into when the simplifications of the standard model are justified. For example, is the standard model still appropriate if the particles in the feed have different sizes, and the pores are not straight tubes? Is the continuum model always appropriate, or do we have to model the particles in the feed as discrete entities? Additionally, one might consider whether determining a filtration law by fitting for the decline in flux during a constant-pressure filtration experiment is the best way, or whether there are other options if said measurements cannot be taken. Finally, do we actually need to approximate measurements by a filtration law, or can we just use experimental data directly when designing a membrane module for industrial applications?

In this thesis, we attempt to answer some of these questions by studying four different problems in the area of membrane filtration, which we believe contribute to the further understanding and improvement of membrane filtration by mathematical modelling. Our aim is not only to provide additional insights into already observed experimental phenomena, but also to provide inspirations and theoretical underpinnings for potential techniques and methods that can, at some point, be used by practitioners.

In this thesis, we are only concerned with membrane filtration for liquids at low Reynolds number flows and we do not expect our results to hold for membrane filters that operate in higher Reynolds number regimes such as air filters [12].

1.2 Overview of the thesis

In Chapter 2, we analyse why the conventional approach from the four filtration laws for modelling cake filtration typically provides a sufficiently good approximation for

measurements of constant-pressure filtration and therefore keeps being used in the engineering literature. Based on the theory of nonlinear poroelasticity, we derive a coupled model for the build-up and deformation of a porous medium, solve it numerically, and show that the resulting equations allow for a similarity solution given that a corresponding boundary-value problem can be satisfied. Using asymptotic analysis for the full model, we introduce a quasi-static caking model that provides a good approximation to the solution of the full model for typical experimental settings. This allows us to conclude that the complex deformable cake filtration model and the simple model are qualitatively equivalent for constant-pressure filtration. In the case of constant-flow-rate filtration, qualitative discrepancies between the two models emerge, as the models accounting for compression only allow for a finite maximum flux for a given cake length, and so running the filtration experiment at constant flux is only possible for a finite time.

In Chapter 3, we account for the fact that the particles retained by the membrane are discrete entities and introduce the theory to model filtration as a stochastic process, which allows us to understand the measurements at membrane level as the outcome of several stochastic processes at pore level. We extend this model to account for more complex pore structures, particle mixtures, and interconnected pores. We then analyse the relation between the discrete stochastic model and continuum models using the Fokker–Planck equation.

In Chapter 4, we analyse whether it is possible to determine the underlying filtration law that governs the spreading of a particle-laden gravity current on a pre-wetted membrane by tracking the position of the front in two specific settings. In the first half of Chapter 4, we combine the theory of gravity currents with the stochastic filtration theory developed in Chapter 3 to model corresponding experiments for the spreading of a particle-laden gravity current on a pre-wetted porous mesh. In the second half of Chapter 4, we consider the more general problem of inferring filtration laws from the spreading speed of solutions to the porous medium equation with drainage derived from a generalisation of the conventional filtration laws. We show that, under suitable influxes, we can in fact distinguish different filtration laws by observing their long-term spreading speed.

In Chapter 5, we model experiments for a multi-capsule depth filter, which is commonly used in large-scale industrial applications. Instead of using filtration laws to model the impact of fouling, we show how we can combine experimental measurements of filtration laws directly with simple fluid mechanics in order to obtain precise predictions for the scale-up of a multi-capsule depth filter.

These four chapters look at different problems of membrane filtration and are therefore intended to be self-contained. However, the first half of Chapter 4 uses basic ideas from the first sections of Chapter 3. Each chapter contains a literature review of its own as well as a conclusion. An outlook to future problems and improvements is given in Chapter 6.

1.3 Statement of originality

The work in thesis is believed to be original unless indicated otherwise, and each chapter contains a detailed account of the contributions for which we claim originality. As a general indicator, the work of Chapter 3, Chapter 4, and Chapter 5 is believed to be primarily original, whereas the work of Chapter 2 provides additional insights into an already existing theory and therefore predominantly consists of review material.

Chapter 2

Compression-dependent cake filtration

2.1 Introduction

A filtercake acts as a resistor in series, and so the permeability, k, of the combined membrane and cake satisfies

$$\frac{L_m + L_c}{k} = \frac{L_m}{k_m} + \frac{L_c}{k_c}, \tag{2.1}$$

where k_m is the permeability and L_m the length of the membrane, and k_c is the permeability and L_c the length of the filtercake. Within the experimental community, the permeability of the filtercake is usually modelled with a *conventional* approach where the porosity of the filtercake is assumed to be uniform throughout the cake [92]. While cake filtration is observed both in cross-flow [68] and dead-end filtration [39], we will only consider consider dead-end filtration in this chapter for simplicity. However, the results are expected to hold for cross-flow filtration and direct-flow filtration as long as the shear-flow within the filtercake is negligible.

When a fluid flows through a porous medium, it exerts a stress on its *solid matrix* which in turn leads to deformations that typically differ visibly from a comparable mechanical deformation [93], also reproduced in figure 2.1. The fluid flow through the porous medium can either be imposed by applying a mechanical load to one side of the fluid-filled medium, this is called *compaction* or *consolidation*, or by applying a pressure gradient across the medium, which is called *fluid-driven deformation*, the two different concepts are illustrated in figure 2.1. The study of deformations of fluid filled porous media was initially motivated by problems in civil engineering, where the deformation of soil subject to a mechanical load had to be determined [115], with the first complete mathematical treatise being based on the theory of linear elasticity

[18]. The problem of compaction is not only of interest in civil engineering, but also in the dewatering of fibres [55, 111] or in oil recovery, where the build-up of pore pressure due to sedimentation needs to be modelled [9].

Fluid-driven deformation is relevant for a variety applications, for example in the modelling of soft biological tissue [13] or in the manufacturing of composite materials, where the injection of a fluid into an initially dry porous medium has been studied [110]. With the filtercake simultaneously growing and deforming due to the fluid flow through it, cake filtration is another example of a problem in the domain of fluid-driven deformations and has been recognised as such since at least 1970 [109].

This chapter contributes to the understanding of why the conventional approach based on a uniform porosity of the filtercake is sufficient to model constant-pressure cake filtration. To do so, we consider the build-up of a one-dimensional porous medium of initial length L_i that is pinned to a solid mesh on its left side and has a free boundary on the right side, as in figure 2.1. The fluid flows from right to left due to an applied pressure gradient, the solid particles in the fluid are deposited at the upstream boundary of the porous medium. Note that this assumption neglects the potential migration of finer particles deeper into the filtercake [100]. We then derive an advection–diffusion equation for the porosity of the filtercake based on the theory of nonlinear poroelasticity following MacMinn et al. [83], which allows us to compute the compression and growth of the filtercake. Atsumi and Akayama [8] suggested that the corresponding equations of the Stefan problem associated with cake filtration allow for a similarity solution, albeit based on experimentally motivated assumptions regarding the growth in length, while Landman et al. [76] derived the similarity solution without making any simplifying assumptions. The similarity solution turns the partial differential equation (PDE) for the porosity into a boundary value problem for an ordinary differential equation (ODE), which leaves questions about the existence and uniqueness of the solution as well as the range of admissible values for boundary conditions of the boundary value problem.

By using asymptotic analysis, we show that a quasi-static caking model where the compression happens instantaneously is a suitable model for physically relevant situations. Using this quasi-static model, we then consider the problem of constant-flow-rate filtration, which highlights the difference between compression-dependent and conventional models, as the former only allows for a finite running time.

In Section 2.2, we briefly review the general theory for modelling deformations of fluid-filled porous media with two-phase models based on nonlinear poroelasticity. In Section 2.3, we introduce the uniaxial model for cake filtration and compression, and

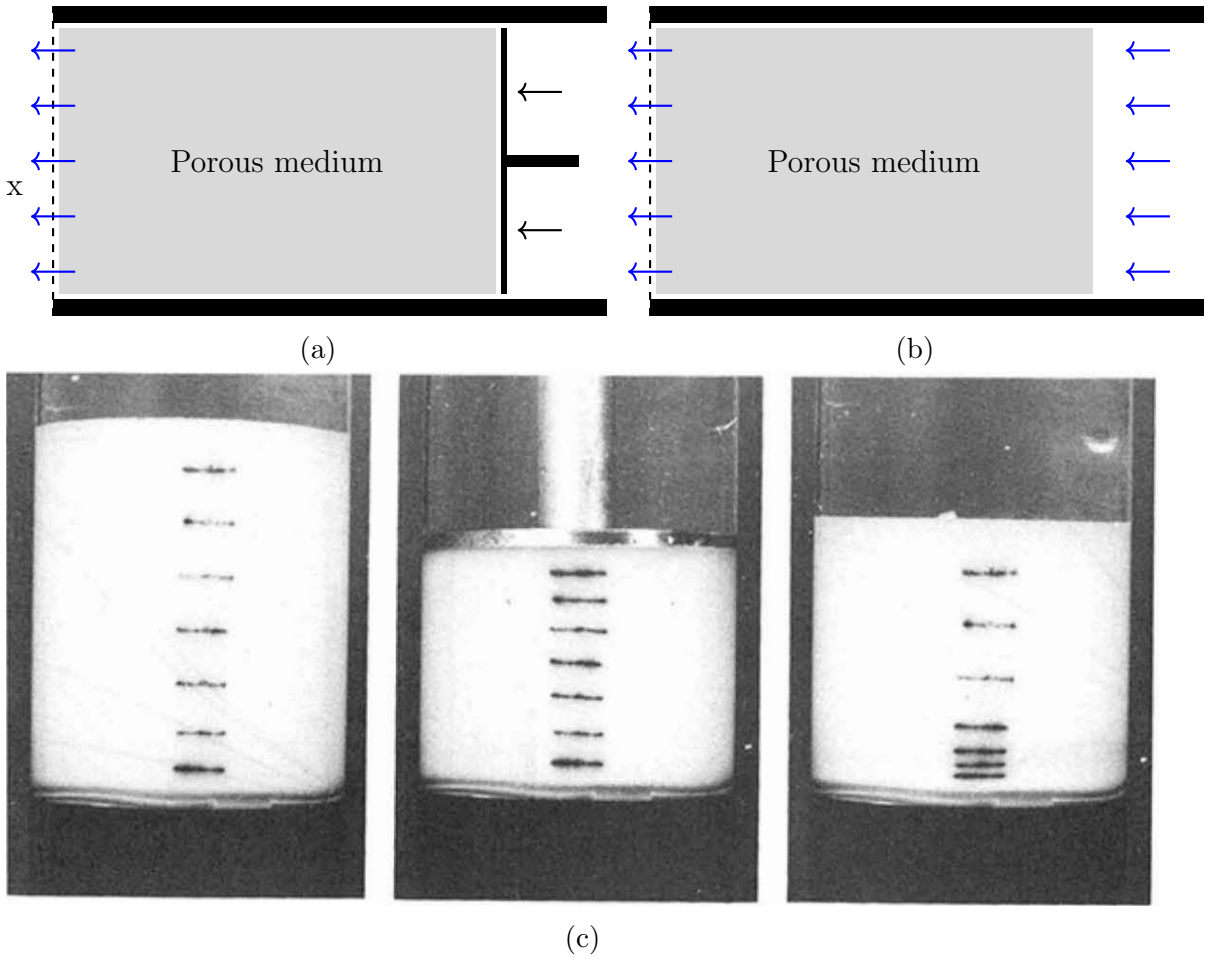

Figure 2.1: Schematics of (a) compaction by applying a mechanical load on the right side of the porous medium, which is enclosed in a solid container and attached to a mesh (dashed line) on the left side, and (b) fluid-driven deformation, where the porous medium is attached to the mesh one the left side and deforms due to the fluid flowing through it. In (c), taken from Parker et al. [93], the differences between mechanical and fluid-driven deformation are shown. An initially undeformed sponge (left) is compressed by a mechanical load (center) and by a fluid flow (right).

discuss numerical methods for solving it. In Section 2.4, we analyse the constant-pressure problem asymptotically and numerically, which motivates the derivation of the similarity solution. Finally, we compare the non-compressible model and the compressible model for constant-flow-rate filtration in Section 2.5.

The theory of fluid-driven deformations is well established [29], and modelling compressible cake filtration with two-phase models has been discussed in the literature before [8, 76]. We claim originality for the new insights in Sections 2.4 and 2.5 based on asymptotic analysis, except where stated otherwise.

Throughout this chapter, we will assume that the resistance of the membrane and the pressure drop in the channel are negligible and so we can impose boundary conditions directly at the upstream and downstream end of the filtercake; see figure 2.2. This greatly simplifies the analysis as we do not have to account for the changing pressure at the interface between the membrane and filtercake. We expect the qualitative results to hold as well for the instances where the resistance of the the membrane is non-negligible.

2.2 Modelling fluid-driven deformation with nonlinear poroelasticity

As the experiments of Parker et al. [93] have shown, fluid-driven compression in a uniaxial setting can lead to large deformations and introduces non-uniform strains, and so we cannot expect the permeability of the filtercake to be uniform. In this section, we review the standard theory for modelling deformations of fluid-filled porous media based on two-phase models coupled with nonlinear poroelasticity. This section is a brief review of much more extensive works [29, 83], it is included to introduce the general ideas of poroelasticity and to provide a basis for appreciating the crucial simplifications that the uniaxial model, introduced in Section 2.3, allows for.

Throughout this chapter, we assume that both the fluid and solid phase are incompressible, and so any compression or extension of the porous medium will in fact be a change in the relative volume fractions of the two phases. We also assume that the porous medium is fully saturated. Denoting the fluid volume fraction by ϕ_f and the solid volume fraction by ϕ_s, we therefore must have $\phi_s + \phi_f \equiv 1$. This allows us to work with the fluid volume fraction only and we write $\phi = \phi_f$ accordingly, we will at times refer to ϕ as *porosity* for brevity. The initial volume fraction of the liquid at time $t = 0$ is denoted by $\Phi(x) = \phi(x, 0)$.

The two-phase model consists of four equations: Due to the incompressibility of the solid and the fluid phase, Reynolds' transport theorem [1] yields a conservation of mass for each phase,

$$\frac{\partial \phi}{\partial t} + \nabla \cdot (\phi \mathbf{v}_f) = 0, \tag{2.2a}$$

$$\frac{\partial (1-\phi)}{\partial t} + \nabla \cdot ((1-\phi)\mathbf{v}_s) = 0, \tag{2.2b}$$

where $\mathbf{v}_f, \mathbf{v}_s$ denote the velocities of the fluid and solid.

As we are only considering low-Reynolds-number flow, Darcy's law [14] is a suitable constitutive law to relate the gradient of the pressure p to the difference between the velocities of the fluid and solid phase, which in this instance reads as

$$\phi \left(\mathbf{v}_f - \mathbf{v}_s\right) = -\frac{k(\phi)}{\mu} \left(\nabla p + \mathbf{G}\right), \tag{2.3}$$

where μ denotes the dynamic viscosity of the liquid, $\mathbf{G}$ a body force such as gravity, and we assume that the permeability k of the porous medium only depends on the porosity ϕ. While there is no universally valid permeability–porosity relationship, appropriate constitutive relations between the porosity and permeability can be found for a wide range of settings [16]; we introduce a suitable relationship in the next section.

To complete the two-phase model, we assume that inertial effects are negligible and therefore introduce mechanical equilibrium as the fourth equation. In mechanical equilibrium, the total stress S in the matrix, which consists of the stress in the solid matrix τ and the stress exerted by the fluid, has to balance the body force $\mathbf{G}$. It can be shown that the shear stress is negligible compared to the bulk stress of the liquid [83], and so a common modelling assumption is to use *Terzaghi's principle* which states that, at macroscopic level, the stress exerted by the fluid is the pore pressure. Thus, the net stress S in the porous medium is given by

$$S = pI + \tau, \tag{2.4}$$

where I denotes the identity matrix, and so we obtain

$$\nabla \cdot S + \mathbf{G} = \nabla p + \nabla \cdot \tau + \mathbf{G} = 0. \tag{2.5}$$

Writing $\mathbf{v}_f = \phi \mathbf{v}_f + (1-\phi)\mathbf{v}_s + (1-\phi)\mathbf{v}_f - (1-\phi)\mathbf{v}_s$, we can combine the equations for conservation of mass (2.2) with Darcy's law (2.3) and the mechanical equilibrium (2.5) to obtain an equation for the flux $\mathbf{Q} = \phi \mathbf{v}_f + (1-\phi)\mathbf{v}_s$ as

$$\frac{\partial \phi}{\partial t} + \nabla \cdot \left(\phi \mathbf{Q} + (1-\phi) \frac{k(\phi)}{\mu} \nabla \cdot \tau \right) = 0. \tag{2.6}$$

Note that conservation of mass for the fluid and solid phase (2.2) leads immediately to the incompressibility condition $\nabla \cdot \mathbf{Q} = 0$.

To proceed, we need to introduce a constitutive relationship for the stress–strain relationship. For larger deformations, we assume the material to be *hyperelastic* and so the stress–strain relationship can be derived from a strain-energy density function $\mathcal{W}$ [59]. That is, for a displacement $\mathbf{u_s}(\mathbf{X}, \mathbf{t}) = \mathbf{x}(\mathbf{X}, t) - \mathbf{X}$ of the solid, we assume that the stress tensor τ is given by

$$\tau_{ij} = \frac{\partial \mathcal{W}}{\partial F_{ij}}, \quad 1 \leq i, j \leq 3, \tag{2.7}$$

where F denotes the *deformation-gradient tensor* defined as

$$F^{-1} = I - \nabla \mathbf{u}_s. \tag{2.8}$$

If the deformation of the material is small compared to the length of the medium or the applied pressure difference across the medium is small compared to the stiffness of the medium, it can be sufficient to use a linear stress–strain relationship. For an isotropic material, this implies that the elastic stress tensor τ is given by

$$\tau = \Lambda(\nabla \cdot \mathbf{u}_s)I + M\left(\nabla \mathbf{u}_s + \nabla \mathbf{u}_s^{\intercal}\right) \tag{2.9}$$

where Λ, M are the Lamé constants of the material. While M must always be positive, Λ need not be (but is positive for most materials) and the condition $\Lambda + 2M/3 > 0$ must be satisfied. Values range from $\Lambda = 3 \cdot 10^5$ Pa and $M = 9 \cdot 10^5$ Pa for cartilage to $\Lambda = 2.6 \cdot 10^{12}$ Pa and $M = 4 \cdot 10^{12}$ Pa for diamond [59]. As we are considering a porous material, the effective parameters for the solid/liquid mixture will be different from the parameters of the solid.

In the next section, the definition of the constitutive stress–strain relations will be significantly simplified, as the uniaxial setting allows us to introduce a direct relation between the porosity ϕ and the strain. This is no longer true in higher dimensions, see for example Auton and MacMinn [10]. We will work on the basis of hyperelasticity, but also use linear elasticity for comparison to understand when nonlinear effects become relevant.

2.3 Uniaxial cake filtration and compaction

In this section, we derive the one-dimensional caking model based on the two-phase model introduced in Section 2.2. The key ingredient of the caking model is the

boundary condition for the growth of the porous medium due to the deposition of particles, which will be derived in Section 2.3.2. We will then nondimensionalise the complete model and introduce a numerical scheme to solve the dimensionless problem.

2.3.1 Governing equations

The fluid-driven deformation of a porous medium is governed by the general advection–diffusion equation (2.6). In the uniaxial setting, we can transform this equation into a one-dimensional advection–diffusion equation for the volume fraction ϕ of the fluid phase due to two key assumptions: First, because we are assuming the solid matrix to be hyperelastic, the stress in the porous matrix will only depend on the strain. In a uniaxial setting, the relationship between the strain and the porosity is invertible, and so the stress will only depend on the porosity. Second, we also assume the permeability to only depend on the porosity. To derive the one-dimensional advection–diffusion equation, we first state the one-dimensional versions of the conservation of mass, Darcy's law, and mechanical equilibrium and derive the strain–porosity relationship. We introduce constitutive relationships for the porosity and stress–strain behaviour at the end of this section.

Let us consider a porous medium of length L oriented along the x-axis, which is completely filled with liquid. Both the liquid and the solid phase are assumed to be incompressible, hence we obtain the conservation of mass in the one-dimensional version of (2.2) as

$$\frac{\partial \phi}{\partial t} + \frac{\partial}{\partial x}\left(\phi v_f\right) = 0, \tag{2.10a}$$

$$-\frac{\partial \phi}{\partial t} + \frac{\partial}{\partial x}\left((1-\phi) v_s\right) = 0. \tag{2.10b}$$

The porous medium is oriented along the x-axis, hence gravity does not play a role, and so Darcy's law (2.3) becomes

$$\phi(v_f - v_s) = -\frac{k(\phi)}{\mu}\frac{\partial p}{\partial x}. \tag{2.11}$$

Finally, the one-dimensional version of mechanical equilibrium (2.5) is given by

$$\frac{\partial \tau}{\partial x} = -\frac{\partial p}{\partial x}. \tag{2.12}$$

The incompressibility for the total volume flux $Q = \phi v_f + (1-\phi)v_s$ is given by $\partial Q/\partial x = 0$, and so we have $Q = Q(t)$.

To make progress, we show that hyperelasticity allows us to introduce a constitutive relation between the stress tensor τ and the liquid volume fraction ϕ. For a one-dimensional, uniform deformation of a segment, the strain e is defined as the ratio of the length difference between its initial length L and new length L' to its initial length, that is

$$e = \frac{L' - L}{L}. \tag{2.13}$$

Now, consider a solid of length l being part of a material of length L. Then, we know $(1 - \Phi)L = l$, where Φ denotes the volume fraction of the material in the undeformed state. If this is deformed to a new length L', we have, due to conservation of mass, $(1 - \phi)L' = l$ and so we obtain

$$e = \frac{\phi - \Phi}{1 - \phi}. \tag{2.14}$$

Now, the stress τ only depends on the strain based on the assumption of hyperelasticity, and so equation (2.14) immediately allows us to write

$$\tau = \tau(\phi), \tag{2.15}$$

which is also known as *Athy's law* [7] based on his experimental work on porosity profiles in sediments. In one dimension we can equivalently introduce a constitutive relation for the pore pressure p as $p = p(\phi)$ due to (2.12). This will not hold in higher dimensions as the strain will in general no longer uniquely depend on the porosity.

For the permeability k, we follow [54] and use the Carman–Kozeny relation as the constitutive relation, that is

$$k(\phi) = k^\star \frac{\phi^3}{(1 - \phi)^2}, \tag{2.16}$$

where the *characteristic permeability* $k^\star$ is a constant for a given material. For the stress–strain relation, we require the stress to diverge as a minimum porosity ϕ_m is attained, which is related to a maximal strain $e_M = (\phi_m - \Phi)/(1 - \phi_m)$. We therefore use the linear model with finite strain from Nordstrom et al. [91],

$$\tau(e) = -\tau^\star \frac{e}{1 - e/e_M}, \tag{2.17}$$

where $\tau^\star$ is a dimensional constant, the *characteristic matrix pressure*. We expect a typical filtercake composed of cells or proteins to be sufficiently *squishy* to attain volume fractions arbitrarily close to 1 under an applied stress. Hence, we choose $\phi_m = 0$ as the minimum porosity and so the constitutive relation (2.17) becomes

$$\tau_{\text{nonlin}}(\phi) = -\tau^\star \frac{\Phi}{1 - \Phi} \frac{\phi - \Phi}{\phi}. \tag{2.18}$$

For comparisons with linear elasticity, we use the exact definition of the strain (2.14) instead of a linear approximation and obtain

$$\tau_{\text{lin}}(\phi) = -\tau^\star \frac{\phi - \Phi}{1 - \phi}. \tag{2.19}$$

For linear elasticity in one dimension, we have $\tau^\star = \Lambda + 2M$, where Λ, M are the Lamé constants introduced in Section 2.2, which can be used as a good estimate for the magnitude of $\tau^\star$. Despite having introduced specific constitutive relations for $k(\phi)$ and $\tau_{\text{lin}}(\phi), \tau_{\text{nonlin}}(\phi)$, we will use k and τ to keep the derivation of the following equations as general as possible and to underline that the results hold for both choices of constitutive stress-strain relations. In the following, we will refer to the constitutive relation (2.18) as the *Nordstrom* and to (2.19) as the *linear* stress–strain relation.

To derive the advection–diffusion equation for ϕ, note that we can combine Darcy's law (2.11) and the definition of the flux $Q = \phi v_f + (1 - \phi)v_s$ to obtain

$$v_s = Q + \frac{k(\phi)}{\mu} \frac{\partial p}{\partial x}. \tag{2.20}$$

Now, using mechanical equilibrium (2.12) in (2.20) and the conservation of mass for the solid phase (2.10), we obtain the advection–diffusion equation for ϕ as

$$\frac{\partial \phi}{\partial t} + Q \frac{\partial \phi}{\partial x} = -\frac{\partial}{\partial x} \left[(1 - \phi) \frac{k(\phi)}{\mu} \frac{\partial \tau}{\partial \phi} \frac{\partial \phi}{\partial x} \right], \tag{2.21}$$

where we have used the incompressibility $\partial Q / \partial x = 0$ of the fluid. We will derive the boundary conditions in the next subsection.

2.3.2 Boundary conditions

To solve (2.21) for $x \in [0, L(t)]$, where the moving boundary $L(t)$ arises due to compression and deposition, we need to impose four boundary conditions and two initial conditions. For the initial conditions, we assume that the porous medium has length $L(0) = L_i$ and that it is initially undeformed, that is, $\phi(x, 0) = \Phi$.

For the derivation of the boundary conditions, we assume $t > 0$. The first two boundary conditions are for the porosity at the left and right boundary, which are determined by the imposed pressure difference. The pressure difference across the membrane is Δp, and so we can set, without loss of generality (w.l.o.g.),

$$p(0) = 0 \quad \text{and} \quad p(L(t)) = \Delta p. \tag{2.22}$$

The porous medium is unstressed at the right edge and so the matrix stress has to balance the entire applied pressure at the left edge, yielding

$$\tau(0) = \Delta p \quad \text{and} \quad \tau(L(t)) = 0. \tag{2.23}$$

From our porosity–strain relationship (2.14) we identify the unstressed state $\tau = 0$ with $\phi = \Phi$ to obtain

$$\phi(0) = \tau^{-1}(\Delta p) \quad \text{and} \quad \phi(L(t)) = \Phi. \tag{2.24}$$

On the left-boundary, the porous medium is fixed, and so the solid phase cannot move, hence

$$v_s(0, t) = 0, \tag{2.25}$$

and so the flux $Q(t)$ is given by

$$Q(t) = \phi v_f|_{(0,t)}\,. \tag{2.26}$$

To derive the condition for the moving boundary $L(t)$, we consider conservation of mass. Let $V(t)$ denote the total volume of the porous medium, whose unit is metres as we are considering the one-dimensional problem. Both the fluid and solid phase are incompressible, yielding

$$V(t) = \int_0^{L(t)} (1 - \phi)\ \mathrm{d}x. \tag{2.27}$$

The volume increases due to deposition, that is

$$\frac{\mathrm{d}V}{\mathrm{d}t} = -cQ(t), \tag{2.28}$$

where c is the volume fraction of particles in the fluid. Note that we use the negative sign due to the direction of the flow. Using Leibniz' integral rule, we obtain

$$-cQ(t) = \frac{\mathrm{d}V}{\mathrm{d}t} = \frac{\mathrm{d}}{\mathrm{d}t}\left(\int_0^{L(t)} (1 - \phi)\ \mathrm{d}x\right) = (1 - \Phi)\frac{\mathrm{d}L}{\mathrm{d}t} - \int_0^{L(t)} \frac{\partial \phi}{\partial t}\mathrm{d}x \tag{2.29}$$

and using conservation of mass for the solid velocity v_s (2.10) together with $v_s = 0$ at $x = 0$ gives

$$\frac{\mathrm{d}L}{\mathrm{d}t} = v_s - \frac{c}{1 - \Phi}Q. \tag{2.30}$$

Now, we can use (2.20) to finally obtain the boundary condition as

$$\frac{\mathrm{d}L}{\mathrm{d}t} = Q\left(1 - \frac{c}{1 - \Phi}\right) - \left.\frac{k(\phi)}{\mu}\frac{\partial \tau}{\partial \phi}\frac{\partial \phi}{\partial x}\right|_{(L(t),t)}. \tag{2.31}$$

We point out that the boundary condition (2.31) is a special case of more general moving boundary conditions when there is sedimentation at a rate of $\dot{m}_s$,

$$\frac{\partial L}{\partial t} = v_s - \dot{m}_s, \tag{2.32}$$

see for example [41].

2.3.3 Nondimensionalisation

For the nondimensionalisation, we follow Hewitt et al. [54] and nondimensionalise the equations on the basis of the characteristic matrix pressure $\tau^\star$, the characteristic permeability $k^\star$, and initial length $L_i > 0$, which will automatically introduce a velocity scale for the flux Q. While it is just as valid to use the applied pressure difference Δp in the nondimensionalisation, using the characteristic matrix pressure allows for a better estimation of the pressures involved when interpreting the results for the dimensionless model. We assume the initial length L_i to be greater than zero so that we can apply Darcy's law, the similarity solution introduced in section 2.4.2 will later allow us to consider the limit $L_i \to 0$. We rescale both the stress τ and pressure p with the matrix pressure scale $\tau^\star$:

$$p = \tau^\star \tilde{p} \quad \text{and} \quad \tau = \tau^\star \tilde{\tau}. \tag{2.33}$$

For the position x and the length L, the initial length L_i is used to nondimensionalise as

$$x = L_i \tilde{x} \quad \text{and} \quad L = L_i \tilde{L}. \tag{2.34}$$

The boundary condition for the flux Q (2.26) and Darcy's law (2.11) suggest the nondimensionalisation

$$Q = \frac{k^\star \tau^\star}{\mu L_i} \tilde{Q}. \tag{2.35}$$

For the time t, introduce a time scale based on the initial length L_i and the characteristic velocity scale,

$$t = \frac{\mu L_i^2}{k^\star \tau^\star} \tilde{t}. \tag{2.36}$$

The nondimensionalisation leads to two dimensionless parameters: the parameter δ governing the increase in length due to the deposition of particles and the parameter $\mathcal{P}$ denoting the ratio of the applied pressure Δp to the matrix pressure $\tau^\star$, defined respectively as

$$\delta = \frac{c}{1 - \Phi} \quad \text{and} \quad \mathcal{P} = \frac{\Delta p}{\tau^\star}. \tag{2.37}$$

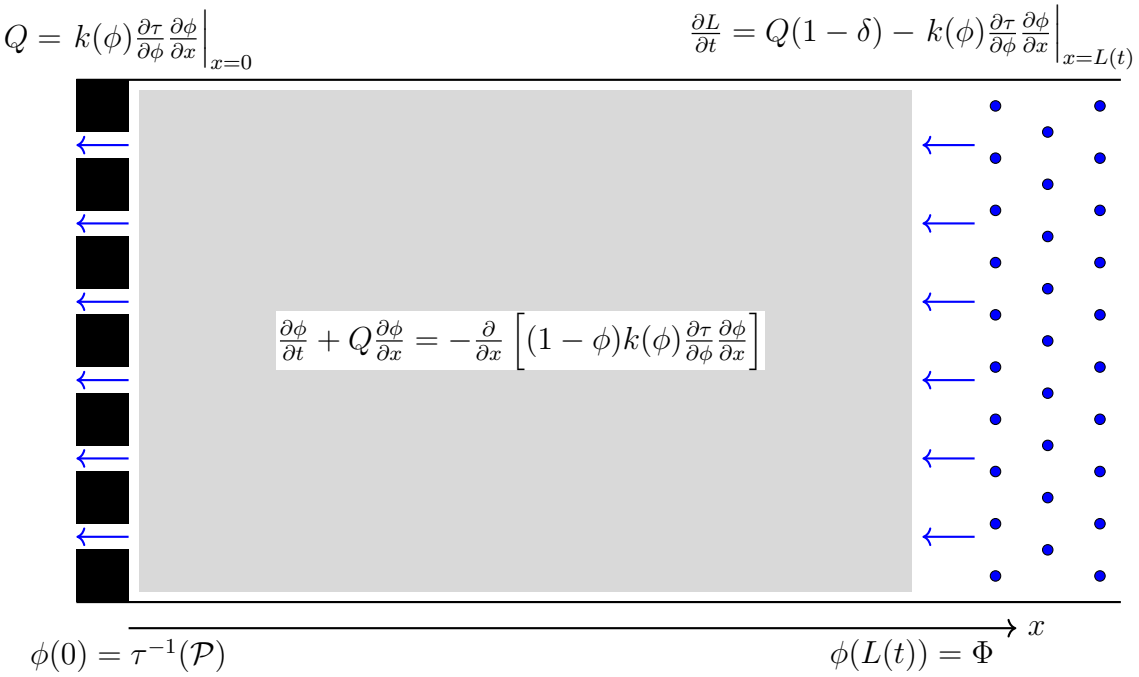

Figure 2.2: Schematic of the modelling setup. The growing porous medium is fixed at the left boundary and grows through the deposition of particles at the upstream boundary, we assume that the resistance of the permeable barrier at the left is negligible and so we can impose the pressure boundary condition directly at the downstream boundary of the porous medium. The deformation of the porous medium due to the fluid flow is determined by the advection–diffusion equation for the porosity.

We now rewrite the model in dimensionless form and drop the tildes for ease of reading.

With these nondimensionalisations, the dimensional advection–diffusion equation (2.21) for the porosity becomes

$$\frac{\partial\phi}{\partial t} + Q\frac{\partial\phi}{\partial x} = -\frac{\partial}{\partial x}\left[(1-\phi)k(\phi)\frac{\partial\tau}{\partial\phi}\frac{\partial\phi}{\partial x}\right], \tag{2.38}$$

subject to the initial conditions $L(0) = 1$ and $\phi(x, 0) = \Phi$. The boundary conditions for the porosity are given by

$$\phi(0) = \tau^{-1}(\mathcal{P}) \quad \text{and} \quad \phi(L(t)) = \Phi, \tag{2.39}$$

and the expressions for the flux and the moving boundary are given by

$$Q = k(\phi)\frac{\partial\tau}{\partial\phi}\frac{\partial\phi}{\partial x}\Big|_{x=0} \quad \text{and} \quad \frac{\partial L}{\partial t} = Q(1-\delta) - k(\phi)\frac{\partial\tau}{\partial\phi}\frac{\partial\phi}{\partial x}\Big|_{x=L}. \tag{2.40}$$

The full problem is sketched in figure 2.2. In the next subsection, we will briefly describe the numerical method used to compute the solution of (2.38) subject to the boundary conditions (2.39) and (2.40).

2.3.4 Numerical methods

We solve the nonlinear advection–diffusion equation (2.38) for the porosity with the method of lines and discretise in space using finite-differences. To transform the moving boundary problem into a problem on a fixed interval, the scaling

$$\eta = \frac{x}{L(t)} \tag{2.41}$$

is introduced and we choose N equidistant points in $[0, 1]$ via

$$\eta_i = \frac{i}{N+1}, \text{ for } i = 1, \ldots, N. \tag{2.42}$$

Rewriting equation (2.38) in terms of η, this becomes

$$\frac{\partial \phi}{\partial t} - \frac{\dot{L}}{L}\eta\frac{\partial \phi}{\partial \eta} + \frac{Q}{L}\frac{\partial \phi}{\partial \eta} = -\frac{1}{L^2}\frac{\partial}{\partial \eta}\left[(1-\phi)k(\phi)\frac{\partial \tau}{\partial \phi}\frac{\partial \phi}{\partial \eta}\right]. \tag{2.43}$$

The boundary conditions for ϕ (2.39) are unaffected by the scaling,

$$\phi(0) = \tau^{-1}(\mathcal{P}) \quad \text{and} \quad \phi(1) = \Phi, \tag{2.44}$$

whereas the boundary conditions (2.40) for Q and $\mathrm{d}L/\mathrm{d}t$ become

$$Q = \frac{1}{L}k(\phi)\frac{\partial \tau}{\partial \phi}\frac{\partial \phi}{\partial \eta} \quad \text{at } \eta = 0 \tag{2.45}$$

and

$$\frac{\mathrm{d}L}{\mathrm{d}t} = Q\,(1-\delta) - \frac{1}{L}k(\Phi)\frac{\partial \tau}{\partial \phi}\frac{\partial \phi}{\partial \eta} \quad \text{at } \eta = 1. \tag{2.46}$$

2.4 Cake filtration for constant-pressure filtration

In this section, we evaluate the compressible cake model for a constant-pressure filtration. Rescaling the dimensionless equations with the caking time scale using the dimensionless parameter δ, we consider the simplified behaviour of the model when δ is very small or very large, we will call these the *slow-* and *fast-caking* limits. In the instance where δ is very small, we recover a quasi-static caking model and we show very good agreement between the full and the quasi-static model. We then argue that the instance of δ being large is not physically sensible but nevertheless mathematically interesting. Motivated by the numerical simulations, we show that the full caking problem exhibits a similarity solution, as has been reported previously [8, 76].

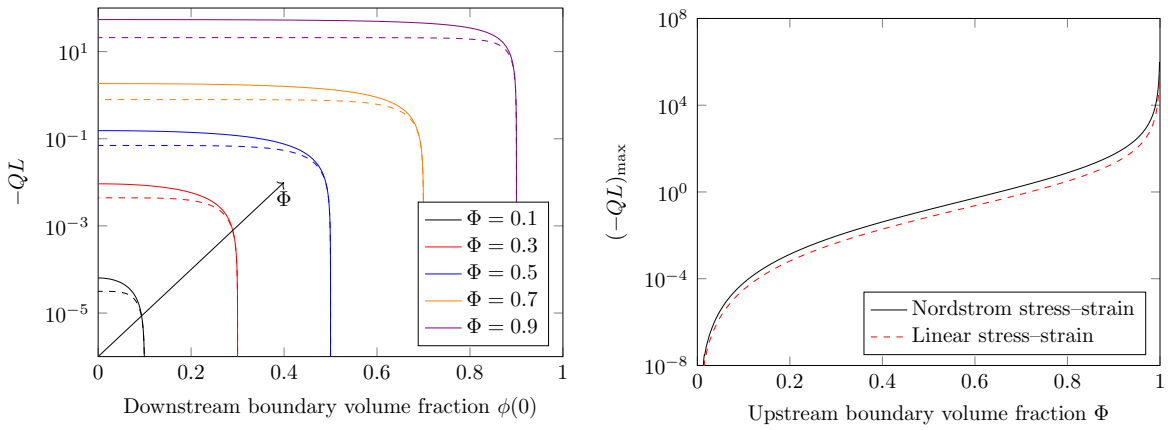

(a) (b)

Figure 2.3: In (a), we show the values of the product of the flux and length for the steady-state of the fluid driven deformation for different combinations of the volume fraction at the downstream boundary $\phi(0)$ and the volume fraction Φ at the upstream boundary. We see a good agreement between the Nordstrom (bold) and linear (dashed) model as long as $\phi(0)$ is close to Φ. In (b), we show the maximum value of $-QL$ which is, for our constitutive relations for permeability and stress–strain, attained when $\phi(0) = 0$.

2.4.1 The slow- and fast-caking limits

Using the caking time scale T, defined as $t = \delta^{-1}T$, the dimensionless advection–diffusion equation (2.38) for the porosity becomes

$$\delta\frac{\partial\phi}{\partial T} + Q\frac{\partial\phi}{\partial x} = -\frac{\partial}{\partial x}\left[(1-\phi)k(\phi)\frac{\partial\tau}{\partial\phi}\frac{\partial\phi}{\partial x}\right], \tag{2.47}$$

subject to the initial conditions $L(0) = L_i$ and $\phi(x,0) = \Phi$. Here, we use $L(0) = L_i$ instead of $L(0) = 1$ to obtain a consistent derivation of the slow-caking limit. For $T > 0$, the boundary conditions for the porosity remain as before,

$$\phi(0) = \tau^{-1}(\mathcal{P}) \quad \text{and} \quad \phi(L(t)) = \Phi, \tag{2.48}$$

and we obtain for the flux and the moving boundary

$$Q = k(\phi)\frac{\partial\tau}{\partial\phi}\frac{\partial\phi}{\partial x}\bigg|_{x=0} \quad \text{and} \quad \frac{\partial L}{\partial T} = \delta^{-1}\left(Q - k(\phi)\frac{\partial\tau}{\partial\phi}\frac{\partial\phi}{\partial x}\bigg|_{x=L}\right) - Q. \tag{2.49}$$

We now consider the limiting cases of slow caking, which corresponds to $\delta \to 0$, and fast caking, which corresponds to $\delta \to \infty$.

The slow-caking limit

The slow-caking limit corresponds to feeds with low concentration and we expect compaction to happen much faster than the build-up of cake. For $\delta \ll 1$, the dimensionless advection–diffusion equation (2.47) simplifies at first order to

$$Q\frac{\mathrm{d}\phi}{\mathrm{d}x} = -\frac{\mathrm{d}}{\mathrm{d}x}\left[(1-\phi)k(\phi)\frac{\mathrm{d}\tau}{\mathrm{d}\phi}\frac{\mathrm{d}\phi}{\mathrm{d}x}\right], \tag{2.50}$$

subject to the boundary conditions

$$\phi(0) = \tau^{-1}(1), \quad \phi(L) = \Phi, \quad \text{and} \quad Q = k(\phi)\frac{\mathrm{d}\tau}{\mathrm{d}\phi}\frac{\mathrm{d}\phi}{\mathrm{d}x}\bigg|_{x=L}, \tag{2.51}$$

where L denotes the steady-state length of the porous medium, which will be different from the initial length L_i due to deformation. This is the classical steady-state limit of the flow-induced deformation of a porous medium, see [29, 54, 83]. We compute the steady-state flux Q and steady-state length L directly as follows, assuming that τ is invertible (see [83] for a more general strategy):
Both the liquid and solid phase are assumed to be incompressible, and so conservation of mass yields

$$(1-\Phi)L_i = \int_0^L (1-\phi)\,\mathrm{d}x. \tag{2.52}$$

To compute the flux Q, we write

$$(1-\phi)Q = (1-\phi)k(\phi)\frac{\mathrm{d}\tau}{\mathrm{d}\phi}\frac{\mathrm{d}\phi}{\mathrm{d}x}, \tag{2.53}$$

and obtain

$$QL_i = \int_0^L \frac{(1-\phi)k(\phi)\frac{\mathrm{d}\tau}{\mathrm{d}\phi}\frac{\mathrm{d}\phi}{\mathrm{d}x}}{1-\Phi}\,\mathrm{d}x = \int_{\phi(0)}^{\Phi} \frac{1-\phi}{1-\Phi}k(\phi)\frac{\mathrm{d}\tau}{\mathrm{d}\phi}\,\mathrm{d}\phi, \tag{2.54}$$

because τ is invertible. In the steady state, the solid velocity vanishes, and so the flux Q is given by $Q = \phi v_f$. The dimensionless version of Darcy's law (2.11) therefore states $\phi v_f = k(\phi)\mathrm{d}\tau/\mathrm{d}x$, and the length L can be determined by integrating the constant flux Q from 0 to L,

$$QL = \int_0^L k(\phi)\frac{\mathrm{d}\tau}{\mathrm{d}\phi}\frac{\mathrm{d}\phi}{\mathrm{d}x}\,\mathrm{d}x = \int_{\phi(0)}^{\Phi} k(\phi)\frac{\mathrm{d}\tau}{\mathrm{d}\phi}\,\mathrm{d}\phi. \tag{2.55}$$

An important takeaway from (2.55) is that the product of the flux and length is a constant that, for given constitutive relations for the permeability and stress–strain relationship, only depends on the initial and unstressed porosity Φ and the applied

pressure $\mathcal{P}$. We compare different values of QL for the steady-state case, both for the linear and Nordstrom stress–strain relationship, in figure 2.3.

To compare the slow-caking limit ($\delta \to 0$) with the general case ($\delta > 0$), we compute the product QL for large times $t = 10^6$ numerically. This is motivated by the observation that the flux should be (approximately) inversely proportional to the length by Darcy's law, making QL a constant. Moreover, we have $\mathrm{d}L/\mathrm{d}T \approx -Q$ and so we obtain $-QL \approx 1/2(\dot{L}^2)$, which would allow us to determine the growth in length if we knew the value of QL. While this argument makes certain simplistic assumptions, the similarity solution introduced in Section 2.4.2 will justify treating QL as a constant for sufficiently large t. The results for the Nordstrom stress–strain relation are shown in figure 2.4a, we note that for $\delta \leq 0.1$, the quasi-steady model provides an excellent approximation to the full model, the behaviour for $\delta > 1$ is discussed in the next section.

For completeness, we introduce a quasi-static caking law from equations (2.54) and (2.55). We assume

$$\frac{\mathrm{d}L_i}{\mathrm{d}T} = -Q, \tag{2.56}$$

and so we obtain

$$L_i(T) = \left(-2T \int_{\phi(0)}^{\Phi} \frac{1-\phi}{1-\Phi} k(\phi) \frac{\mathrm{d}\tau}{\mathrm{d}\phi} \, \mathrm{d}\phi \right)^{1/2}. \tag{2.57}$$

The compressed length L can be computed using (2.54) and (2.55) to obtain

$$L(T) = \left(\int_{\phi(0)}^{\Phi} k(\phi) \frac{\mathrm{d}\tau}{\mathrm{d}\phi} \, \mathrm{d}\phi \right) \cdot \left(\int_{\phi(0)}^{\Phi} \frac{1-\phi}{1-\Phi} k(\phi) \frac{\mathrm{d}\tau}{\mathrm{d}\phi} \, \mathrm{d}\phi \right)^{-1} L_i(T). \tag{2.58}$$

The fast-caking limit

The fast-caking limit, $\delta \to \infty$, is mathematically interesting, but not physically sensible as the cake would grow by more than the total volume of the fluid; we therefore discuss it only briefly. For large δ, we obtain from (2.47) to first order

$$\frac{\partial \phi}{\partial T} = 0, \tag{2.59}$$

stating that the porosity is constant, subject to the boundary conditions

$$\phi(0) = \tau^{-1}(\mathcal{P}), \quad \phi(L) = \Phi, \quad \text{and} \quad \frac{\mathrm{d}L}{\mathrm{d}T} = -Q. \tag{2.60}$$

The solution to (2.60) is given by $\phi(x,t) = \Phi$ and a boundary layer would have to be introduced to satisfy the left-hand boundary condition. While the numerical results

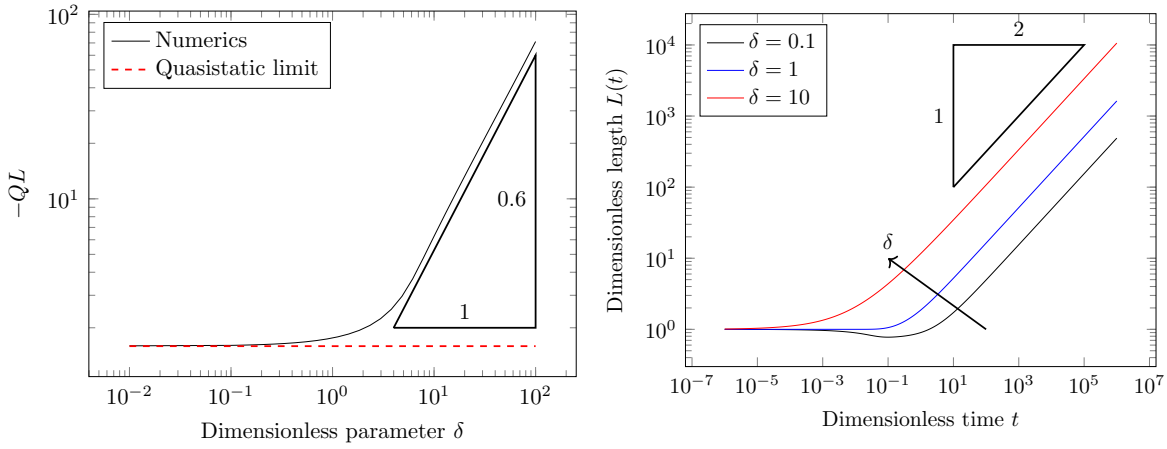

(a) (b)

Figure 2.4: In (a), we show the numerical results for the product QL at $t = 10^6$ for $\Phi = 0.7$ and $\phi(0) = 0.4$ using $N = 1000$ interpolation points. The dashed red line indicates the value for the slow-caking limit and provides an excellent approximation for sufficiently small δ. In (b), we show the length of the porous medium of initial length $L(0) = 1$ for different values of δ, using the same parameters as in (a). The dip for $\delta = 0.1$ corresponds to the initial compression of the filtercake.

shown in 2.4a suggest a relation of the type $-QL \sim \delta^{0.6}$ for sufficiently large δ, we have not been able to derive the relation analytically.

The conventional, compression-free model is not an appropriate model to understand this limit, however. For this instance, we would have that $k = k(\Phi)$ is a constant, the flux Q is given by the applied pressure times the permeability divided by the length of the porous medium, that is

$$Q(T) = -\frac{k(\Phi)\mathcal{P}}{L(T)} = k(\Phi)\mathcal{P}\left(\int_0^T Q(s)\ \mathrm{d}s\right)^{-1}, \tag{2.61}$$

and so we would obtain $-QL = k(\Phi)\tau(0.4) \approx 6.67$ as an upper limit, independent of δ. However, the observed values for $-QL$ are much larger than the predicted value from this model, which is why it remains an interesting problem to find an appropriate scaling and maybe even a physically sensible explanation for the case of $\delta \to \infty$.

2.4.2 Similarity solution in the general case

The numerical results from figure 2.4b suggest that the length evolves as $ct^{1/2}$ for large t and some constant c. If we use $L(0) = 0$ as the initial condition for L, this also suggests that we can hope to find a similarity solution for all $\delta \in (0, \infty)$. Introducing

the self-similar scaling

$$\eta = \frac{x}{ct^{1/2}}, \tag{2.62}$$

where c will be determined later, we introduce $\phi(x,t) = \phi(\eta)$ accordingly. The dimensionless advection–diffusion equation (2.38) now becomes

$$-\frac{c^2\eta}{2}\frac{\partial\phi}{\partial\eta} + ct^{1/2}Q\frac{\partial\phi}{\partial\eta} = -\frac{\partial}{\partial\eta}\left[(1-\phi)k(\phi)\frac{\partial\tau}{\partial\phi}\frac{\partial\phi}{\partial\eta}\right]. \tag{2.63}$$

The left-side boundary condition

$$ct^{1/2}Q = k(\phi)\frac{\partial\tau}{\partial\phi}\frac{\partial\phi}{\partial\eta} \quad \text{at } \eta = 0 \tag{2.64}$$

states that the term $ct^{1/2}Q$ is a constant, which justifies evaluating QL in the previous sections and guarantees that (2.63) is in fact an ODE. The condition for the growth in length now becomes

$$\frac{1}{2}c^2 = ct^{1/2}Q(1-\delta) - k(\phi)\frac{\partial\tau}{\partial\phi}\frac{\partial\phi}{\partial\eta} \quad \text{at } \eta = 1. \tag{2.65}$$

Therefore, we obtain a boundary value problem with two unknown parameters that will govern the expansion of the porous medium. We point out that this similarity solution only exists if there exist such parameters c and $ct^{1/2}Q$ such that all three equations (2.63)–(2.65) are satisfied.

2.5 Cake filtration for constant-flow-rate filtration

Given that the quasi-static compressible-cake-filtration model is a suitable approximation for the parameter ranges of δ that we are interested in, we use this model to study the discrepancies that arise between the conventional model and the compressible-cake-filtration model for constant-flow-rate filtration.

During constant-flow-rate filtration, the applied pressure must be continuously increased to maintain a constant flux as the filtercake grows due to deposition of particles. Therefore, the product of the positive flux and the length, $-QL$, increases for constant-flow-rate filtration. For the constitutive relation that we consider, we see from figure 2.3b that there is a maximum value that $-QL$ can attain, allowing only for a finite running time for the quasi-static caking model. This is also illustrated in figure 2.5a, where $-QL$ plateaus as the ratio between the applied pressure and the matrix pressure $\mathcal{P} \to \infty$, however, in the conventional model $-QL = k(\Phi)\mathcal{P}$ is unbounded as $\mathcal{P}$ becomes arbitrarily large.

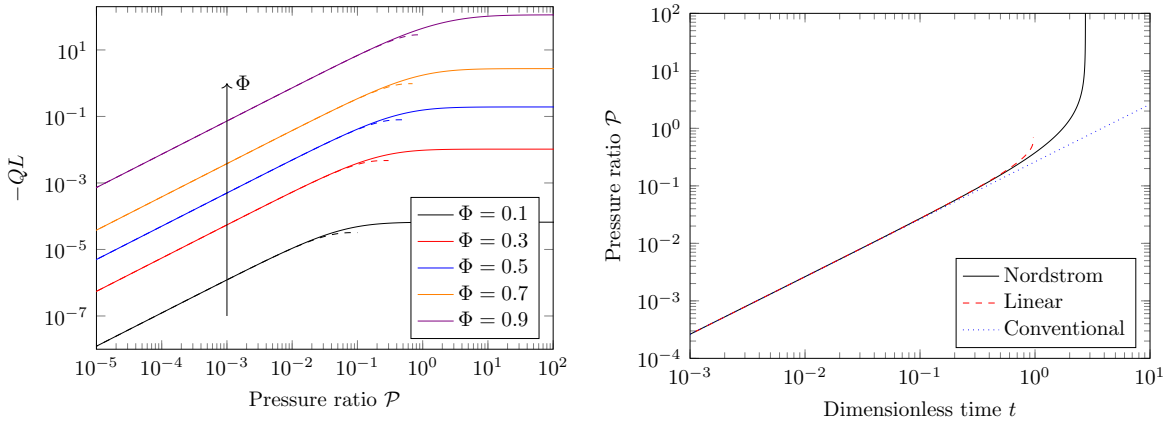

(a) (b)

Figure 2.5: In (a), we compare the results for the product QL for the linear (dashed) and Nordstrom (solid) stress–strain relation, note that there is a maximum pressure that can be applied in the linear model. In (b), we compare the required applied pressure for $Q = 1$ and $\Phi = 0.7$ for the conventional and compression-based model. The two models agree initially but only the compression-based model diverges within finite times.

To compute the necessary applied pressure $\mathcal{P}$, we can use the definitions of the linear (2.19) and Nordstrom (2.18) stress–strain relationships to obtain

$$\phi_{\text{lin}}(0) = \frac{\mathcal{P} - \Phi}{\mathcal{P} - 1} \tag{2.66}$$

in the linear case, and

$$\phi_{\text{nonlin}}(0) = \frac{\Phi^2}{\Phi + \mathcal{P}(1 - \Phi)} \tag{2.67}$$

in the Nordstrom case. We require $\phi \geq 0$, and so the maximum applicable pressure for the linear case is given by $\mathcal{P} = \Phi$, which is of the order of magnitude of the characteristic matrix pressure $\tau^\star$ unless Φ is very small. In the Nordstrom case, we can apply an arbitrarily large pressure because the solid matrix stiffens to prevent arbitrary compression.

To compute the pressure that needs to be applied to maintain a constant flux, equations (2.66) and (2.67) are used together with the computation of $-QL$ (2.55) to determine the applied pressure for $Q = -1$ versus time, the results are shown in figure 2.5b. While the conventional and the compression-based models agree at early times, the discrepancy arises for larger times, as the applied pressure diverges for the compression-based case.

2.6 Conclusion

In this chapter, we developed a two-phase model based on nonlinear elasticity to incorporate compressibility of the filtercake into the conventional cake filtration law. We analysed the two asymptotic limits of slow and fast caking for constant-pressure filtration, where we argued that only the slow-caking limit is physically sensible and corresponds to a quasi-static caking law. Our numerical simulations of the full problem indicated that the quasi-static caking model is a suitable approximation for filtration. We also showed the suitability of treating $-QL$ as a constant by considering the similarity solution of the full problem.

Having established the quasi-static model as a suitable model for constant-pressure filtration, we then used it in the case of constant-flow-rate filtration to illustrate the differences between the conventional and compressible-cake-filtration model. While the conventional caking law allows for an infinite running time, our choice of constitutive relations for the permeability and stress–strain relationship only allows for a finite running time. However, the corresponding applied pressures are typically of the order of the matrix pressure and therefore large, and so this difference will probably not become apparent experimentally.

To conclude, while there is an appreciable theoretical difference between the conventional and compression-based models, our results indicate that there will be no noticeable difference experimentally. For the case of constant-pressure filtration, the similarity solution of the full model provides a result for the growth of L or decrease in Q that is qualitatively similar to the the conventional model, with the only difference being the multiplicative constants. For the case of constant-flow-rate filtration, the finite running time of the compressible-cake-filtration model makes for an appreciable difference, however, the associated pressures ($> 10^6 Pa$, as estimated from the Lamé constants for representative materials) are typically beyond those that are used in membrane filtration experiments ($10^4 Pa$) [74, 101].

Chapter 3

Stochastic modelling of membrane filtration

3.1 Introduction

Filtration models using only a single blocking mechanism are suitable, as demonstrated in Chapter 1, to model a variety of filtration experiments. However, there are several instances where a single blocking mechanism is insufficient to explain for example the decrease in flux during constant-pressure filtration. For instance, Iritani et al. [66] reported that a single blocking filtration law was insufficient to describe their experimental measurements for BSA filtration.

A potential solution to this problem is to combine several filtration laws. Ho and Zydney [57] derived a concurrent model of complete blocking and cake filtration to model protein fouling in dead-end stirred cell filtration, while Mondal and De [86] used a consecutive model for cross-flow filtration. Duclos-Orsello et al. [36] combined standard and intermediate blocking, as well as cake filtration, to obtain good fits to protein microfiltration.

However, even the combination of the four blocking mechanisms, be it concurrent or consecutive, can at times be insufficient to model experimental observations appropriately. Ho and Zydney [56] combined intermediate blocking with a two-resistor model to explain different experimental results for straight-through versus interconnected membranes in protein microfiltration based on the membrane morphology. Bolton et al. [19] considered the special geometry of fibrous membranes to obtain better predictions for glass fibre filters.

The last two examples underline the need to allow for more complex geometries and particle–pore interactions in mathematical models for membrane fouling. In this regard, Dalwadi et al. [31] employed homogenisation techniques to provide a better

understanding of the effect of porosity gradients in depth filters, while Rahimi et al. [98] used full-scale finite element simulations to model membrane filtration in more detail. Sanaei and Cummings [102] introduced a continuum model that allows clogging by sieving and adsorption in complex membrane morphologies. A stochastic simulation approach was proposed by Griffiths et al. [44], who considered a three-step blocking process in a constant-pressure filtration setting. Here, in each pore, uniformly sized particles first constrict the pore by adhesion on the pore wall, then, once the radius of the pore has been sufficiently decreased, partially cover the pore, and then finally stack up to form a filtercake above the pore. This blocking process is assumed to be the same for all pores, and so the flux through a given pore only depends on the number of particles it has retained. To compute the flux decline for the entire membrane they ran multiple stochastic simulations, where the probability of a pore receiving a particle in a given iteration step depended on the flux through it, the flux through the entire membrane was then obtained by summing over the fluxes of the single pores.

Stochastic models have been used to model particle transport and retention in porous media [15, 116, 124] and to provide an alternative approach to explain and model filtration. For example, Hsu and Fan [60] considered the number of blocked pores as a random variable and use the Carman-Kozeny equations to compute the corresponding pressure build-up in a deep porous medium. An alternative derivation of the complete-blocking model was proposed, which fits their experimental observations for filtering coal particles with a deep bed of sand. Iritani et al. [67] used a stochastic model to compute the expected number of retained particles in a filtration experiment. By considering the four blocking mechanisms used for standard, complete and partial blocking, and cake filtration, they obtain alternative derivations of the four conventional filtration laws. Tarafdar et al. [114] modelled the filtration process as a transition between different *states* of the entire membrane, with each state corresponding to a certain flux through the membrane. To model depth filters, which primarily work by retaining particles within the membrane structure and not on the surface, Nassar et al. [89] subdivided depth filters in their model into several compartments to compute the spatial distribution of particles. For standard blocking of a deep porous medium by particles with a given, potentially continuous, size distribution, Shapiro et al. [105] derived a population balance model, which was then averaged to obtain a system of differential equations describing the reduction in permeability due to particle retention.

This chapter builds on several of these ideas by introducing a generalisation of the work of Griffiths et al. [44] to provide a tool to model membrane filtration for more complex particle–pore interactions. We focus on normal-flow filtration in a constant-pressure setup. At the model's core lies the assumption that the blocking process is the same for each pore. With this assumption, it follows that the *conductivity* of a pore, relating the applied pressure to the flux through the pore, only depends on the number of retained particles and, when there are different particle types involved, their order of arrival. We model the filtration as a stochastic process and consider the number of retained particles and their order for a given pore as our random variable. Taking an ensemble average over a large set of pores then allows us to derive a system of ODEs to compute the time-dependent probability distribution for our random variable.

Note that the number and order of arrival of the retained particles for a given pore effectively represents the state of a pore. Considering the state of a pore instead of the state of the entire membrane, however, has the advantage that we can determine the conductivity of a pore for a given state using analytical, numerical, or experimental techniques. Moreover, it allows for insights into the randomness of the filtration as the distribution of the number of particles retained by the pores can be tracked during a simulation. The expected flux through the membrane can be obtained directly from the time-dependent probability distribution of the random variable and the state-dependent conductivity. Thus, this approach allows us to compute the decline in flux across the membrane for any set of particle–pore interactions where a relationship between the number of retained particles by a pore, including their order of arrival in case of different particle sizes, and the conductivity of the pore can be established.

Following the work of Griffiths et al. [45] on using stochastic simulations for interconnected membranes, we also show that this approach can be generalised to interconnected pore geometries. Instead of a compartmentalisation as proposed by Nasser et al. [89], we represent the underlying membrane structure by a network of connected pores, extend the idea of retention-dependent conductivity to the links in the network, and consider the change in pressure distribution through the network due to particle retention.

This chapter is divided into five sections. In Section 3.2, we introduce our approach on the basis of monodisperse particles, which is extended to multi-particle models in Section 3.3. In Section 3.4, we discuss how to adapt our model to membranes with an interconnected pore structure and in Section 3.5, we use these ideas to derive a method for the fast computation of filtration coefficients. Finally, in Section 3.6 we

analyse the continuous equivalents of our discrete models. The results from Sections 3.2 – 3.4 have been published [72]; the results from Sections 3.5 and 3.6 represent additional work that extends the published results.

3.2 Stochastic modelling of normal-flow filtration of monodisperse particles

3.2.1 A basic model of membrane filtration

We begin by considering the simplest membrane, comprising a solid material containing a number, N, of circular and non-interconnected holes called pores that run from one side of the membrane to the other. This type of structure describes, for example, track-etched membranes [4], where the pores are usually cylindrical or cone-shaped; a schematic is shown in figure 3.1a.

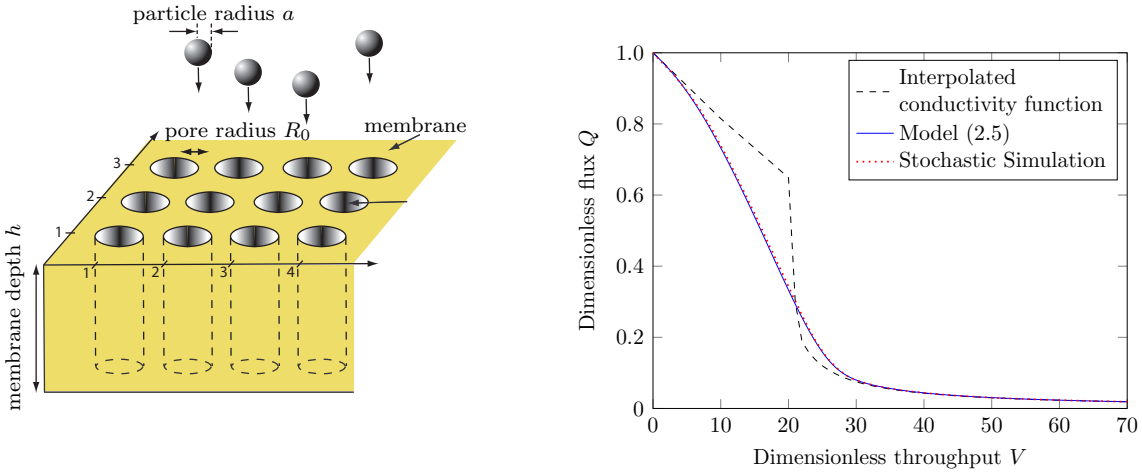

(a) (b)

Figure 3.1: (a) Schematic diagram of a portion of the membrane setup considered. (b) Flux (Q) versus throughput (V) graph for the stochastic simulation and ODE-model (3.5) for the conductivity function (3.7), contrasted with the results for interpolated conductivity function. The stochastic simulation and our ODE model show excellent agreement, while the stark difference between the expected flux and the interpolated conductivity function underlines the difference between pore-level and membrane-level behaviour.

The particles in the fluid are assumed to be uniform in shape and size. Furthermore, we assume that the concentration c of the particles in the fluid is constant, and that the particles do not interact. As the fluid passes through the pores of the membrane the particles are potentially retained with *retention probability* P_R. The

underlying mechanisms behind the retention are usually complex: they can be of physical or chemical nature, depend on properties of the particles and the membrane, and may change over the course of the filtration process.

We assume that the pores retain the particles in an identical way, that is, two pores having retained the same number of particles are assumed to be indistinguishable. Therefore, both the retention probability and the flux f through a given pore only depend on the number n of particles the pore has retained and the applied pressure difference Δp across the membrane, that is, $P_R = P_R(n, \Delta p)$ and $f = f(n, \Delta p) = \tilde{\kappa}(n)\Delta p$, where $\tilde{\kappa}(n)$ denotes the *conductivity* of a pore with n retained particles. The last equality follows from the linearity of the Stokes equations, which describe the low-Reynolds-number flow encountered in membrane filtration of liquids. The conductivity function $\tilde{\kappa}$ will be a central concept in this work. This depends on several parameters, such as the geometry of the pores and the material properties of the membrane, and must be determined by analytical, computational, or experimental considerations. The conductivity function is usually a decreasing function of n.

In typical constant-pressure filtration experiments, the flux $\tilde{Q}$ through the membrane is measured against the throughput $\tilde{V}$, the time-integral of the flux. For unit retention probability, we might anticipate that the flux through the entire membrane after processing a volume $\tilde{V}$ of fluid is simply the sum of the average flux through an individual pore after that time, i.e. $N\ \tilde{\kappa}(c\tilde{V}/N)\Delta p$, using linear interpolation whenever $c\tilde{V}/N$ takes a non-integer value. However, the measured flux $\tilde{Q}(\tilde{V})$ typically differs significantly from this expression. Hence the average behaviour of the flow through the pores, as seen in the flux, is not the behaviour of a pore with the average number of particles. The conductivity function $\tilde{\kappa}$ only describes the impact of particle retention on the flux through a single pore, whereas $\tilde{Q}(V)$ combines this impact with the stochastic behaviour of the system composed of several pores. In the next section, we will therefore describe how to obtain the flux ($\tilde{Q}$) – throughput ($\tilde{V}$) relationship from the conductivity function by accounting for the stochastic nature of the filtration process.

3.2.2 Derivation of evolution equations

From the assumptions of uniform concentration c of the particles in the fluid and no particle–particle interaction, it follows that the number of particles in a given volume $\Delta\tilde{V}$ of fluid is Poisson distributed with parameter $c\Delta\tilde{V}$. Hence, membrane filtration is fundamentally a stochastic process and the measured flux $\tilde{Q}$ against throughput $\tilde{V}$ constitutes an outcome of this stochastic process.

As the pressure difference Δp across the membrane is uniform and the pores are non-interconnected, the flux through a given pore only depends on the number of retained particles and not on the flux through the other pores. Hence, the stochastic processes describing the filtration for the individual pores are independent of each other. Typical membranes have a large number of pores, and so the flux measurements will be close to the expected outcome of the stochastic process of the individual pores. This justifies framing filtration as a deterministic process and our goal is to determine the expected flux $\tilde{Q}_e$ as a function of time, from which we can derive the relationship as a function of volume.

For a given pore $i \in \{1, \dots, N\}$, we introduce the time-dependent random variable $X_i(\tilde{t})$, counting the number $n \in \mathbb{N}_0$ of particles retained by the pore at time $\tilde{t} \geq 0$. We denote the probability of the pore having n particles at time $\tilde{t}$ by $P_X(n, \tilde{t}) := \mathbb{P}(X(\tilde{t}) = n)$. The measured flux $\tilde{Q}_m$ and the expected flux $\tilde{Q}_e$ are then given by

$$\begin{aligned} \tilde{Q}_m(\tilde{t}) &= \sum_{i=1}^{N} \tilde{\kappa}(X_i(\tilde{t}))\Delta p \\ \text{and} \quad \tilde{Q}_e(\tilde{t}) &= \sum_{i=1}^{N}\sum_{n=0}^{\infty} \tilde{\kappa}(n) P_{X_i}(n, \tilde{t})\Delta p \;=\; N\sum_{n=0}^{\infty} \tilde{\kappa}(n) P_X(n, \tilde{t})\Delta p. \end{aligned} \tag{3.1}$$

To obtain the expected flux $\tilde{Q}_e$ we need to obtain the evolution equation for P_X. We consider the change in P_X over a short time-period $\Delta\tilde{t}$, chosen to be small enough such that the probability of more than one particle arriving during this time is small. A pore will contain n particles at time $\tilde{t} + \Delta\tilde{t}$ if it contains n particles at time $\tilde{t}$ and does either not receive a particle during the interval $\Delta\tilde{t}$ or does not retain the particle it receives. This happens with probability

$$\begin{aligned} P &= P_X(n, \tilde{t}) \left[\mathrm{Poi}(0, \Delta\tilde{t}\ c\ \tilde{\kappa}(n)\Delta p) + (1 - P_R(n))\,\mathrm{Poi}(1, \Delta\tilde{t}\ c\ \tilde{\kappa}(n)\Delta p) + O\left(\Delta\tilde{t}^2\right)\right] \\ &= P_X(n, \tilde{t}) \left[1 - P_R(n)\Delta t\ c\ \tilde{\kappa}(n)\Delta p \exp\left(-\Delta\tilde{t}\ c\ \tilde{\kappa}(n)\Delta p\right) + O\left(\Delta\tilde{t}^2\right)\right], \end{aligned} \tag{3.2}$$

where we used the shorthand $P_R(n) = P_R(n, \Delta p)$ as the pressure difference is constant, $\mathrm{Poi}(n, \lambda)$ denotes the probability $\mathbb{P}(Y = n)$ where Y is Poisson distributed with parameter λ, and the $O(\Delta t^2)$ correction accounts for the probability of retaining more than one particle in this time interval. A pore can also contain $n \geq 1$ particles at time $\tilde{t} + \Delta\tilde{t}$ by containing $n-1$ particles at time $\tilde{t}$ and retaining one particle during the time interval $\Delta\tilde{t}$. This happens with probability

$$\begin{aligned} P &= P_X(n-1, \tilde{t})\ P_R(n)\ \mathrm{Poi}(1, \Delta\tilde{t}\ c\ \tilde{\kappa}(n-1)\Delta p) + O\left(\Delta\tilde{t}^2\right) \\ &= P_X(n-1, \tilde{t}) \left[P_R(n)\ \Delta\tilde{t}\ c\ \tilde{\kappa}(n-1)\Delta p \exp\left(-\Delta\tilde{t}\ c\ \tilde{\kappa}(n-1)\Delta p\right)\right] + O\left(\Delta\tilde{t}^2\right), \end{aligned} \tag{3.3}$$

where the $O\left(\Delta\tilde{t}^2\right)$ correction accounts for the probability of retaining more than one particle during the time interval and having contained correspondingly fewer particles at time $\tilde{t}$.

Combining equations (3.2) and (3.3), letting $\Delta\tilde{t} \to 0$, scaling $\tilde{t} = (c/(\tilde{\kappa}(0)\Delta p))t$, so that on average initially one particle is expected to arrive in each pore per unit time step, $\tilde{Q} = \tilde{Q}(0)Q$, $\tilde{V} = (\tilde{Q}(0)c/N\tilde{\kappa}(0)\Delta p)V$, and $\tilde{\kappa}(n) = \tilde{\kappa}(0)\kappa(n)$ we obtain the dimensionless governing equations for the probability P_X as

$$\begin{aligned} \frac{\mathrm{d}P_X(n,t)}{\mathrm{d}t} &= -P_R(n)\kappa(n)P_X(n,t) + P_R(n-1)\kappa(n-1)P_X(n-1,t), \quad n \geq 1, \\ \frac{\mathrm{d}P_X(0,t)}{\mathrm{d}t} &= -P_R(0)P_X(0,t), \end{aligned} \tag{3.4}$$

with initial conditions $P_X(0,0) = 1$ and $P_X(n,0) = 0\ \forall n \geq 1$. Note that mass is conserved by summing the equations for $P_X(\cdot,t)$ over all n.

As the flux is usually plotted against the throughput V, it is useful to rewrite (3.4) in terms of the expected throughput V_e by using $\mathrm{d}V_e/\mathrm{d}t = Q_e$, which gives

$$\begin{aligned} \frac{\mathrm{d}P_X(n,V_e)}{\mathrm{d}V_e} &= \frac{1}{Q_e(V_e)}\left[-P_R(n)\kappa(n)P_X(n,V_e) + P_R(n-1)\kappa(n-1)P_X(n-1,V_e)\right], \quad n \geq 1, \\ \frac{\mathrm{d}P_X(0,V_e)}{\mathrm{d}V_e} &= -\frac{1}{Q_e(V_e)}P_R(0)P_X(0,V_e), \end{aligned} \tag{3.5}$$

with the same initial conditions $P_X(0,0) = 1$ and $P_X(n,0) = 0\ \forall n \geq 1$ as for (3.4).

It is possible to obtain a closed-form solution for P_X for any κ. In the simplest case where $P_R\kappa = 1$ for all $n \geq 0$, we find that $P_X(n,t) = t^n/(n!)\exp(-t)$, the moments of the Poisson distribution with parameter 1, and that the flux Q_e is constant. In the case of a unit retention probability $P_R \equiv 1$ and a strictly decreasing conductivity function κ, that is $1 = \kappa(0) > \kappa(1) > \ldots$, which is expected to be the case in a filtration experiment, we obtain

$$Q_e(t) = \sum_{n=0}^{\infty}\kappa(n)P_X(n,t) = \sum_{n=0}^{\infty}\kappa(n)\left[\sum_{k=0}^{n}\left(\prod_{i=0,i\neq k}^{n}\frac{1}{\kappa(i)-\kappa(k)}\right)\exp(-\kappa(k)t)\right]. \tag{3.6}$$

Other cases for the retention probability and conductivity function can be computed in a similar fashion using integrating factors.

It is important to note that, although we can compute an exact solution for an arbitrary retention probability P_R and conductivity function κ, the closed form is not particularly useful as the evaluation of the product in (3.6) is numerically unstable. Therefore, numerical solution of (3.4) is the preferred method.

For simplicity, we have restricted ourselves in the derivation of equation (3.4) to a single-particle system with a one-dimensional state space, namely the number of retained particles by a pore. However, we can model more complex configurations that might occur within a pore, such as bridging, by introducing a multi-dimensional state space, where different states can correspond to different aggregations of the same number of particles within a pore or by subdividing the pore into several sections. The necessary techniques and generalisations for this are developed in Sections 3.3 and 3.4.

3.2.3 Comparison with a three-stage fouling model

Modelling filtration as a stochastic process is especially useful if there are different mechanical stages in the fouling of a pore. We compare our methods with the work of Griffiths et al. [44], who evaluate a three-stage fouling process using stochastic simulations on a fixed number of identical pores.

The three stages arise as the cylindrical pores have a larger radius than the spherical particles, allowing for the particles to enter the pores. Once a particle has entered a pore, it either adheres to the pore wall with retention probability P_R or passes through. The analysis we present holds for pore-radius- or time-dependent probabilities but here we shall assume that P_R is constant. It is assumed that the reduction in radius due to particle adhesion is uniform within the pore, so that a pore with initial radius R_0 containing n particles has radius $R_n = \sqrt{R_0^2 - n\ 4a^3/3h}$, where a denotes the radius of the particles and h the depth of the pore; this is known as *standard blocking*. The new, reduced flux $\tilde{Q}_n$ through the pore can then be computed by using Poiseuille's law as $\tilde{Q}_n = \Delta p R_n^4/8\mu h$, where μ denotes the fluid viscosity.

As each retained particle decreases the radius of the pore, the maximum number of admissible particles per pore is given by $n^\star = \left\lceil \frac{3(R_0^2 - a^2)h}{4a^3} \right\rceil$, which follows from requiring $R_n \geq a$ for a particle to enter the pore. Once the pore has a smaller radius than the particles due to this constriction, it enters the second stage, where the next particle that arrives at the pore will cover it, allowing for a fixed residual flux $\tilde{Q}_{\text{res}} = \tilde{\kappa}_{\text{res}} \Delta p$. After the pore has been covered, subsequent particles reaching the pore will stack on top of each other in the third stage, forming a filtercake. The filtercake imposes an additional resistance that is proportional to its height.

Combining these three stages, we can infer the dimensionless conductivity function

$\kappa = \tilde{\kappa}/\tilde{\kappa}(0)$ for the pore as

$$\begin{aligned} &\text{(first stage: constriction)} \quad \kappa(n) = \left(1 - n\frac{4a^3}{3hR_0^2}\right)^4, \quad n \le n^\star, \\ &\text{(second stage: covering)} \quad \kappa(n) = \kappa_{\text{res}}, \quad n = n^\star + 1, \\ &\text{(third stage: caking)} \quad \kappa(n) = \left((\kappa_{\text{res}})^{-1} + r(n - n^\star)\right)^{-1}, \quad n \ge n^\star + 2, \end{aligned} \tag{3.7}$$

where the dimensionless parameter r relates the number of particles in the filtercake to its resistance.

To evaluate the flux–throughput behavior of this model, in Griffiths et al. [44], N=144 pores were considered taking the average over several stochastic simulations using the following algorithm:

1. Subdivide the throughput V into equal volume steps $V_k = k\Delta V := k/c,\ k = 1, 2, \ldots,$ where c is the particle concentration (number of particles per unit volume), so that at each step a particle arrives at the membrane.

2. At each volume step V_k, choose the pore to which the particle is assigned to, with the probability P_j of a given pore j receiving the particle being $P_j = \kappa(n_j(V_{k-1}))/Q(V_{k-1})$, where $n_j(V_{k-1})$ denotes the number of particles retained by pore j after volume V_{k-1} has been processed by the membrane.

3. If the particle, with probability $P_R(n_j(V_{k-1}))$, is retained, update the number of retained particles of the pore that received the particle and continue.

To compute the expected flux Q_e for the conductivity function κ defined by (3.7), we first solve (3.5) where we extend the definition of $P_R(n)$ via $P_R(n) = 1$ if $n \ge n^\star$ and $P_R(n) = 0.1$ otherwise, r was chosen to be 1, $a = 0.9$, $h = 10$, $R_0 = 1$, and $\kappa_{\text{res}} = 0.3$. For a given volume V, we can then obtain $Q_e(V)$ using the same approach as in (3.1).

The solution to the system of ODEs (3.5) is shown in figure 3.1b to provide almost exact agreement with the stochastic model of Griffiths et al. [44]. The figure also crucially highlights the difference between the observed flux–throughput behaviour and the interpolated conductivity function that would be predicted if we assumed that the particles were equidistributed across the pores during the filtration. For a given non-zero retention probability P_R, the expected dimensionless volume that is processed before a particle is retained is P_R^{-1}. Therefore, we choose interpolation points $(V_i, \kappa(i))$ with $V_i = \sum_{k=0}^{i-1} P_R(k)^{-1}$ for plotting the conductivity function. This demonstrates why our model is essential to traverse from the microscopic level of the individual pore to the macroscopic level of the entire membrane. As the number of

pores in a typical membrane is large, computing the expected flux Q_e is sufficient to predict the measured flux–throughput behaviour. Compared with the stochastic simulation, solving the evolution equation (3.5) offers a significantly faster and easy-to-implement method for this computation. In our simulations, we achieved a speedup of three orders of magnitude and needed only a fraction of the lines of code.

3.2.4 Multiple-pore-geometry membranes

A multiple-pore-geometry membrane contains several types of differently shaped unconnected pores instead of a single pore type as assumed in the previous subsections. It is appropriate to consider these types of membranes because different pore geometries can be created in a single membrane either on purpose or due to imperfections in the manufacturing process.

For a membrane with K different types of pores, we can adapt the stochastic model to multiple-pore-geometry membranes by introducing representative random variables X_k counting the number of particles retained by pore type $k \in \{1, \dots, K\}$, κ_k denoting its conductivity function, P_{R_k} its retention probability, and P_{X_k} the probability distribution of X_k. As the flux through a given pore only depends on the number of particles retained by the pore, the time-dependent evolution equations for the different pore types are independent of each other. Hence, we can solve equation (3.4) for each pore type $k \in \{1, \dots, K\}$ and then sum the different expected fluxes to obtain the total flux through the membrane. Specifically, if N_k denotes the number of pores of type k, we obtain the total expected dimensionless flux Q_e through the membrane as

$$Q_e(t) = \sum_{k=1}^{K} N_k \sum_{n=0}^{\infty} \kappa_k(n) P_{X_k}(n,t). \tag{3.8}$$

To obtain the volume-dependent evolution equation, we have to use (3.8) to compute the flux and take into account the number of pores of each type, hence

$$\begin{aligned} \frac{\mathrm{d}P_{X_k}(n,t)}{\mathrm{d}V_e} &= \frac{N_k}{Q_e(V_e)} \left[-P_{R_k}(n)\kappa_k(n)P_{X_k}(n,t) + P_{R_k}(n-1)\kappa_k(n-1)P_{X_k}(n-1,t) \right], \quad n \geq 1, \\ \frac{\mathrm{d}P_{X_k}(0,t)}{\mathrm{d}V_e} &= \frac{N_k}{Q_e(V_e)} \left[-P_{R_k}(0)\kappa_k(0)P_{X_k}(0,t) \right], \end{aligned} \tag{3.9}$$

with initial conditions $P_{X_k}(0,0) = 1$, $P_{X_k}(n,0) = 0 \ \forall n \geq 1 \ \forall K \in \{1, \dots, k\}$.

We point out that the independence in the time evolution for the different pore types allows us to formulate the optimal pore-type composition of a membrane as an

optimisation problem of a linear objective function, however, the constraints are not necessarily linear. When designing a membrane, a standard goal is to maximise the expected throughput $V_e(T) = \int_0^T Q_e(t)\mathrm{d}t$ of a membrane after time T in constant-pressure filtration by choosing the right mixture of pores $N_1, \ldots, N_k$. Rearranging the expected throughput as

$$V_e(T) = \sum_{k=1}^{K} N_k \int_0^T \sum_{n=0}^{\infty} \kappa_k(n) P_{X_k}(n,t)\ \mathrm{d}t =: \sum_{k=1}^{K} N_k V_k(T), \tag{3.10}$$

we see that obtaining a membrane with maximum expected throughput is in fact simply a packing problem, where we want to cover the surface of the membrane with the pore inlets such as to maximise (3.10). Packing problems are in general hard problems, for which no efficient optimisation algorithms exist. However, if the pore inlets have to be arranged on some lattice instead so that the total number of pores $N = N_1 + \ldots + N_K$ is prescribed, the maximum throughput will be attained by choosing only pores of type k where $V_k = \max\{V_1, \ldots, V_K\}$.

While this conclusion is as we would expect, we have highlighted the methodology that may be adopted to consider membranes with multiple pore geometries and that such generalisations are simple to include within our framework. In the remaining sections, we will return to single-pore-type models, but emphasize that all models can be extended to membranes with multiple pores using the results from this section.

3.3 Multi-particle systems

3.3.1 A two-particle system

We now turn our attention to the filtration of a fluid containing two types of particles: *small* particles, having a radius less than that of the pores, and *large* particles, having a radius bigger than that of the pores. We denote their concentrations by $\tilde{c}_s$ and $\tilde{c}_l$, respectively. As in the previous section, we consider a membrane of fixed depth h with cylindrical, non-interconnected pores of uniform radius R_0 and apply a constant transmembrane pressure Δp.

This two-particle model is a good approximation for filtering the protein bovine serum albumin (BSA) with sterile membranes having a pore diameter of around $200nm$. Protein monomers in general can aggregate to large polymers due to a variety of factors, even under operating conditions where the monomer state is highly favoured [26]. While BSA monomers have diameters of around $10nm$, the aggregated polymers can grow larger than the pore diameter. As an example, Ho and Zydney

measured particle-size distributions between 100 to $450nm$ for the BSA aggregates in a filtration experiment [56].

Having two types of particles extends the range of possibilities for a pore to foul. While small particles will enter the pores where, if retained with probability P_R, they constrict the pore, particles that exceed the pore size will cover the pore entrance, allowing for a residual flux but making it impossible for any further small particles to enter the pore. Therefore, once a pore has been sealed, both small and large particles will stack up on the surface, forming a filtercake. For this model, we neglect the possibility of particles in the filtercake being released back into the fluid or filtercakes of neighbouring pores interacting with each other. The interaction between neighbouring filtercakes can be modelled by including pore–pore interactions as discussed in Section 3.4, whereas the release of particles back into the fluid would have to be dealt with by including additional terms in the governing equations (3.14) and (3.15).

Until the pore has been covered, we only have to keep track of how many small particles have been retained inside the pore. As soon as the pore is covered, we also have to keep track of the depth of the filtercake, that is, we need to know how many small and large particles have been retained on the surface of the pore. We will identify the number of small particles n inside the pore and the number of large particles l and small particles m on the surface of the pore as the *state* of the pore; it is denoted by the triplet (n, l, m). A pore transitions from one state to another when it retains a particle. The newly attained state depends on the previous state as well as the particle that is being retained, we use the $\mid$ sign to distinguish between two states that are attainable if either a small or a large particle is retained. As in Section 3.2.3, we assume that there is a maximum number $n^\star$ of small particles that can be retained within a pore and every particle that arrives at the pore thereafter is retained on the surface. If no large particle has been retained yet, we therefore have to distinguish between these two cases:

$$\begin{aligned} (n,0,0) &\longrightarrow (n+1,0,0) \mid (n,1,0),\ n < n^\star, \\ (n^\star,0,m) &\longrightarrow (n^\star,0,m+1) \mid (n^\star,1,m). \end{aligned} \tag{3.11}$$

Once a large particle has been retained, all particles are retained on the surface and so

$$(n,l,m) \longrightarrow (n,l,m+1) \mid (n,l+1,m),\ l \geq 1. \tag{3.12}$$

To obtain the conductivity function, we adapt the analysis from Section 3.2.3, assuming that the radius of the pore shrinks in response to the deposition of particles

so that we obtain an average pore constriction following the retention of each particle. In addition to the previous conductivity function (3.7), we introduce a further parameter $\beta \in [0,1]$ to control the conductivity of a constricted pore. This is motivated by findings of Bowen and Gan [21], who observed a flux through fully constricted pores. Once the pore has been covered, all particles contribute to the formation of the filtercake which acts as an additional resistor in series, its resistance being proportional to the number of retained small and large particles. Hence, the total resistance of the pore is the resistance of the constricted pore and the resistance of the filtercake, and so the dimensionless conductivity is given by

$$\kappa(n,l,m) = \left(\left(1 - \beta n \frac{4a^3}{3hR_0^2} \right)^{-4} + l\ r_l + m\ r_s \right)^{-1}, \quad n \leq n^\star, \tag{3.13}$$

where a denotes the radius of a small particle, h the depth of the membrane, and r_l, r_s relate the number of large and small particles, respectively, to the resistance of the filtercake. Reducing the parameter β increases the residual flux through a fully constricted pore.

To compute the probability density function for the random variable X, indicating the state (n,l,m) a given pore is in, note that the time-dependent evolution of the different pores is independent and the Poisson parameters for the transitions are given, as before (see, for example, equation (3.2)), by $\tilde{c}_s \tilde{\kappa}(0) \kappa(X(t)) \Delta p$ and $\tilde{c}_l \tilde{\kappa}(0) \kappa(X(t)) \Delta p$, where $\tilde{\kappa}(0)$ denotes the dimensional conductivity of an unconstricted pore. Using (3.11), scaling $\tilde{t} = ((\tilde{c}_s + \tilde{c}_l)/(\kappa(0)\Delta p))t$, $c_s = \tilde{c}_s/(\tilde{c}_s + \tilde{c}_l)$, and $c_l = \tilde{c}_l/(\tilde{c}_s + \tilde{c}_l)$, so that initially one particle, either large or small, is expected to arrive per unit time step and c_s and c_l are the fractions of small and large particles, we obtain for (3.11)

$$\begin{aligned}
\frac{\mathrm{d}P_X\left((n,0,0),t\right)}{\mathrm{d}t} &= -\left(c_s\ P_R(n) + c_l\right)\ \kappa\left(n,0,0\right)\ P_X((n,0,0),t) \\
&\quad + \mathbb{1}_{n>0}\ c_s\ P_R(n-1)\ \kappa(n-1,0,0)\ P_X((n-1,0,0),t), \quad n \leq n^\star, \\
\frac{\mathrm{d}P_X\left((n^\star,0,m),t\right)}{\mathrm{d}t} &= -\kappa\left(n^\star,0,m\right)\ P_X((n^\star,0,m),t) \\
&\quad + \mathbb{1}_{m=0}\ c_s\ P_R(n^\star-1)\ \kappa(n^\star-1,0,0)\ P_X((n^\star-1,0,0),t) \\
&\quad + \mathbb{1}_{m>0}\ c_s\ \kappa(n^\star,0,m-1)\ P_X((n^\star,0,m-1),t),
\end{aligned} \tag{3.14}$$

where $\mathbb{1}$ denotes the indicator function taking value 1 if the associated condition is satisfied and 0 otherwise. Note that the retention probability P_R is only relevant for small particles while they can still enter the pore and so only depends on n. Similarly,

for (3.12) we have

$$\begin{aligned}\frac{\mathrm{d}P_X((n,l,m),t)}{\mathrm{d}t} &= -\kappa(n,l,m)P_X((n,l,m),t)\\ &+ c_l\ \kappa(n,l-1,m)\ P_X((n,l-1,m),t)\\ &+ \mathbb{1}_{m>0}\ c_s\ \kappa(n,l,m-1)\ P_X((n,l,m-1),t), \quad l \geq 1.\end{aligned} \tag{3.15}$$

As before, we can obtain the expected dimensionless flux Q_e by summing over all possible states:

$$Q_e(t) = \sum_{n=0}^{n^\star} \sum_{l,m\in\mathbb{N}} \kappa(n,l,m)P_X((n,l,m),t). \tag{3.16}$$

We consider the impact of the fraction of small particles c_s on the results of the membrane filtration based on the conductivity function (3.13) in figure 3.2. We contrast the effect of the residual flux in a completely constricted pore by considering the cases $\beta = 1$, which corresponds to a low residual flux through the fully constricted pore, and $\beta = 0.1$, which corresponds to to a large residual flux through the pore. For a low residual flux, the flux versus throughput relationship is convex, whereas for a large residual flux, the relationship is initially concave and then convex.

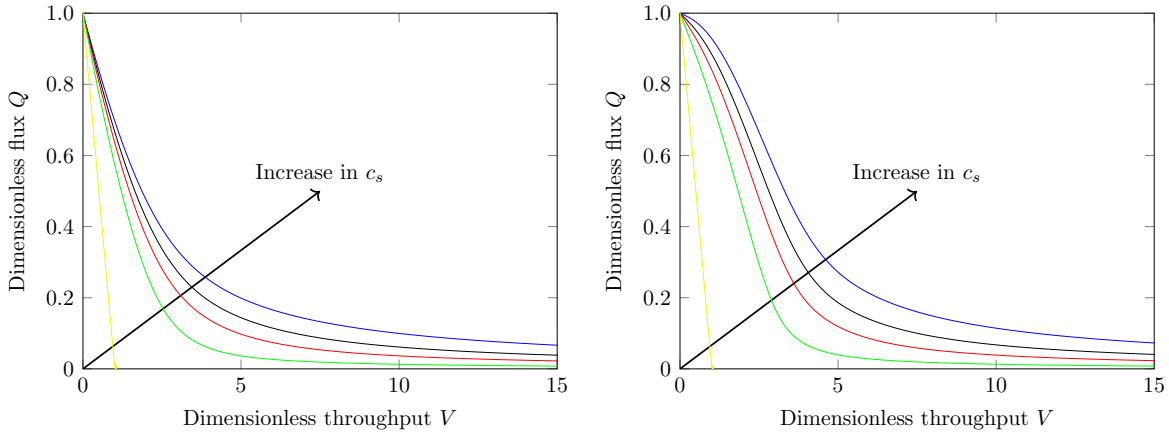

(a) (b)

Figure 3.2: The effect of the residual flux parameter β and the ratio of large particles c_l on the flux (Q) versus throughput (V) relationship for the conductivity function (3.13) with parameters $a = 0.9$, $h = 10$, $R_0 = 1$, $r_s = 1$, $r_l = 10$ and (a) $\beta = 1$ and (b) $\beta = 0.1$. The values for the ratio c_s are $0, 0.8, 0.9, 0.95, 1$, and $P_R \equiv 1$.

3.3.2 General form of multi-particle models

For the general multi-particle problem, if we assume that there are J different types of particles then the state space can be represented by the set of ordered sequences

of finite length, $[J]^{\mathbb{N}_0}$. To derive the evolution equations for the probability P_X of the random variable X, we use the notation

$$\sigma \xrightarrow{c_{\sigma\tau}} \tau, \tag{3.17}$$

denoting that a pore can transition from state σ to state τ, where $\sigma, \tau \in [J]^{\mathbb{N}_0}$, and that the relative concentration of the corresponding particles for the transition is $c_{\sigma\tau}$, their state-dependent retention probability is denoted by $P_R(\sigma, \tau)$. The evolution equation for the probability P_X is then obtained by considering, for a given state σ, the probability of being in state σ and transitioning to τ and the probability of being in a state γ and transitioning to state σ, yielding

$$\begin{aligned} \frac{\mathrm{d}P_X(\sigma,t)}{\mathrm{d}t} = &- \left(\sum_{\{\tau:\sigma\to\tau\}} c_{\sigma\tau}\ P_R(\sigma,\tau) \right) \kappa(\sigma)\ P_X(\sigma,t) \\ &+ \left(\sum_{\{\gamma:\gamma\to\sigma\}} c_{\gamma\sigma}\ P_R(\gamma,\sigma)\ \kappa(\gamma)\ P_X(\gamma,t) \right). \end{aligned} \tag{3.18}$$

Note, however, that the set of ordered sequences of length at most L contains $(1 - J^{L+1})/(1 - J) \geq J^L$ elements, hence the state space for general problems will quickly become too large to be dealt with efficiently. If we cannot use state-space reduction schemes as described in Section 3.3.1, Monte Carlo methods may be a viable alternative to obtain an approximation for the expected flux instead.

3.4 Modelling membranes with interconnected pore structure

3.4.1 General modelling strategy

Although the stochastic model developed in this chapter is motivated by track-etched membranes with non-interconnected pores, it can also be applied to membranes with an interconnected pore structure, such as polyvinyl difluoride (PVDF) membranes [123]. In an interconnected pore structure, the inlets on the top surface of a membrane are connected to multiple outlets on the bottom surface and vice versa. In this case there may be several paths through the membrane between connected inlets and outlets. Membranes with an interconnected pore structure exhibit a different flux–throughput behaviour to track-etched membranes in various filtration experiments [56].

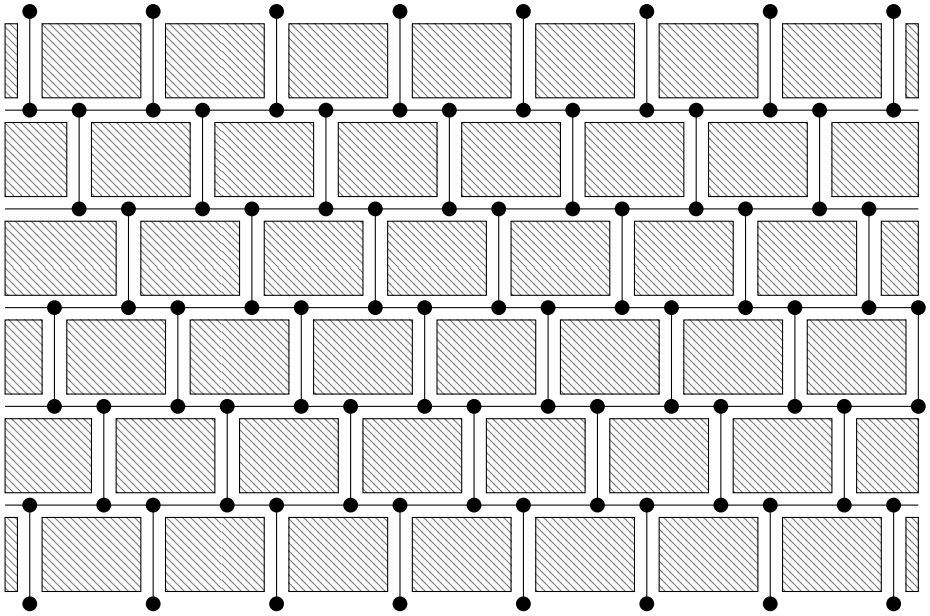

Figure 3.3: Representation of the internal membrane structure by superimposing an undirected graph onto the cross-section of a porous medium.

In order to evaluate the contribution of the membrane geometry to this differing behaviour, we represent the membrane structure beneath a given area, e.g. a square, by an undirected graph as shown in figure 3.3. The edges of the graph are identified with the pores discussed in the previous sections. However, they now no longer run all the way through the membrane but connect junctions instead, represented by the nodes in the graph. Accordingly, particles retained on the surface or within the membrane alter the conductivity of the corresponding edge and the state of an edge is given by the number and order of arrival of the particles the edge has retained. The flux through a given edge depends on the pressure above and below the pore and hence not only on the state of that edge but also on the states of the other edges in the network. We therefore introduce the state of the network as the Cartesian product of the states of the edges in the network.

We assume that the expected time for retaining a particle within the network is much smaller than the expected time between two particles arriving, and so the particle arriving in the structure is retained before the next particle arrives. Thus, the network transitions from one state σ to another state τ if the two states differ by an edge e having retained one more particle in τ than in σ, which we denote by $\sigma \xrightarrow{e} \tau$. The derivation of the evolution equation for the probability distribution of the state of the network, similar to (3.4) and (3.18), is divided into two steps. For a given state σ of the network, we first compute the pressure distribution within the

network. Then, for each edge e, we compute the probability for e to retain the next particle.

As for the pores in the previous sections, the state-dependent conductivity function for a given edge can be computed either analytically or numerically, or determined experimentally. The pressure distribution in the network of state σ can then be obtained by solving the corresponding set of linear equations that arise due to conservation of mass: for a given node v, let p_v denote the pressure at the corresponding junction, for an edge $e = e(u, v) = e(v, u)$ connecting vertices u, v, let $\kappa(e, \sigma) = \kappa(e(u, v), \sigma)$ denote its conductivity. If the node is located at the upper or lower surface of the membrane, we have $p_v = p_{in}$ or $p_v = p_{out}$ as boundary conditions, as we assume that the inlet and outlet pressures are constant. Within the network, we have conservation of mass, implying for every node v

$$\sum_{u \in C(v)} \kappa(e(v, u), \sigma)(p_v - p_u) = 0, \tag{3.19}$$

where $C(v)$ denotes the set of nodes u that v is connected to. In order to obtain a unique solution to the resulting set of linear equations, we only consider those vertices that can be reached from either one of the inlet or outlet nodes via a path of edges having non-zero conductivity.

In the previous models the concentration of particles arriving at a pore was known and constant. However, in a network the concentration of particles in the fluid leaving a pore may change as particles are being retained. As a consequence, the Poisson parameter $\Lambda(\sigma, \tau)$ for the transition $\sigma \xrightarrow{e} \tau$ between two states σ, τ is no longer given by the product of the concentration $c_{\sigma\tau}$, the flux, and the retention probability $P_R(e, \sigma, \Delta p(e, \sigma))$ alone, with $\Delta p(e, \sigma)$ denoting the (positive) pressure difference across e. We now also have to factor in the probability of a particle reaching the edge e in the first place. For a particle to reach the edge e, it has to traverse the network along a path ending in e without being retained. Since the particles travel with the fluid, the pressures in the nodes of the path have to be decreasing and so there is only a finite number of these paths. At every node v, since there can be multiple edges to travel along, we assume that the probability $P_J(l, \sigma)$ of taking an edge l leading to a node u with lower pressure is given by the flux through l divided by the sum of the fluxes of the edges leading from v to nodes with lower pressure. Thus, we obtain the

Poisson parameter

$$\Lambda(\sigma,\tau) = c_{\sigma\tau}\ \kappa(e,\sigma)\Delta p(e,\sigma)\cdot \left[P_R(e,\sigma,\Delta p(e,\sigma)) \sum_{w\in \mathrm{Paths}(e)} \prod_{l\in w\setminus e} P_J(l,\sigma)\left[1-P_R(l,\sigma,\Delta p(l,\sigma))\right]\right], \tag{3.20}$$

where Paths denotes the set of all paths with decreasing pressure on the nodes that end with e. Note that the Poisson parameter defined in (3.20) is independent of time and only depends on the state of the network.

Similar to equation (3.18), we obtain

$$\frac{\mathrm{d}P_X(\sigma,t)}{\mathrm{d}t} = -\left(\sum_{\{\tau:\sigma\to\tau\}} \Lambda(\sigma,\tau)\right)\ P_X(\sigma,t) + \left(\sum_{\{\gamma:\gamma\to\sigma\}} \Lambda(\gamma,\sigma)\ P_X(\gamma,t)\right). \tag{3.21}$$

As the state space of the network is given by the Cartesian product of the state spaces of the different edges, solving the system of ODEs arising from (3.21) quickly becomes infeasible. We therefore either have to look for symmetries or other simplifications to obtain a state space of manageable size (see Section 3.4.2) or consider small networks (see Section 3.4.3). If neither is an option, stochastic simulations, as presented by Griffiths et al. [45] are more suitable to compute a good approximation for the expected flux through the network.

3.4.2 Example: Retention of large particles in 2D and 3D grids

We begin by considering a simple model for the retention of particles with larger diameter than the pores, so that all particles in the fluid are retained on the surface. We assume that a particle landing on an inlet seals it completely. As the particles cannot enter the membrane due to their size, only the edges incident to an inlet can change their conductivity due to particle retention. Hence, the state space of the network can be simplified to $\{\text{sealed}, \text{unsealed}\}^N$, where N denotes the number of inlets, i.e. pores connected to the upper surface (generalising our previous definition for the number of pores in a non-interconnected membrane).

To evaluate the impact of the underlying membrane structure, we consider a simple network as shown in figure 3.4a, where we are interested in the effect of the depth of the network on the decline of the expected flux. Every edge in the network has initially unit dimensionless conductivity. If one of the nodes of the edge is an inlet, the conductivity is reduced to zero once the inlet is sealed.

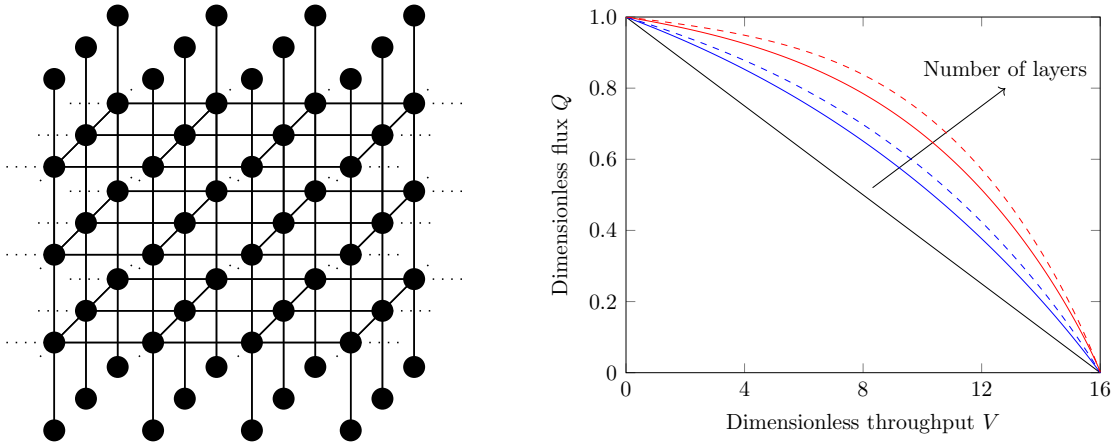

(a) (b)

Figure 3.4: (a) Schematic of a 3×4 3D grid structure with 5 layers. The dotted lines illustrate the cyclic connection. (b) Flux (Q) versus throughput (V) graphs for the 4×4 (dashed) and 16×1 (solid) configuration with 4 (blue) and 8 (red) layers. The black line corresponds to 16 non-interconnected pores. An increase in concavity is observed with an increase in the number of layers, with the concavity for the 3D structure being more pronounced than for the 2D structure with the same number of layers.

While the network of a real interconnected membrane is usually three-dimensional, it is useful to consider a two-dimensional model. We show the difference in the flux–throughput graphs for the 2D and 3D structure by comparing the results for a 4×4 and 16×1 gridstructure, and a membrane containing 16 non-interconnected pores. To provide the most accurate representation of a real membrane, we introduce cyclic connectivity, meaning that the nodes on the right boundary are connected to the ones on the left and the ones on the front boundary to those at the back.

Compared with a membrane with non-interconnected pores, the flux–throughput graph increases in concavity with the number of layers of the membrane (figure 3.4b), a pattern that is commonly observed when filtering BSA with interconnected membranes. Additionally, the concavity of the flux–throughput graphs is more pronounced for the 3D structure than the 2D structure, which we expect to be due to the higher average degree of the vertices in the 3D structure (figure 3.4b).

3.4.3 Internal blocking in a small network

To study the impact of particle size on the flux–throughput shape for different membrane geometries, we now consider a model of a single particle type with the pores having larger diameter than the particles. In this case, initially the particles can

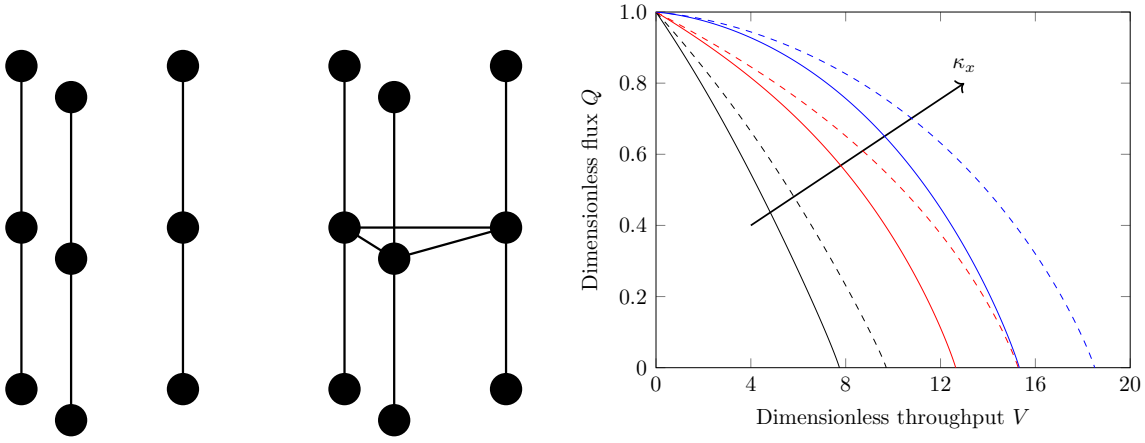

(a) (b)

Figure 3.5: (a) Schematic of non-interconnected (left) and interconnected (right) network structure. (b) Flux (Q) versus throughput (V) graph for $\kappa_x = 0.1, 0.5, 0.9$ for non-interconnected (solid) and interconnected (dashed) network structure. The interconnected network structure leads to a larger expected total throughput than the non-interconnected structure for the chosen retention probabilities.

traverse any edge in the graph. We assume that the dimensionless conductivity of an edge is either $1, \kappa_x$ or 0 depending on whether the edge has retained $0, 1$ or 2 particles respectively, with differences in the value of κ_x identified with differences in the particle size. We consider $\kappa_x = 0.1, 0.5, 0.9$ where a smaller particle size corresponds to a bigger κ_x. As in Section 3.2.3 we choose a retention probability $P_R = 0.1$. Thus, the state space of an edge can be represented by the set $\{0, 1, 2\}$ and the size of the state space is 3^E, where E is the number of edges in the network. We consider the two networks shown in figure 3.5a with 6 and 9 edges for the non-interconnected and interconnected networks respectively. The state space for the interconnected network with 9 edges contains $3^9 = 19683$ elements, which makes computing the expected flux for the interconnected network computationally still feasible. However, considering more than 10^5 states becomes difficult without further optimisation.

Note that for the same values of κ_x, the flux–throughput curve for the interconnected network structure lies above the flux–throughput curve for the non-interconnected structure, and the expected total throughput is significantly higher for the interconnected network structure than for the non-interconnected structure (figure 3.5b). This is an observation that we expect in general when comparing the performance of interconnected and non-interconnected membranes, and is corroborated by the stochastic study performed in [45], as an interconnected membrane structure allows for more load balancing once the pores start to constrict.

3.5 Fast computation of filtration coefficients

We now consider the transport of small contaminants such as bacteria or colloids in a deep porous medium such as a depth filter with interconnected pores. Studying the transport of small contaminants is of particular importance for example when modelling the dispersion of pollutants into groundwater aquifers [85], where the spreading speed and penetration depth of the pollutants are of particular interest. The transport and diffusion of the particles can be modelled using the standard advection–diffusion equation. The standard tool for modelling the adsorption (and potential release) of particles on a macroscale is the *filtration coefficient*, which measures the probability that a particle is retained per unit area. Note that the filtration coefficient λ_r represents an averaged retention probability that depends both on the properties of the particle, for example its radius r, and the microstructure of the porous medium, and can therefore vary spatially and temporarily. Thus, we can compute the concentration c_r of the pollutant in, say, the lower half-space $\Omega = \{(x, y, z) : z \leq 0\}$ by solving

$$\frac{\partial c_r}{\partial t} + \nabla \cdot (\mathbf{U} c_r) = \Delta(D c_r) - \lambda_r c_r \tag{3.22}$$

subject to a source condition $c_r(z = 0, t) = 1$. Here, $\mathbf{U}$ denotes the averaged Darcy velocity and D a diffusion coefficient, which depends on the microstructure and can either be computed using homogenisation theory [30] or continuous-time random-walk theory [15]. If the retention of particles is based on size-exclusion, an experimental way of measuring the filtration coefficient is to measure the concentration difference for a small volume discharge before and after passing through the porous medium for the different particle sizes [34].

Determining filtration coefficients accurately is of high importance for predicting the transport of particles in a porous medium. It has been shown that modelling a porous medium as a network is a suitable tool to determine filtration coefficients [34, 124]. In both publications, the authors determine the penetration depths for different particle sizes based on a large number (10^5) of Monte Carlo simulations per particle size in question. We show that the insights from modelling membranes with interconnected pore structure can be used for a much faster and accurate computation.

For particle retention based on size exclusion, Yuan et al. [124] introduce two capture schemes: the *minimum capture scheme* and the *maximum capture scheme*. The minimum capture scheme replicates the flow-based probabilities from Section 3.4 where the probability $P(f, v)$ of taking an edge f from a given node v is given by the

positive flux of f divided by the sum of all outgoing fluxes, that is

$$P(f,v) = \mathbb{1}_{\Delta p(f)<0} \frac{\kappa(f)\Delta p(f)}{\sum_{u\in C(v)} \mathbb{1}_{\Delta p(e(v,u))<0} \kappa(e(v,u))\Delta p(e(v,u))}, \tag{3.23}$$

where $C(v)$ denotes the neighbours of v and $\Delta p(e(v,u)) = p(v) - p(u)$ is the pressure difference between nodes v and u. To compute filtration coefficients, the effect of clogging is neglected, which is why the pressure and the conductivity are independent of any given state.

For the maximum capture scheme, the particle will only travel through edges with positive flux that have the same or a larger radius, if no such edge exists at a given node v, the particle is retained. In this instance, the probability of taking a given edge f at a node v can be computed in a similar fashion to (3.23), except that the indicator function is now for the set of edges that have a positive (outgoing) flux and a larger radius than the particle.

Because we are considering a hydraulic system without cycles and there is no flow between nodes of equal pressure, we can obtain a topological ordering of the nodes based on their pressure. Therefore, we can compute the probability $P_r(v)$ for a particle to reach a node v by solving the forward probability equation

$$P_r(v) = \sum_{u\in C(v)} P(e(u,v),u) P_r(u) \tag{3.24}$$

following the topological ordering of the nodes and subject to flux-based initial conditions for the nodes at the surface. Solving the forward equation needs $O(|V|)$ steps, where V is the set of nodes and is therefore significantly faster than conducting Monte Carlo simulations.

3.6 The continuum limit

When considering filtration experiments where the ratio of the typical particle diameter to the typical pore diameter is very small or there is a large number of different potential particle sizes involved, it can be preferable to treat the distribution of the random variable in question, be it the amount of mass in a given volume of fluid or particle size, as continuous. The random variable $X(t)$ measuring the state of a given pore then takes on values in $\mathbb{R}^N$, where $N \in \mathbb{N} \cup \{\infty\}$. For continuous random variables, we are no longer interested in computing the probability $P(X = \sigma)$ of a

pore being in state $\sigma \in \mathbb{R}^N$, as this will be 0 for any continuous distribution. We are interested in the probability density $p(X,t)$ instead, which satisfies

$$\int_{\mathbb{R}^N} p(x,t)\ \mathrm{d}x = 1 \quad \forall\ t > 0. \tag{3.25}$$

In Section 3.6.1 we discuss how to model continuous particle-size distributions, in Section 3.6.2 we discuss how to model equally sized but infinitesimally small particles.

3.6.1 Continuous particle-size distributions

When modelling the continuous particle-size distributions, we assume that in any given amount of fluid V there are countably many particles whose positive mass distribution is given by a continuous distribution ρ. We note that it is possible to consider other features such as the diameter of a particle as well and consequently employ continuous distributions $\tilde{\rho} : \mathbb{R}^N \to \mathbb{R}$, where N denotes the number of features. As the corresponding models differ only marginally in notation, we will consider the simple model with the mass as the single feature for brevity, as for example discussed by Shapiro et al. [105]. We can extend the equation (3.4) for a single-particle model to continuous models to obtain the governing equation for the probability density $p(x,t)$ of a pore to have mass x at time t as

$$\begin{aligned}\frac{\partial p(x,t)}{\partial t} = &-\kappa(x)p(x,t)\int_0^\infty P_R(x,y)\rho(y)\ \mathrm{d}y \\ &+\int_0^x \kappa(y)p(y,t)P_R(y,x-y)\rho(x-y)\ \mathrm{d}y,\end{aligned} \tag{3.26}$$

where $P_R(x,y)$ denotes the retention probability for a particle of mass y to stick in a pore that has retained particles with total mass x. Assuming that, initially, there are no particles in the pore, we use the initial condition $p(x,0) = \delta(x)$ where δ is the *Dirac delta function*.

Note that, in this model, the ordering of the particles does not play a role but only the mass of the particles that have been filtered out. As discussed in Section 3.3, we can let κ act on ordered sequences of real numbers instead, that is,

$$\kappa : \mathbb{R}^{\mathbb{N}} \to [0,1]. \tag{3.27}$$

If we denote the density of particles leading to a transition from state σ to state τ by $\rho(\sigma,\tau)$ and the corresponding retention probability by $P_R(\sigma,\tau)$, we obtain an integral

version of (3.18) for the probability density $p(\sigma, t)$ of a pore to be in state σ at time t as

$$\begin{aligned}\frac{\mathrm{d}p(\sigma,t)}{\mathrm{d}t} = &-\left(\int_{\{\tau:\sigma\to\tau\}} \rho(\sigma,\tau)\ P_R(\sigma,\tau)\ \mathrm{d}\tau\right)\kappa(\sigma)\ p(\sigma,t)\\ &+\left(\int_{\{\gamma:\gamma\to\sigma\}} \rho(\gamma,\sigma)\ P_R(\gamma,\sigma)\ \kappa(\gamma)\ p(\gamma,t)\ \mathrm{d}\sigma\right),\end{aligned} \tag{3.28}$$

subject to the standard initial condition $p(\sigma, 0) = \delta(\sigma)$ for all $\sigma \in \mathbb{R}^{\mathbb{N}}$. While this approach allows us to handle continuous distributions theoretically, we will always have to resort to some discretisation for numerical evaluations, hence considering continuum distributions of particle features such as their radius is only of limited value.

3.6.2 Infinitesimally small particles

We now turn our attention to the experiments where the ratio of the particle diameter to the pore diameter is very small. We will use the *central limit theorem* to show that, as the ratio of particle diameter to pore diameter converges to zero, the number of particles (and consequently their combined mass as well) in a given volume of fluid is normally distributed under an appropriate scaling. We will then show that, in the limit of infinitesimally small particles, the total mass of the particles in the given volume of fluid equals the expected value of the distribution with probability 1. From this we can infer that, for infinitesimally small particles, the filtration process is a deterministic process and so the conductivity function is equal to the flux–throughput relationship. Using the result that the combined mass of all particles for a very (but not infinitesimally) small ratio of particle diameter to pore diameter is normally distributed, we will show that the probability density for the total mass in a pore satisfies a version of the *Fokker–Planck* equation with small diffusivity. We will conclude the section by exploiting the smallness of the diffusivity to construct approximate analytical solutions to the Fokker–Planck equation, which we will compare with the corresponding full numerical solution and the results of the discrete model 3.4 of the previous sections.

From our discrete model, we know that the number of particles in a given volume of fluid V is Poisson-distributed with parameter cV, where c denotes the concentration of particles. If we divided each particle into $K > 1$ equally sized smaller particles, the random variable S_K counting the number of particles would be Poisson-distributed

with parameter KcV and so its expected value is $\mathbb{E}[S_K] = KcV$ and its variance is $\mathbb{V}[S_k] = KcV$ as well. The central limit theorem [70] then states that

$$\frac{S_K - KcV}{\sqrt{KcV}} \to \mathcal{N}(0,1), \tag{3.29}$$

weakly as $K \to \infty$, where $\mathcal{N}(\mu, \sigma^2)$ denotes the normal distribution with expected value μ and variance σ^2. Therefore, for large K, we can infer that the total mass $M_K = \frac{1}{K\rho_K} S_K$ is distributed as

$$M_N \sim \mathcal{N}\left(\tilde{c}V, \sqrt{\frac{\tilde{c}V}{N}}\right), \tag{3.30}$$

where $\tilde{c} = c/\rho_K$ is the mass per unit volume. This implies that, in the limit $K \to \infty$ of infinitesimally small particles, the total mass in a volume V of fluid is $\tilde{c}V$ with probability 1. Therefore, if our random variable $X(t)$ tracks the mass received by a pore, we obtain the deterministic growth equation

$$\frac{\mathrm{d}X}{\mathrm{d}t} = \kappa(X(t)). \tag{3.31}$$

Then, for the probability density $p(m,t)$ of a pore having mass m at time t, we can employ Reynolds transport theorem to obtain the transport equation

$$\frac{\partial p}{\partial t} + \frac{\partial}{\partial m}(\kappa p) = 0, \tag{3.32}$$

subject to the initial condition $p(m,0) = \delta(m)$, which we can solve using the method of characteristics as follows, provided $\kappa > 0$ and κ is differentiable: let $m(t)$ satisfy $\mathrm{d}m/\mathrm{d}t = \kappa(m(t))$ subject to the initial condition $m(0) = m_0$. For the inverse problem of finding m_0 given (m,t), $t \geq 0$, we compute the inverse mapping $M^{-1}(m,t)$ that maps $m(t)$ to m_0 by solving the backward equation $\mathrm{d}m/\mathrm{d}t = -\kappa(m(t))$. Note that, because of our requirement $\kappa > 0$, the inverse problem is well-defined. The solution to (3.32) is therefore given by

$$p(m,t) = p(M^{-1}(m,t)) \exp\left(-\int_0^t \kappa'(m(s))\ \mathrm{d}s\right). \tag{3.33}$$

For the special case of the initial condition $p(x,0) = \delta(x)$, we can compute the flux $Q(t)$ as

$$\begin{aligned} Q(t) &= \int_0^\infty p(m,t)\kappa(m)\ \mathrm{d}m \\ &= \exp\left(-\int_0^t \kappa'(m(s))\ \mathrm{d}s\right) \int_0^\infty \delta(M^{-1}(m,t))\kappa(m)\ \mathrm{d}m. \end{aligned} \tag{3.34}$$

For the coordinate transform $z = M^{-1}(m,t)$, we note that we can compute the determinant of the Jacobian of the coordinate transform as follows: introduce

$$v(m,t) = \frac{\partial M^{-1}(m,t)}{\partial m} \tag{3.35}$$

and note that $v(m,0) = 1$. Then, we have

$$\begin{aligned} \frac{\partial v}{\partial t} = \frac{\partial^2 M^{-1}(m,t)}{\partial t\, \partial m} &= -\frac{\partial \kappa(M^{-1}(m,t))}{\partial m} \\ &= \frac{\partial \kappa(M^{-1}(m,t))}{\partial M^{-1}(m,t)} \frac{\partial M^{-1}(m,t)}{\partial m} = -\kappa'(m(t))v(m,t) \end{aligned} \tag{3.36}$$

which exhibits the solution

$$\frac{\mathrm{d}M^{-1}}{\mathrm{d}m} = \exp\left(-\int_0^t \kappa'(m(s))\ \mathrm{d}s\right) \tag{3.37}$$

so that we obtain the solution to (3.34) as $Q(t) = \kappa(m(t))$. Furthermore, we can then compute the volume as

$$V(t) = \int_0^t \kappa(m(s))\ \mathrm{d}s = \int_0^t \kappa(m(s)) \frac{\mathrm{d}t}{\mathrm{d}m} \mathrm{d}m = \int_0^{m(t)} \mathrm{d}m = m(t) \tag{3.38}$$

and so we arrive at $Q = \kappa(V)$, which means that the conductivity function and the flux–throughput relation are the same. This stands in stark contrast to the results we obtained for non-infinitesimally small particles. The explanation for this difference is that there is currently no randomness in the model.

We visualise the result of the conductivity function and the flux–throughput relation being equal in the limit of infinitesimally small particles in figure 3.6. We show how increasing the number of interpolation points leads to a convergence to the conductivity function by solving the volume-dependent evolution equation (3.5) for an increasing number of interpolation points. The example of the step function, figure 3.6a, demonstrates that even discontinuous functions are being approximated well, while the periodic sin function, figure 3.6b, demonstrates that even for a large number of interpolation points, we will observe a difference between the conductivity function and the flux–throughput relation eventually. Note that this serves as a reminder that finite-size effects do play a role in membrane filtration.

In order to introduce randomness, we revisit the assumption that the particles are infinitesimally small and their mass in a given volume V of fluid is $\tilde{c}V$ with probability 1. Instead, we look at the derivation for the distribution of mass (3.30) which states

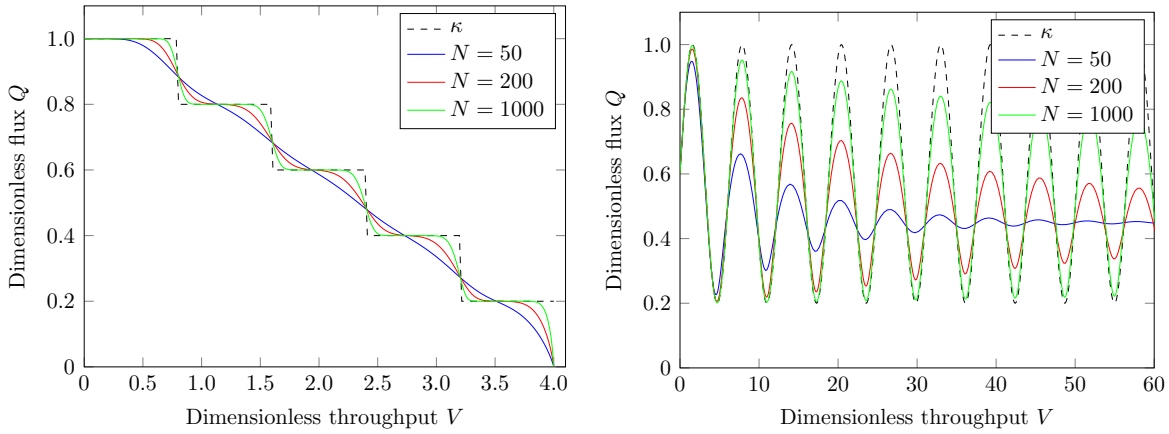

(a) (b)

Figure 3.6: Results for solving the evolution equations (3.5) for different number of interpolation points. (a) Step function $f(x) = 1 - n/5$ for $x \in [4n/5, 4(n+1)/5)$ and $n \in \{0, \dots 4\}$. The N interpolation points are equidistributed across the interval $[0, 4]$. (b) $f(x) = \frac{2}{5}(\frac{3}{2} + \sin(x))$ with the number of interpolation points referring to the interval $[0,\ 2\pi]$.

that if the particles are very small (but not infinitesimally small), the amount of mass $m(V)$ in a given volume of fluid is distributed as

$$m(V) \sim \tilde{c}V + \epsilon\mathcal{N}(0, V), \tag{3.39}$$

where $\epsilon^2 = \tilde{c}/N$ expresses the amount of mass per particle and N is the number of particles. Then, the mass $m(t)$ of a pore at time t follows a random process, formally written as

$$m(t + \Delta t) = m(t) + \kappa(m(t))\Delta t + \epsilon\sqrt{\kappa(m(t))}\mathrm{d}W, \tag{3.40}$$

as the increase in mass is governed by the constant amount $\kappa(m(t))\Delta t$ with some added Gaussian noise; W denotes a standard Brownian motion. Then, following the derivation of the Fokker–Planck equation [107] we infer that the probability density $p(m, t)$ for a pore to have mass m at time t has to satisfy the Fokker–Planck equation

$$\frac{\partial p}{\partial t} + \frac{\partial}{\partial m}(\kappa p) = \epsilon^2 \frac{\partial^2}{\partial m^2}\left(\frac{\kappa p}{2}\right), \tag{3.41}$$

subject to the initial condition $p(m, 0) = \delta(m)$. In comparison to the transport equation (3.32), the Fokker–Planck equation (3.41) contains a small diffusive term to account for the randomness. We can solve this equation numerically with the method of lines by discretising over m using centered differences. Moreover, we can also use the smallness of ϵ to make further analytical progress. We introduce the coordinate

transform

$$\epsilon\eta = m - y(t), \tag{3.42}$$

so that η is $O(1)$ and y is defined as the solution to the ODE

$$\frac{\mathrm{d}y}{\mathrm{d}t} = \kappa(y(t)), \tag{3.43}$$

subject to the initial condition $y(0) = 0$. This yields

$$\frac{\partial p(\eta,t)}{\partial t} - \frac{1}{\epsilon}\frac{\partial y}{\partial t}\frac{\partial p(\eta,t)}{\partial \eta} + \frac{\mathrm{d}\kappa}{\mathrm{d}m}p(\eta,t) + \frac{1}{\epsilon}\frac{\partial p(\eta,t)}{\partial \eta}\kappa(m) = \frac{\partial^2}{\partial \eta^2}\left(\frac{p(\eta,t)\kappa(y(t)+\epsilon\eta)}{2}\right),$$

subject to the scaled initial condition $p(\eta,0) = \frac{1}{\epsilon}\delta(\eta)$ and we use the expansion $\kappa(y(t)+\epsilon\eta) \sim \kappa(y(t)) + \epsilon\eta\frac{\mathrm{d}\kappa}{\mathrm{d}m} + O(\epsilon^2)$ to obtain the highest order term

$$\frac{\partial p(\eta,t)}{\partial t} + \frac{\mathrm{d}\kappa(y(t))}{\mathrm{d}m}\frac{\partial(\eta p(\eta,t))}{\partial \eta} = \frac{1}{2}\frac{\partial^2}{\partial \eta^2}\left(p(\eta,t)\kappa(y(t))\right), \tag{3.44}$$

subject to the initial condition $p(\eta,0) = \delta(\eta)$. Note both κ and κ' only depend on t and not on η, which will allow us to pursue an ODE solution. For typical conductivity functions, we expect $\kappa > 0$ and $\kappa' < 0$. Then, (3.44) exhibits a *quasi-stationary distribution* subject to the normalisation condition

$$\int_{-\infty}^{\infty} p(\eta,t)\ \mathrm{d}\eta = 1 \tag{3.45}$$

as

$$p(\eta,t) = \left(\pi\left|\frac{\kappa(y(t))}{\kappa'(y(t))}\right|\right)^{-1/2}\exp\left(\frac{\kappa'(y(t))}{\kappa(y(t))}\eta^2\right). \tag{3.46}$$

Note that the quasi-stationary distribution only exists if the ratio κ'/κ is negative. We can use this result to compute an approximation to the expected flux as

$$Q(t) = \int_{-\infty}^{\infty}\kappa(m)\left(\pi\epsilon^2\left|\frac{\kappa(y(t))}{\kappa'(y(t))}\right|\right)^{-1/2}\exp\left(\frac{\kappa'(y(t))}{\kappa(y(t))}\frac{(m-y(t))^2}{\epsilon^2}\right)\ \mathrm{d}m, \tag{3.47}$$

and we will use $Q(t) = 0$ whenever $\kappa'/\kappa \geq 0$. We plot the comparison for the conductivity function $\kappa(m) = 1/(1+m^4)$ in figure 3.7. This form of κ is chosen for its similarity to the conductivity function of Section 3.2. Note that for κ'/κ close to zero, the distribution is relatively wide and so the quasistatic approximation differs significantly from the exact solution of the time-dependent discrete model (3.4) . We plot the flux versus time dependence as the error at early time would skew the flux versus volumetric throughput comparison. Finally, note that for small ϵ, we expect the distribution to have small variance and so we integrate using logarithmically

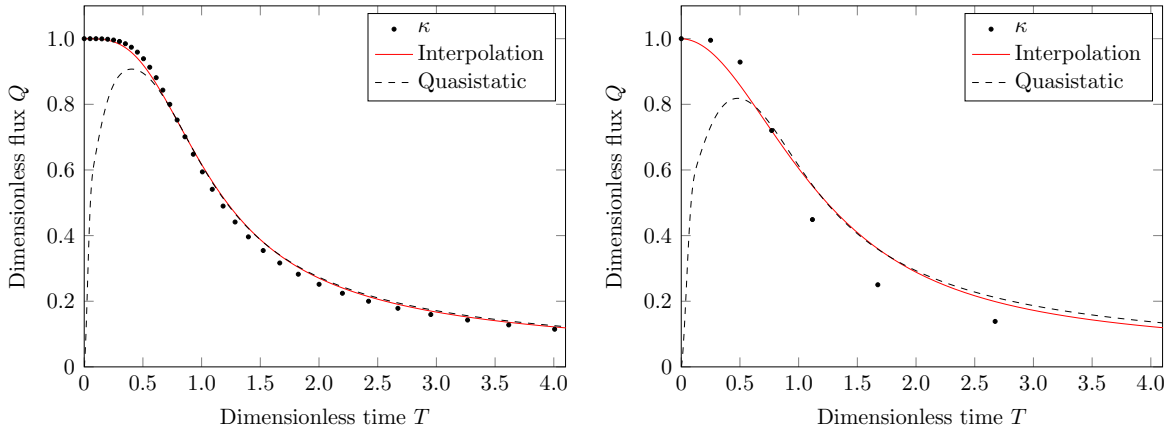

(a) (b)

Figure 3.7: Time dependent flux from the general evolution equation (3.4) compared with the approximation obtained by the quasistatic solution (3.47). We show figures for $\epsilon = 0.05$ (a) and $\epsilon = 0.15$ (b).

spaced points around the expected value using an interval length of five times the standard deviation to obtain an approximation of high accuracy.

To obtain a general solution to (3.44) we use the ansatz

$$p(\eta, t) = \sqrt{\frac{B(t)}{\pi}} \exp(-B(t)\eta^2) \tag{3.48}$$

where B is a positive function and the prefactor $\sqrt{B(t)/\pi}$ is chosen to satisfy the normalisation condition (3.45). Note that under this assumption, we have

$$-\kappa' \sqrt{\frac{B(t)}{\pi}} \eta \exp(-B(t)\eta^2) - \eta\kappa \sqrt{\frac{B(t)}{\pi}} B(t) \exp(-B(t)\eta^2) \to 0 \text{ for } |\eta| \to \infty \tag{3.49}$$

and so mass is conserved. Using (3.48) in (3.44) and simplifying, we obtain

$$B' - 2BB'\eta^2 + 2\kappa' B - 4\kappa'\eta^2 B^2 = -2\kappa B^2 + 2\kappa\eta^2 B^3. \tag{3.50}$$

The variables t and η are independent of each other, and so B has to satisfy the ODE

$$B' + 2\kappa' B = -2\kappa B^2. \tag{3.51}$$

The equation (3.51) is a Bernoulli equation [64] and can be turned into a linear equation using the ansatz $B = 1/z$, $B' = -z'/z^2$, and the change of variable $\mathrm{d}y/\mathrm{d}t = \kappa$ so that, by multiplying through with $1/\kappa^3$, we obtain the ODE

$$\frac{\mathrm{d}}{\mathrm{d}y}\left(\frac{z}{\kappa^2}\right) = \frac{2}{\kappa^2} \tag{3.52}$$

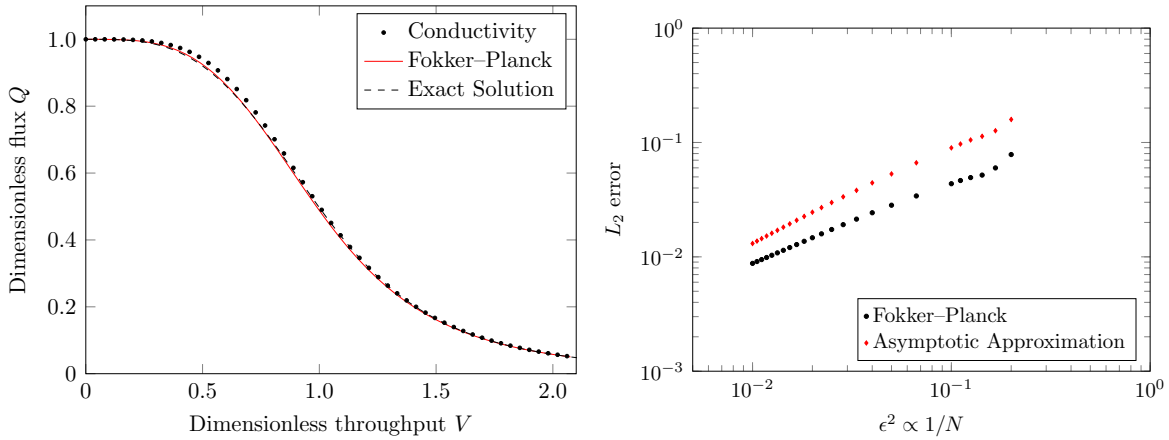

(a) (b)

Figure 3.8: (a) Comparison between the conductivity function, the exact solution of the discrete model (3.5), and the numerical solution to the Fokker–Planck equation (3.41) for $N = 100$ interpolation points. (b) L_2 error between the exact solution of the discrete model (3.5) and the Fokker–Planck equation (3.41) (black) and the exact solution and the asymptotic solution (3.57) (red).

which exhibits the solution

$$B(t) = \left(2\kappa(y(t))^2 \int_0^{y(t)} \frac{1}{\kappa^2(s)} \, \mathrm{d}s \right)^{-1}. \tag{3.53}$$

Now, in order to compute the flux $Q(t)$, we have to evaluate the integral

$$Q(t) = \int_{-\infty}^{\infty} \sqrt{\frac{B(t)}{\pi}} \exp(-B(t)\eta^2)\kappa(y(t) + \epsilon\eta) \, \mathrm{d}\eta \tag{3.54}$$

and we can expand in terms of κ so that we obtain

$$Q(t) = \int_{-\infty}^{\infty} \sqrt{\frac{B(t)}{\pi}} \exp(-B(t)\eta^2) \left(\kappa(y(t)) + \epsilon\eta \frac{\mathrm{d}\kappa}{\mathrm{d}m}(y(t)) + \frac{(\epsilon\eta)^2}{2} \frac{\mathrm{d}^2\kappa}{\mathrm{d}m^2} y(t) + \dots \right) \mathrm{d}\eta \tag{3.55}$$

and we see that the first term is simply $\kappa(y(t))$ due to normalisation and the second one is odd and will therefore vanish in the integral. We can evaluate the $O(\epsilon^2)$ integral by noting that

$$\int_{-\infty}^{\infty} \sqrt{\frac{B(t)}{\pi}} \frac{\eta^2}{2} \exp(-B(t)\eta^2) \, \mathrm{d}\eta = \frac{1}{2\sqrt{\pi}B(t)} \int_{-\infty}^{\infty} s^2 \exp(-s^2) \, \mathrm{d}s = \frac{1}{2B(t)} \tag{3.56}$$

and so we obtain

$$Q(t) = \kappa(y(t)) + \epsilon^2 \frac{\mathrm{d}^2\kappa}{\mathrm{d}m^2}(y(t)) \frac{1}{2B(t)} + O(\epsilon^3) \tag{3.57}$$

as well as

$$V(t) = y(t) + \int_0^t \left(\epsilon^2 \frac{\mathrm{d}^2\kappa}{\mathrm{d}m^2}(y(s)) \frac{1}{2B(s)} \right) \mathrm{d}s. \tag{3.58}$$

The comparison between the solution to the Fokker–Planck equation (3.41) and the solution to the volume dependent evolution equation for the discrete model, (3.5), is shown in figure 3.8. We obtain good agreement between the continuum and the discrete model, as well as between the numerical solution to the Fokker–Planck equation (3.41) and the asymptotic expansion (3.57). This shows that we can use continuum models as an alternative to the discrete model once we have a large number of interpolation points.

3.7 Conclusion

In this chapter, we showed how to compute the expected flux through a membrane during a filtration experiment on the basis of a *conductivity function*, which relates the number and order of the retained particles in a pore to the flux through it. The expected flux through the membrane can then be computed by solving a system of ODEs for the probability distribution of the state of a given pore. Describing membrane filtration in terms of a conductivity function opens up the possibility of considering a variety of retention mechanisms in filtration models, as the stochastic model is valid for any given non-negative conductivity function. We showed that this approach can be applied to a range of membrane-type to feed-type combinations by discussing its application to multi-particle feeds, multi-pore-type membranes, and membranes with an interconnected pore structure. Furthermore, for typical applications, the size of the state space is such that the computation of the expected flux is orders of magnitude faster and more precise than using a stochastic simulation. The ideas behind our model can also be used to speed up the computation of related problems such as determining filtration coefficients. Finally, the derivation of the ODEs highlights that membrane filtration fundamentally is a stochastic process and the ODE model allowed us to compute the probability distribution of the potential states of a pore. We showed that in the limit of small particle to pore diameter, the exact model agrees with the Fokker–Planck equations arising from a continuum approach. This result is of great relevance to the question of whether we can find the conductivity function for a given flux–throughput relation: Backward-diffusion is an ill-posed problem [94], and so we cannot hope to solve the inverse problem of finding the conductivity function without any regularisation. Alternatively, we have to measure a different relation than the flux–throughput relation. The next chapter

will use some of the models introduced in this chapter and tackle the inverse problem of finding the conductivity function, albeit from the spreading speed of a gravity current.

Our model is based on the assumption that one particle enters a pore or interconnected pore structure at a time and so we can define a conductivity function relating the number of retained particles to the flux through the pore. For high enough particle concentrations, several particles can be expected to traverse a pore at the same time and so the assumptions underlying our derivations are no longer valid, making our method not applicable for these instances. When dealing with general multi-particle models or intricate geometries, additional considerations or assumptions have to be made to reduce the size of the state spaces for the corresponding system of ODEs, otherwise the method becomes already impractical for modest instances. If these reductions in the state space are not possible, computing an approximation for the expected flux should be considered instead.

In the realm of interconnected membranes, future work can include deterministic–stochastic models, where we combine our continuum and discrete models. This approach would allow us to consider, for example, feeds containing several particle types through interconnected membranes. Based on the ansatz of modelling fouling as a stochastic process, it would furthermore be important to find ways of computing the probability density for the measured flux. These insights could be of significant value in the area of microfluidic filtration, where the small number of particles and pores often shows the stochastic nature of the filtration process.

Chapter 4

Inferring filtration laws by observing the spreading of a gravity current on a membrane

4.1 Motivation and overview of the chapter

A common feature of Chapters 2 and 3 is that the filtration laws in question are treated as *forward problems*: In Chapter 2, we presented evidence of improvement to the conventional caking law by accounting for the compression of the filtercake, while assuming that all parameters are known. This allows us to predict, say, the decline in flux in a constant-pressure-filtration experiment if we know the relevant parameters. Similarly, in Chapter 3 we presented a general theory to model filtration based on stochastic considerations. One of the key ingredients, the conductivity function, however, was either assumed to be known or had to be inferred using numerical or experimental techniques. This chapter introduces a different approach for the *inverse problem*, the process of finding the filtration law from experimental measurements.

The standard procedure in chemical engineering for determining the filtration law for a given dead-end filtration task is to measure either the decline in flux under a constant applied pressure or the increase in differential pressure for a constant applied flux [6]. These two methods are equivalent under the conventional filtration model, and so the filtration law can be determined by finding a best fit. While this approach is straightforward, there exist situations where the necessary setup cannot be realised, for example when looking at clogging in a geophysical setting such as calcite precipitation, which is hard to replicate in the laboratory [69]. In these instances, other measurement techniques have to be used.

To motivate the approach presented in this chapter, consider a continuously fed

gravity current carrying neutrally buoyant particles that is spreading into air on a porous medium. *Gravity current* is a term commonly used to describe the predominantly horizontal propagation of a fluid into another fluid of different density, as the horizontal velocities will be much larger than the vertical velocities. Nevertheless, as the underlying medium is porous, the gravity current will start leaking into it, which will also make the particles in the current migrate into the medium. If we assume that the particles clog the medium, the drainage at a given position will continuously decrease, allowing the gravity current to spread differently than it would if it had not carried any particles. The filtration law describing the clogging process will be the same at all points in the medium, although the clogging happens asynchronously, as the height of the fluid is not uniform. Now assume we continuously measure the radial extension. Can we infer the filtration law?

This chapter looks at the problem of determining the filtration law based on the spreading of a gravity current from a practical and a theoretical angle. In the first section, we couple the well-known theory of gravity currents with our theory from Chapter 3 to model experiments conducted by Box [22]. In his experiments, Dr. Box tracked the position of the front of an axisymmetric particle-laden gravity current spreading on a porous mesh. While we know the relevant experimental parameters, such as the inflow rate, the viscosity of the liquid, or the concentration of particles within the fluid, we do not know the conductivity function describing the reduction of permeability due to the particles being deposited on the mesh. We determine the conductivity function by using the theory for *discrete filtration laws* developed in Chapter 3.

In the second section, we look at an inverse problem for *continuous filtration laws*. We generalise the conventional four filtration laws to allow for a continuous family of filtration laws and then show that these filtration laws can in fact be inferred from the spreading speed of a two-dimensional gravity current, provided the experimentalist has control over the influx which originates from a single point source.

Both sections will provide a separate overview of the relevant literature as well as indications about which parts of the chapter constitute original work.

4.2 Inferring discrete filtration laws from the axisymmetric spreading of particle-laden gravity current on a mesh

The theory of gravity currents is applicable to a wide range of fluid problems encountered in industry and the environment, making it an active area of research. Initially studied to predict the spreading of poisonous gas released from a point source [62], many variations on gravity currents are encountered and studied in a plethora of atmospheric and geological fluids [108]. As a more recent application, gravity currents have been studied to understand and improve subsurface CO_2 storage [63].

In the simplest setting, the outward spreading of a liquid into another liquid of lower density on an impermeable surface is studied, both in a $2D$ and axisymmetric configuration [61], although the theory also applies for inward facing settings [43, 126]. For impermeable bases, other configurations such as inclines [120] motivated by CO_2 storage and elastic membranes [125] have also been studied. Motivated by subsurface problems, the spreading within a confined area, be it in 2D [95] or axisymmetric [47] have been studied.

When studying the spreading of gravity currents on soil, for example motivated by the spillage of some chemicals, or within the porous mantle of the earth, drainage cannot be neglected. The drainage can either stem from the entire base being porous [2] or from point leaks [121] or line leaks [90], which is particularly relevant when assessing the long-term viability and capacity of CO_2 storage sites. For gravity currents spreading on a porous base on top of an infinite reservoir, a distinguishing feature is whether the medium is *deep*, that is, never fully saturated [112] or *thin*, where it is fully saturated after a certain time [97]. In both instances, the gravity current attains a finite spreading radius when subject to a constant influx. This is not the case when the porous base is not prewetted and capillary effects play a role [82], in which case a non-wetting nose can spread arbitrarily far under constant influx [104].

A special case of gravity currents are particle-laden gravity currents, which can be encountered in oceanic sediment transporting currents, volcanic ash or simple saltwater currents [58]. When the particles are not neutrally buoyant, the study of particle distribution within turbulent gravity currents, or *turbidity currents*, is especially of interest [20]. In these currents, particle settling occurs in a viscous boundary layer.

In this section, we study the axisymmetric spreading of a particle-laden, viscous gravity current into air on a prewetted porous mesh under constant influx. As the

particles are neutrally buoyant, they will not sediment and only settle due to vertical flows; however, they will be retained by the mesh as we consider particles whose diameter is larger than the aperture. The retention of particles on the mesh or on top of each other leads to a reduction in permeability of the mesh, reducing the outflow and allowing the gravity current to spread further. As the reduction of permeability happens in *quantised* steps, we can employ the theory developed in Chapter 3 to model the averaged reduction in permeability. In Section 4.2.1, we combine this theory with the standard theory of gravity currents to develop a novel model to explain the experimental observations and nondimensionalise the model. An important aspect of the dimensionless model is the dimensionless parameter δ, the ratio of the height scale to the thickness of the mesh. In Section 4.2.2, we study the finite spreading radius of a gravity current for the cases where $\delta \to 0$, that is, the mesh is infinitesimally thin, and $\delta \to \infty$, that is, the mesh is infinitely deep. In the latter case, we recover the solution of Spannuth et al. [112], whereas the first case constitutes a problem mentioned in [97] whose solution, to our best knowledge, has not yet been published. Additionally, we consider the more general problem of finding the spreading radius for $\delta \in (0, \infty)$ and show how the limit solutions of $\delta \to 0$ and $\delta \to \infty$ act as asymptotic limits. In Section 4.2.3, we develop a fixed-interval finite difference scheme to numerically solve our novel mathematical model. In Section 4.2.4, we describe the experiments conducted by Dr. Finn Box [22], in the following Section 4.2.5, we show how we can employ a parameter sweep to determine the conductivity function and compare the experimental results with our theoretical predictions.

4.2.1 Mathematical model

We want to model the axisymmetric spreading of a fluid containing neutrally buoyant particles into air on a prewetted, thin porous membrane under constant influx. The spreading radii measured for different concentrations of the particles are shown in figure 4.1. Thus, we can expect the typical spreading radius $\bar{r}_f$ to be on the order of tens of centimetres, and the Bond number Bo

$$Bo := \frac{\Delta\rho g \bar{r}_f^2}{\gamma} \gg 1 \tag{4.1}$$

will be large. Here, $\Delta\rho$ denotes the difference in density between the liquid and the surrounding air, g the gravitational acceleration, and γ the surface tension of the liquid. Therefore, we can neglect the effects of surface tension on the air-liquid surface. Furthermore, as the membrane is prewetted, we can also neglect capillary

entry pressures. If the membrane were not prewetted, we would observe the existence of an imbibition front [104]. Using the standard assumptions of a stress-free surface and a no-slip condition at the interface between the mesh and the base of the current, we can follow the usual steps [61] to obtain the vertically averaged velocity u,

$$u(r,t) = -\frac{\Delta\rho g}{3\mu} h^2 \frac{\partial h}{\partial r}, \tag{4.2}$$

where μ denotes the dynamic viscosity of the liquid particle mixture and h the height of the gravity current. The viscosity of the mixture will differ from the viscosity μ_0 of the liquid. As we only have data on μ_0, we need to estimate μ. For the experiments in question, the volume concentration of the particles is small, and so we can use the Einstein viscosity [46]

$$\mu = \mu_0 \left[1 + \frac{5}{2}\phi + O(\phi^2)\right], \tag{4.3}$$

where ϕ is the constant particle volume fraction, to estimate the viscosity of the mixture. To compute the drainage, we assume that the pressure of the air is constant and the underside of the mesh is also at atmospheric pressure. We note that the radial length scale is much larger than the horizontal length scale, and so the pressure within the current is hydrostatic to first order. For our experiments, we cannot neglect the depth of the membrane in comparison to the height of the current, hence, we model the drainage velocity v as

$$v(r,t) = \frac{\Delta\rho g k}{\mu}\left(1 + \frac{h}{d}\right) \cdot \mathbb{1}_{h(r)>0}, \tag{4.4}$$

where k denotes the effective permeability of the membrane and d the depth of the membrane. Here, we are neglecting effects of instabilities forming under the mesh on the drainage velocity [96]. Using the continuity equation

$$\frac{\partial h}{\partial t} + \frac{1}{r}(rhu) = -v, \tag{4.5}$$

we arrive at the thin-film equation with drainage

$$\frac{\partial h}{\partial t} = \frac{\Delta\rho g}{3\mu}\frac{1}{r}\frac{\partial}{\partial r}\left(rh^3\frac{\partial h}{\partial r}\right) - \frac{\Delta\rho g k}{\mu}\left(1 + \frac{h}{d}\right). \tag{4.6}$$

For a constant influx Q, conservation of mass is given by

$$2\pi\int_0^{r_f(t)} rh \, \mathrm{d}r + 2\pi\int_0^t\int_0^{r_f(s)} rv \, \mathrm{d}s \, \mathrm{d}r = Qt, \tag{4.7}$$

where $r_f(t)$ denotes the radius of the front where we have $h(r_f, t) = 0$. Differentiating (4.7) w.r.t. t and using (4.6), we obtain the constant influx condition

$$\lim_{r\to 0} rh^3 \frac{\partial h}{\partial r} = -\frac{3\mu Q}{2\pi\Delta\rho g}, \tag{4.8}$$

and the condition for no flux through the nose,

$$\frac{2\pi\Delta\rho g}{3\mu} rh^3 \frac{\partial h}{\partial r}\bigg|_{(r_f,t)} = 0. \tag{4.9}$$

Given that the particles cannot pass the membrane, we also have to account for the change in permeability due to particles retained at the surface blocking up the holes of the mesh. We therefore rewrite the permeability k as

$$k(r, t) = \lambda(r, t)k_d, \tag{4.10}$$

where $\lambda(r, t) \in [0, 1]$ is the dimensionless factor accounting for the reduction in permeability due to the retained particles and k_d denotes the initial effective permeability of the mesh, the product of the permeability and the porosity of the mesh. The particles have a uniform, positive radius, and so, following the argumentation in Chapter 3, we have to account for random effects. For a given radius, we can expect these random effects to average out along the corresponding perimeter, and so we can homogenise the stochastic nature of the clogging with the theory developed in Chapter 3. Thus, if the value of the permeability factor λ is $\lambda_0 = 1$ if zero particles are retained, λ_1 if one is retained, λ_2 if two are retained and so forth, we obtain the homogenised version

$$\lambda(r, t) = \sum_{n=0}^{\infty} \lambda_n P_n(r, t), \tag{4.11}$$

where $P_n(r, t)$ denotes the probability that n particles have been retained at r. The probability P_n can be determined by solving the system of ODEs

$$\frac{\mathrm{d}P_0}{\mathrm{d}t} = -c\lambda_0 P_0 \frac{\Delta\rho g k_d}{\mu}\left(1 + \frac{h}{d}\right) \tag{4.12a}$$

$$\frac{\mathrm{d}P_n}{\mathrm{d}t} = c\left(-\lambda_k P_n + \lambda_{k-1} P_{n-1}\right)\frac{\Delta\rho g k_d}{\mu}\left(1 + \frac{h}{d}\right) \quad n \geq 1, \tag{4.12b}$$

subject to the initial conditions $P_0(x, 0) = 1$ and $P_n(x, 0) = 0$ for $n \geq 1$. The factor c counts the number of particles per unit hydrostatic height, a good approximation for c is given ϕ/d_p, where d_p is the diameter of the particles. While this model is valid for any $\lambda_k \in \mathbb{R}$, we expect $1 = \lambda_0 \geq \lambda_1 \geq \ldots \geq 0$ as the permeability should decrease with increased number of particles but always remain non-negative. The inverse problem of determining the filtration law thus consists of determining $\lambda_k,\ k \geq 1$.

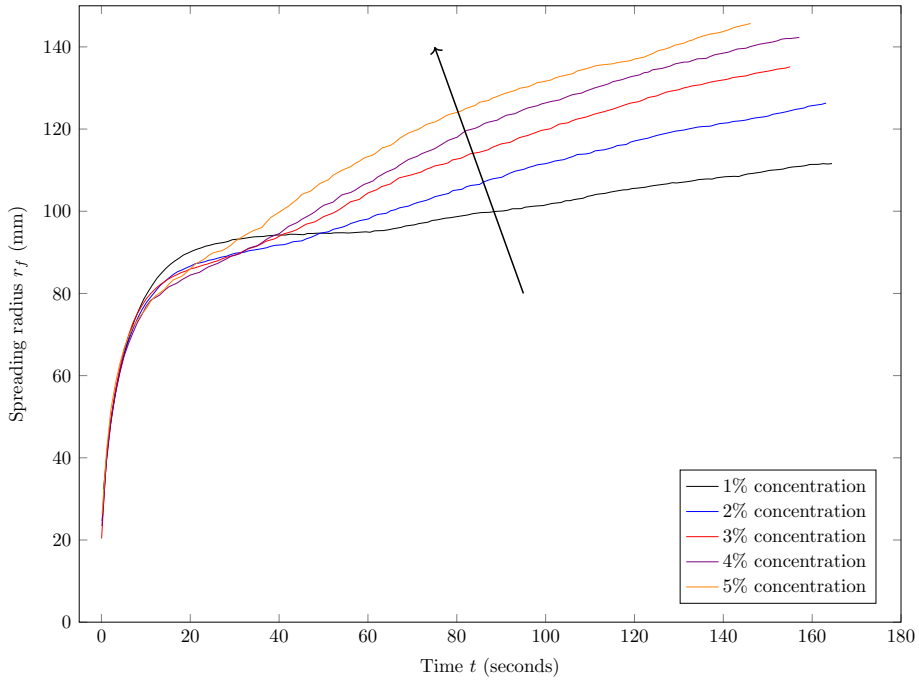

Figure 4.1: Spreading radius of the gravity current for different volume concentrations measured against time. The measurements were taken by Box [22], the experimental parameters are provided in table 4.1. The arrow indicates the ordering for different volume concentrations, that is, gravity currents with higher particle concentrations spread farther.

Nondimensionalisation

For the nondimensionalisation, we start with the influx condition (4.8) to obtain a scaling for h

$$h = \left(\frac{3\mu Q}{2\pi\Delta\rho g}\right)^{1/4} H. \tag{4.13}$$

From this, we can infer the scalings for r and t as

$$r = \left(\frac{\mu Q}{2\pi\Delta\rho g k_d}\right)^{1/2} R \quad \text{and} \quad t = \left(\frac{3\mu^5 Q}{2\pi\Delta\rho^5 g^5 k_d^4}\right)^{1/4} T, \tag{4.14}$$

and so we obtain the dimensionless PDE

$$\frac{\partial H}{\partial T} = \frac{1}{R}\frac{\partial}{\partial R}\left(RH^3\frac{\partial H}{\partial R}\right) - \lambda\left(1 + \frac{H}{\delta}\right), \tag{4.15}$$

subject to the boundary conditions $H(R_F, t) = 0$, where R_F is the dimensionless spreading radius, conservation of mass at the front

$$RH^3\frac{\partial H}{\partial R}\bigg|_{(R_F,t)} = 0, \tag{4.16}$$

and the constant influx condition

$$\lim_{R\to 0} RH^3 \frac{\partial H}{\partial R} = -1. \tag{4.17}$$

The dimensionless parameter δ measures the height scale of the current against the depth of the membrane, i.e.

$$\delta = \left(\frac{3\mu Q}{2\pi\Delta\rho g}\right)^{-1/4} d. \tag{4.18}$$

In the next section, we will determine the spreading radius in the limit when δ is very small or very large if we neglect clogging. We will also show how these two limits relate to the steady-state spreading radius of the general case $\delta \in (0, \infty)$. We display the results of our nondimensionalisation later on in figure 4.5, where we compare the experimental results with our numerical predictions.

For the governing equations for the probabilities $P_k(r, t)$, we additionally nondimensionalise the constant c as

$$c = \left(\frac{3\mu Q}{2\pi\Delta\rho g}\right)^{-1/4} C \tag{4.19}$$

to obtain

$$\frac{\mathrm{d}P_0}{\mathrm{d}T} = -C\lambda_0 P_0 \left(1 + \frac{H}{\delta}\right) \tag{4.20a}$$

$$\frac{\mathrm{d}P_n}{\mathrm{d}T} = C\left(-\lambda_k P_n + \lambda_{k-1} P_{n-1}\right)\left(1 + \frac{H}{\delta}\right) \quad n \geq 1, \tag{4.20b}$$

subject to the initial conditions $P_0(x, 0) = 1$ and $P_n(x, 0) = 0$ for $n \geq 1$.

4.2.2 Asymptotic results

In this subsection, we consider the case where there is no clogging, that is, $C = 0$, which results in the gravity current only reaching a finite spreading radius. This is helpful for comparing the spreading radius of the particle laden solution with the expected maximum spreading radius when there would be no particles included.

From our nondimensionalisation, we have retained the dimensionless parameter δ which measures the ratio of the height-scale of the current to the thickness of the mesh. If δ is small, the membrane is thin compared to the height of the current and so the drainage will mostly be driven by the hydrostatic pressure of the current. If, on the other hand, δ is large, then the membrane will be deep compared to the height

of the current and so the drainage will be mostly driven by the weight of the liquid in the membrane.

We begin by reviewing the case where δ is large to recover Spannuth et al.'s solution [112], albeit with different constants due to a slightly different nondimensionalisation. The solution to the case where δ is small, which is mentioned but not solved by Pritchard et al. [97], is novel to our best knowledge, and we solve it using an asymptotic expansion around the front of the current in the style of Huppert [61]. We conclude by determining the finite spreading radius for different orders of magnitude of δ using asymptotic expansions and a shooting method and we recover the two asymptotic limits, for which we also claim originality.

4.2.2.1 Steady state for large δ

When δ is large, we neglect the H/δ term in (4.15). This is equivalent to an drainage driven by background flow [97], although this is only applicable where $H > 0$. The maximum spreading radius will be attained when a steady state is reached, and so we have to solve

$$\frac{\mathrm{d}}{\mathrm{d}R}\left(RH^3\frac{\mathrm{d}H}{\mathrm{d}R}\right) = R. \tag{4.21}$$

This can be integrated directly using the dimensionless influx boundary condition (4.17) and conservation of mass condition at the front (4.16) to obtain a steady-state maximum spreading radius $R_F = \sqrt{2}$, or, in dimensional terms,

$$r_f = \left(\frac{\mu Q}{\pi\Delta\rho g k_d}\right)^{1/2}. \tag{4.22}$$

By writing H^3H' as $(H^4)'/4$, we can integrate once more to also obtain the steady shape

$$H(R) = \left(R^2 - 4\log\left[\frac{1}{\sqrt{2}}R\right] - 2\right)^{1/4}. \tag{4.23}$$

We will use this result to validate our numerics.

4.2.2.2 Asymptotics for small δ

For small δ, we rescale $T = \delta\tilde{T}$ and $R = \sqrt{\delta}\tilde{R}$, but do not rescale $H = \tilde{H}$ to leave the influx condition (4.17) consistent. Using this rescaling in (4.15), multiplying by δ, and neglecting the small terms, we arrive at

$$\frac{\partial\tilde{H}}{\partial\tilde{T}} = \frac{1}{\tilde{R}}\frac{\partial}{\partial\tilde{R}}\left(\tilde{R}\tilde{H}^3\frac{\partial\tilde{H}}{\partial\tilde{R}}\right) - \tilde{H}. \tag{4.24}$$

In this equation, we can consider the behaviour for the spreading of the gravity current for very early times and the steady state in late times. For very early times, we rescale $\tilde{R} = \sqrt{\epsilon}\hat{R}$, $\tilde{T} = \epsilon\hat{T}$, and, leaving $\tilde{H} = \hat{H}$ unscaled to keep the influx condition, we obtain, after multiplying by ϵ and neglecting the small terms,

$$\frac{\partial \hat{H}}{\partial \hat{T}} = \frac{1}{\hat{R}}\frac{\partial}{\partial \hat{R}}\left(\hat{R}\hat{H}^3\frac{\partial \hat{H}}{\partial \hat{R}}\right), \tag{4.25}$$

which is the standard equation governing the spreading of an axisymmetric gravity current under constant influx (4.17). We can recover Huppert's solution [61] in dimensionless terms as

$$\hat{R}_F(T) \approx 1.4244 T^{1/2}, \tag{4.26}$$

which we will use for the validation of our numerical methods.

More interestingly, to compute the maximum spreading radius we have to solve the dimensionless steady-state equation of (4.24)

$$\left(\tilde{R}\tilde{H}^3\tilde{H}'\right)' = \tilde{R}\tilde{H}, \tag{4.27}$$

subject to the boundary conditions

$$\tilde{R}\tilde{H}^3\tilde{H}'|_{\tilde{R}=\tilde{R}_F} = 0 \quad \text{and} \quad \lim_{\tilde{R}\to 0}\tilde{R}\tilde{H}^3\tilde{H}' = -1. \tag{4.28}$$

We scale $z = \tilde{R}/\tilde{R}_F$ and $\tilde{H} = \tilde{R}_F^{2/3}\psi$ to obtain

$$\left(z\psi^3\psi'\right)' = z\psi, \tag{4.29}$$

subject to the boundary conditions

$$z\psi^3\psi'|_{z=1} = 0, \quad \psi(1) = 0, \quad \text{and} \quad \lim_{z\to 0} z\psi^3\psi' = -\frac{1}{\tilde{R}_F^{2/3}}. \tag{4.30}$$

We can use the influx boundary condition to compute $\tilde{R}_F$ once we have solved the problem numerically, as the inflow has to match the drainage and so

$$\tilde{R}_F = \left(\int_0^1 z\psi \, \mathrm{d}z\right)^{-3/2}. \tag{4.31}$$

As we are not aware of an analytic solution to (4.29), we seek an approximate solution by expanding around the front, set $z = 1 - x$, so that

$$\left((1-x)\psi^3\psi'\right)' = (1-x)\psi. \tag{4.32}$$

Choosing x to be small, we obtain the equation

$$\frac{1}{4}(\psi^3)' = \psi. \tag{4.33}$$

By expanding $\psi \sim \gamma(1-x)^\alpha$ and balancing powers, we obtain $\alpha = \frac{2}{3}$ and $\gamma = \left(\frac{9}{10}\right)^{1/3}$ and so

$$\psi = \left(\frac{9}{10}\right)^{1/3}(1-x)^{2/3} + O((1-x)^{5/3}). \tag{4.34}$$

We can use the expansion provide an approximation for the derivative of ψ at the front, the results are displayed in figure 4.2a. Numerical computations yield $\tilde{R}_F \approx 1.7294$. Hence, we obtain, in dimensional terms

$$r_f \approx 1.7294\left(\frac{d}{3K}\left(\frac{3\mu Q}{2\pi\Delta\rho g}\right)^{3/4}\right)^{1/2}. \tag{4.35}$$

4.2.2.3 Spreading radius for general δ

Finally, let us compute the steady-state spreading radius for $\delta \in (0,\infty)$, that is, the drainage will be driven both by the hydrostatic pressure of the gravity current and the weight of the liquid in the membrane. For this, we have to solve the steady-state equation of (4.15),

$$\frac{\mathrm{d}}{\mathrm{d}R}\left(RH^3\frac{\mathrm{d}H}{\mathrm{d}R}\right) = R\left(1+\frac{H}{\delta}\right), \tag{4.36}$$

subject to the influx condition $RH^3\mathrm{d}H/\mathrm{d}R = -1$ as $R \to 0$ and the conservation of mass at the front condition $RH^3H' = 0$ at $R = R_F$. We are not aware of a closed-form solution, and so we solve this numerically for any given δ via a shooting method for R_F. However, to solve (4.36) numerically, we require a boundary condition for H' at R_F. This condition for the derivative will be obtained by an asymptotic analysis for the behaviour around the front. We rescale $z = R/R_F$ to obtain

$$(zH^3H')' = R_F^2\left(z+\frac{zH}{\delta}\right), \tag{4.37}$$

subject to the new boundary conditions $H(1) = 0$ and $zH^3H' = 0$ at $z = 1$, the influx condition remains as is. We are interested in balancing the terms as $z \to 1$, thus use $z = 1-x$ and neglect all small terms to obtain

$$(H^3H')' = R_F^2 + R_F^2\frac{H}{\delta}. \tag{4.38}$$

Now, $H \to 0$ as $x \to 0$, but R_F^2 is a constant, which has to be balanced by $(H^3H')'$, hence

$$H \sim \left(2R_F^2\right)^{1/4}(1-x)^{1/2} \quad \text{as } x \to 0. \tag{4.39}$$

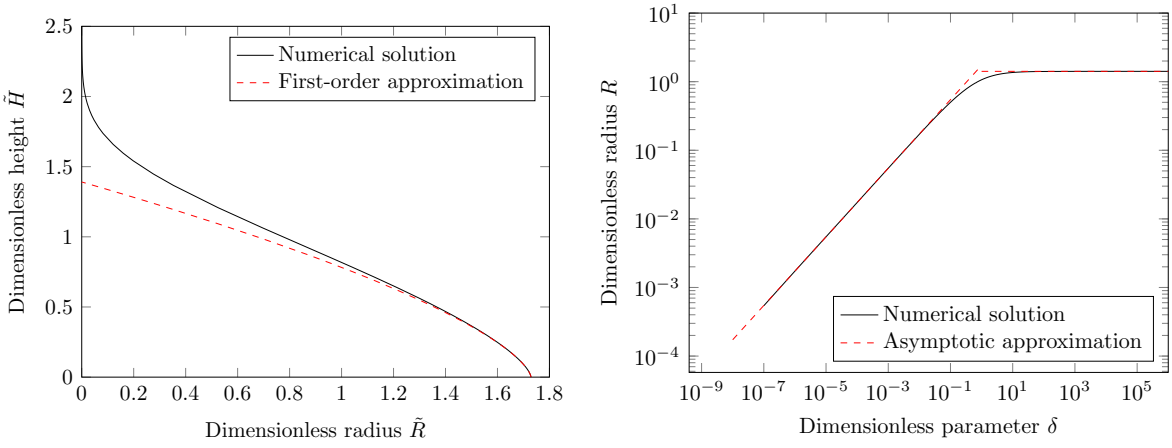

(a) (b)

Figure 4.2: In (a), the solution to the steady-state height-driven drainage (4.27) and its asymptotic expansion (4.34) are shown. In (b), we show the steady-state spreading radius for different δ. Note the two asymptotic regimes: For large δ, the spreading radius approaches the limit of $\sqrt{2}$; for small δ, we recover the height-driven radius of $1.7294\sqrt{\delta}$.

We can explain this physically, as the weight driven drainage in the porous medium is constant, which will eventually become bigger than the height driven drainage as the hydrostatic head goes to zero, so all the flux that goes right to the front is exclusively balancing the weight-driven drainage.

We use the expansion (4.39) to provide an initial condition on the derivative of H. For the shooting method, we compute the influx I via

$$I = R_F^2 \int_0^1 z \left(1 + \frac{H}{\delta}\right) \, \mathrm{d}z, \tag{4.40}$$

because the outflow and the influx have to balance in the steady state. If the computed influx is larger than 1, R_F has to be smaller, and if the influx is less than 1, then it must be larger. We use $[0, \sqrt{2}]$ as the initial interval for the shooting method, as the current has to have a positive radius but will be smaller than the steady position when $\delta \to \infty$. This is because, for $\delta \in (0, \infty)$, the drainage is driven both by the height and by the weight of the fluid within the membrane and so the outflow will be larger than if it were driven by the weight of the fluid in the membrane alone.

The numerical results are shown in figure 4.2b. We recover the two asymptotic limits that we determined analytically: For large δ, the spreading radius converges to $\sqrt{2}$ as the drainage will be mostly driven by the weight of the fluid in the membrane. For small δ, we use the scaling $R = \sqrt{\delta}\tilde{R}$ from our asymptotic analysis to recover

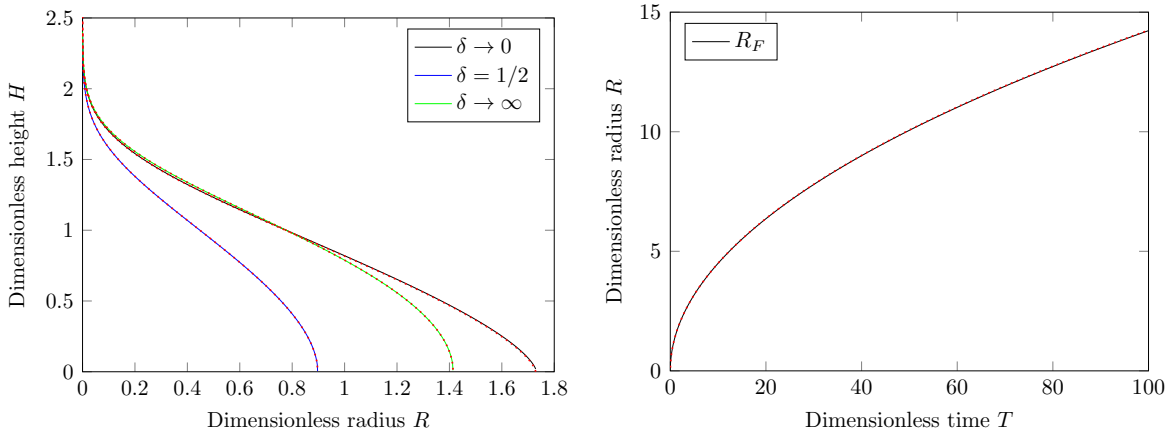

(a) (b)

Figure 4.3: Validation of the numerical method for solving the equation (4.15) for the shape of the gravity current. In (a), we compare the steady shapes for background-flow drainage ($\delta \to \infty$), height-driven drainage ($\delta \to 0$), and a mixed combination ($\delta = 0.5$) with the corresponding exact solutions (red dots). In (b), we compare the position of the front of an axisymmetric gravity current with no drainage ($\lambda = 0$) with the exact solution $R_F(T) \approx 1.4244T^{1/2}$. For both instances, we obtain excellent agreement between the numerical and the exact solutions.

that $R_F \sim 1.7294\sqrt{\delta}$, where the constant is given by considering the gravity-driven drainage alone.

In the next section, we will discuss the numerical methods used to solve the time-dependent problem when clogging is included.

4.2.3 Numerical methods for the full problem

To obtain higher accuracy at early times and to make evaluating the spreading of the current for large times possible, we map the domain from the inlet to the front to a fixed domain. In the experiments, the inlet is a circular annulus of positive radius instead of a point source, which we will account for in our numerical methods. We use the coordinate transform

$$\eta = \frac{R - R_0}{S(T)} \tag{4.41}$$

for $R_0 \leq R \leq R_F$, where R_0 denotes the dimensionless radius of the inlet and $S(T) = R_F(T) - R_0$ the radial extension of the gravity current from the annulus to the front. Then, the dimensionless PDE for the height of the fluid (4.15) becomes

$$\frac{\partial H}{\partial T} - \frac{\eta}{S}\frac{\mathrm{d}S}{\mathrm{d}T}\frac{\partial H}{\partial \eta} = \frac{1}{S(S\eta + R_0)}\frac{\partial}{\partial \eta}\left(\frac{S\eta + R_0}{S}H^3\frac{\partial H}{\partial \eta}\right) - \lambda\left(1 + \frac{H}{\delta}\right), \tag{4.42}$$

subject to the boundary conditions $H(1) = 0$,

$$\frac{S + R_0}{S} H^3 \frac{\partial H}{\partial \eta}\bigg|_{(1,T)} = 0, \quad \text{and} \quad \frac{R_0}{S} H^3 \frac{\partial H}{\partial \eta}\bigg|_{(0,T)} = -1. \tag{4.43}$$

Additionally, we obtain the kinematic boundary condition for the evolution of the front by dividing the flux $H^3/S\partial H/\partial\eta$ by the height H,

$$\frac{\mathrm{d}S}{\mathrm{d}T} = \frac{1}{S(T)} H^2 \frac{\partial H}{\partial \eta} = \frac{1}{3S(T)} \frac{\partial H^3}{\partial \eta} \quad \text{at } \eta = 1. \tag{4.44}$$

For λ, we note that

$$\frac{\mathrm{d}\lambda(\eta, T)}{\mathrm{d}T} = \sum_{n=0}^{\infty} \lambda_n \frac{\mathrm{d}P_n(\eta, T)}{\mathrm{d}T} \tag{4.45}$$

and for each probability P_n, we have

$$\frac{\partial P_n}{\partial T} - \frac{\eta}{S} \frac{\mathrm{d}S}{\mathrm{d}T} \frac{\partial P_n}{\partial \eta} = C(-\lambda_n P_n + \lambda_{n-1} P_{n-1}) \left(1 + \frac{h}{\delta}\right), \tag{4.46}$$

where we assume $\lambda_{-1} = 0$ for consistency and impose the initial conditions $P_0(\eta, 0) = 1$ and $P_n(\eta, 0) = 0$ for $n \geq 1$ as well as the boundary conditions $P_0(1, t) = 1$ and $P_n(1, t) = 0$ for $n \geq 1$. The system of equations (4.42) and (4.46) can be solved using a finite-difference discretisation and the method of lines. From a practical perspective, we point out that it is of course only feasible to consider finitely many P_n, which is equivalent to setting $\lambda_N = 0$ for some N. If M is the number of interpolation points in the discretisation of η, this leads to $M \cdot (N + 1) + 1$ equations in total, M for the height, $M \cdot N$ for the probabilities P_N, and 1 for the position of the front.

We validate our method in two ways. Using the results from 4.2.2, for $\delta \to 0, \infty$, and $\delta = 0.5$ we compare the numerically obtained steady states with the exact results; this is shown in figure 4.3a. We then compare the numerical spreading radius for no drainage against the exact analytical solution (4.26); this is shown in figure 4.3b.

4.2.4 Description of the experiments

The experiments described in this section were conducted independently by Box [22]. For each experiment, a gravity current was created by letting glycerol flow through a circular annulus (diameter $d = 16$ mm) onto a thin porous mesh with hexagonal holes of width 6.5 mm across flats. The annulus was located at the centre of the mesh and fed from below with a constant flux, which was achieved by maintaining a constant pressure head. The mesh consisted of a woven stainless steel mesh (thickness $b = 0.25$ mm) on top of a perforated aluminium sheet (thickness $b = 0.8$ mm). Here,

(a)

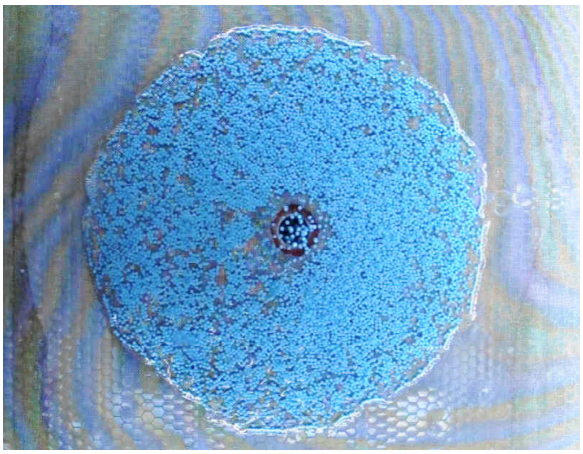

(b)

Figure 4.4: Two pictures from the experiment, (a) the side-view of the gravity current and (b) the top-down view.

the steel mesh played the role of the semipermeable membrane while the aluminium mesh was used to prevent deformations due to the weight of the fluid. Before the start of the experiments, the steel mesh was pre-wetted by applying glycerol with a brush in a circular fashion.

Density matched Cellulose Acetate polymer spheres of 2.0 mm diameter were used as particles in the glycerol. Several experiments were conducted with different volume ratios, ranging from 1% to 15%, although we only consider the experiments with concentrations up to 5% as the experiments with higher concentrations exhibited frontal instabilities and behaved more like a dense granular suspension. The spreading of the gravity current was filmed from the top, and Matlab was used to infer the position of the front of the gravity current afterwards. For the observed volume ratios, instabilities at the front were negligible and so defining the position of the front was unambiguous. A top-down and a side-view picture from the experiment are shown in figure 4.4.

4.2.5 Comparison with experiments

For the comparison with the experiments we need to determine the experimental parameters necessary for the nondimensionalisation. These were measured by Box [22]. The density difference between glycerol and air was constant as $\Delta\rho = 1260\text{kg/m}^3$. The concentration, viscosity, and influx differed between the experimental runs, their values for each run are reported in table 4.1.

The remaining parameter to be determined is the effective permeability k_d, the product of the permeability and the porosity of the mesh. This is discussed in the next subsection.

4.2.5.1 Computing the permeability of the mesh

Let us consider a fluid column draining through a permeable medium of thickness d. For low-Reynolds-number flow, the pressure $p(z,t)$ in the fluid is hydrostatic, i.e.

$$p(z,t) = p_0 + \rho g(h(t) - z), \quad 0 \leq z \leq h(t), \tag{4.47}$$

where p_0 denotes the ambient pressure, ρ the density of the liquid, g the gravitational acceleration and $h(t)$ the height of the liquid at time t, which is uniform across the mesh and therefore only depends on t. The drainage velocity v of the liquid is then assumed to follow Darcy's law

$$\frac{\mu v}{k} = -\frac{\partial p}{\partial z} - \rho g, \tag{4.48}$$

where μ denotes the dynamic viscosity of the liquid and k the permeability of the porous medium. To determine the pressure within the porous medium, we can combine Darcy's law (4.48) and conservation of volume $\nabla \cdot v = 0$ to obtain

$$\frac{\partial^2 p}{\partial z^2} = 0. \tag{4.49}$$

Together with the boundary conditions $p = p_0$ at $z = -d$ and $p = p_0 + \rho g h$ at $z = 0$, we obtain

$$p(z,t) = p_0 + \rho g h \left(1 + \frac{z}{d}\right), \quad 0 \geq z \geq -d. \tag{4.50}$$

Combining (4.48) with (4.50) yields

$$\frac{\mathrm{d}h}{\mathrm{d}t} = \phi v = -\frac{\Delta \rho g \phi k}{\mu}\left(1 + \frac{h}{d}\right), \tag{4.51}$$

which has, writing $\tau = \Delta \rho g \phi k / \mu$, the solution

$$h(t) = (h_0 + d)e^{-\tau t} - d. \tag{4.52}$$

Note that if $h \gg d$ it is often sufficient to use the ansatz $h = h_0 e^{-\tau t}$. We used least-squares approximation to fit experimental measurements and obtain

$$k_d = k\phi \approx 8.03 \cdot 10^{-9}\mathrm{m}^2. \tag{4.53}$$

Parameter	Run 1	Run 2	Run 3	Run 4	Run 5
Concentration	1%	2%	3%	4%	5%
Q (ml/s)	16.47	15.96	16.42	16.43	17.31
μ_0 (Pa·s)	0.72	0.69	0.67	0.65	0.63

Table 4.1: Parameter values for the different experimental runs, measured by Box [22]. The decrease in the viscosity μ_0 of the liquid is suspected to be due to absorption of moisture from the air.

4.2.5.2 Comparison with the model

To fit our model to the experiments, we need to fit the clogging parameters $\lambda_1, \lambda_2, \ldots$, which constitutes the inverse problem of finding the clogging law from the spreading speed of a gravity current. As we do not observe more than 3 spheres stacking up on each other, we assume that $\lambda_4 = 0$, hence we only have to determine the three parameters $\lambda_1, \lambda_2, \lambda_3$ that govern the reduction in permeability due to clogging. For the parameter estimation, we note that $\lambda_1 \geq \lambda_2 \geq \lambda_3$ and we obtain a first approximation by assuming that each $\lambda_i \in \{0, 0.1, 0.2, \ldots 1.0\}$. We determine a best fit by comparing against the results of Run 1, as defined in table 4.1, using the L^2 norm. The first parameter sweep, where we evaluate all 286 combinations of $(\lambda_1, \lambda_2, \lambda_3) \in \{0, 0.1, 0.2, \ldots 1.0\}^3$ with $\lambda_1 \geq \lambda_2 \geq \lambda_3$, yields $\lambda_1 = 0.2$, $\lambda_2 = 0$ and $\lambda_3 = 0$ and we run a second parameter sweep on $\lambda_1 \in \{0.15, 0.16, \ldots 0.25\}$, $\lambda_2, \lambda_3 \in \{0, 0.01, \ldots 0.1\}$ to obtain $\lambda_1 = 0.16$, $\lambda_2 = 0.01$ and $\lambda_3 = 0$.

The results of this fitting and the associated L_2 error between the model and the experimental measurements are shown in figure 4.5. While the fitting was done for the 1% concentration run, we observe a good quantitative and qualitative fit with the other runs as well, although especially for the higher concentrations, certain features of the behaviour around $T = 0.5$ are not well captured. The most probable reason for this is that there are certain aspects of the experiments that our model does not capture, such as no particles depositing right around the annulus due to shear forces. Nevertheless, the good fit shows that our model is suitable to predict the spreading of a particle laden gravity current, and, more importantly, serves as an indication that it could be possible to determine the filtration law from the spreading speed of a gravity current.

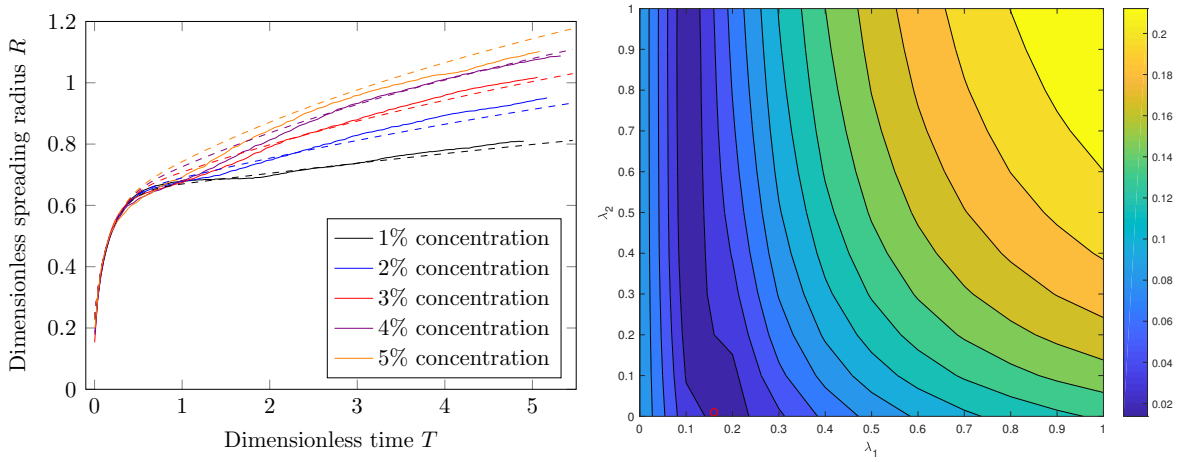

(a) (b)

Figure 4.5: (a) Comparison of the dimensionless front positions for the experiment (solid) and the prediction (dashed). (b) Contourplot of the sum of the L_2 errors between the model and the experimental measurements over all 5 different runs, the minimum is indicated by a red circle. While the evidence is strong for λ_1, the differences in the L_2 error for λ_2 would become more apparent if the experiments would run for longer.

4.2.6 Summary

In this subsection, we have discussed how to determine a discrete filtration law from the spreading speed of a particle-laden gravity current on a porous mesh. We derived a mathematical model that combined the well-known theory of gravity currents with our work on stochastic modelling of membrane filtration to homogenise the finite-size effects of clogging. Looking at the finite spreading radius of a gravity current when neglecting clogging, we determined the spreading radii for the limiting cases of a very thin and very deep mesh and showed how these two cases serve as asymptotic limits to the more general problem when we have a positive, finite depth of the mesh. To solve the coupled problem of spreading and clogging, we then discussed our numerical approach using a fixed-interval mapping both for the spreading of the current and our clogging law. After describing the experiments, we showed how we determined the clogging law using a parameter sweep and showed the good agreement between the experiments and our numerical predictions.

We will discuss potential improvements of the model and next steps in the conclusion of this chapter. In the next section, we look at the problem of finding the filtration law from the position of the spreading front of a gravity current when we assume a continuous filtration law and show how we can use the asymptotic growth

of the position of the front to correctly infer the filtration law.

4.3 Inferring continuous filtration laws from the porous medium equation with absorption and clogging

In the first half of this chapter, we proposed a solution to the inverse problem of determining the filtration law from the spreading position of a particle laden gravity current on a membrane using a parameter sweep and L^2 fitting. This approach was employed because the experiments indicated that no more than three particles would stack onto each other. If the dimension of the search space had been much larger, this approach would not have been computationally feasible, however. Therefore, a different method is needed when the expected number of particles retained per pore is large.

In this section, we will consider the inverse problem of determining a continuous filtration law by observing the position of the front of a gravity current over time. We will not consider *any* filtration law, however, but only consider those of a specific form motivated by Hermia's four blocking laws [50] for the decrease in flux Q,

$$\frac{\mathrm{d}Q}{\mathrm{d}t} = -rQ^k\Delta P. \tag{4.54}$$

Here, the parameters r and $k = 1, 3/2, 2, 3$ depend on the mode of filtration (see Chapter 1, set $k = 3-n$) and ΔP denotes the pressure applied across the membrane. Let us rewrite $Q(t) = \lambda(t)Q(0)$, so that λ takes the role of the dimensionless *permeability factor*. If the applied pressure gradient ΔP is hydrostatic, that is, $\Delta P = \rho g h$ for a fluid of density ρ and height h, g denotes the gravitational acceleration, we can rewrite (4.54) as

$$\frac{\mathrm{d}\lambda}{\mathrm{d}t} = -c_\alpha \lambda^\alpha h, \tag{4.55}$$

where $c_\alpha = r\rho g Q(0)^{\alpha-1}$. Instead of only considering $\alpha \in \{1, 3/2, 2, 3\}$ in (4.55), we will allow $\alpha \in \mathbb{R}$ and identify the limiting cases $\alpha \to -\infty, \infty$ with $\lambda \equiv 0$ and $\lambda \equiv 1$ respectively. While different filtration modes can occur simultaneously during filtration runs, we emphasize that we only assume one filtration mode α to be present.

To model the spreading of the gravity current of the membrane, we use the one-dimensional generalisation of the thin film equation discussed in the previous section, the *porous medium equation with absorption*

$$\frac{\partial h}{\partial t} = \frac{\partial}{\partial x}\left(h^n \frac{\partial h}{\partial x}\right) - \lambda h^q, \tag{4.56}$$

where the exponents q and n are constants and h denotes the height of a gravity current, although the equation can also be used to model other quantities of interest such as the density of a gas. We use the one-dimensional instead of the axisymmetric equation as this simplification facilitates the analysis. However, we expect our results to be transferable to the axisymmetric case as well. The porous medium equation with absorption is used in a variety of applications, including modelling wound healing [106], thermal propagation [51], or population dynamics [48], with q taking on different values [40]. In this chapter, we will only consider standard absorption, that is, $q = 1$.

The *porous medium equation* (equation (4.56) with $\lambda \equiv 0$) can be derived to model the density of a homogeneous gas flowing through a homogeneous porous medium following the argumentation of Aronson [5], where the different exponents n arise due to the constitutive equation relating the density ρ_g and the pressure p of a given gas via

$$\rho_g = c_0 p^\gamma. \tag{4.57}$$

Here, c_0 is a constant and $\gamma \in (0, 1)$ if the flow of the gas in the porous medium is adiabatic. Using conservation of mass and Darcy's law for the motion of the gas in the porous medium, one can recover the porous medium equation (4.56) by setting $n = \gamma^{-1}$ and interpreting h as the dimensionless density. Within the area of gravity currents, the porous medium equation is of interest when studying the spreading of some liquid in air ($n = 3$) [61] or within a porous medium ($n = 1$) [2]. From a theoretical perspective, the Cauchy problem of the porous medium equation has been widely studied [119].

Motivated by the experiments in the first half of this chapter, however, we are interested in a Neumann type problem where we can impose the influx $I(t)$ as

$$h^n \frac{\partial h}{\partial x} = -I(t) \quad \text{at } x = 0, \tag{4.58}$$

and the initial height of the current is zero, i.e. $h(x, 0) = 0$. The central question of this section is whether and how we can determine the filtration mode α by tracking position of the front

$$x_f(t) = \min_{x \geq 0} \{h(x, t) = 0\}, \tag{4.59}$$

and imposing a suitable $I(t)$?

We restrict our analysis to positive exponents $n \geq 1$, although we note that the case $n < 0$ is for example employed in modelling cell dynamics [88]. For $\lambda = 0$, we note that there are two special limiting cases of $n = 0$, which, depending on the scaling of the data, is either the *Heat equation* or the *Eikonal equation* [119], and

$n \to \infty$, which is the *Mesa problem* [37]. We will not study these limits and do not expect our results to be valid in those instances as it is not clear whether the mathematical techniques used in this section are applicable to those limits.

In the next section, Section 4.3.1, we will combine the ideas of this section to assemble and nondimensionalise our mathematical model. In Section 4.3.2, we will consider the long-term behaviour under constant influx and show that the position of the front follows a power law asymptotically for large t. Furthermore, we will show that the power law is unique for $\alpha > 2 + 1/(n+2)$. In Section 4.3.3, we will show that our system of equations exhibits a *travelling wave* solution for a suitable influx. The travelling wave solution will allow us to devise a method for determining α when $\alpha < 1$.

To our best knowledge, the content in this half of the chapter is novel except where stated otherwise.

4.3.1 Mathematical model and nondimensionalisation

We obtain the mathematical model for the spreading of a gravity current of height h on a membrane by combining the dimensional porous medium equation with absorption (4.56) with a generalised version of the four filtration laws (4.55),

$$\frac{\partial h}{\partial t} = c_n \frac{\partial}{\partial x}\left(h^n \frac{\partial h}{\partial x}\right) - c_{\text{imb}} \lambda h, \tag{4.60a}$$

$$\frac{\partial \lambda}{\partial t} = -c_\alpha \lambda^\alpha h, \tag{4.60b}$$

where c_n, c_{imb} and c_α are constants that depend on n and α. While the notion of "height" is motivated by the instances of $n = 1$ or $n = 3$, we will refer to the quantity h as height for all $n \geq 1$ and use the metaphor of a gravity current spreading on a membrane accordingly. We note that all derivatives in x in (4.60) are of even order and so the system of equations is invariant under the transformation $x \mapsto -x$, hence it is sufficient to consider the problem for $x \geq 0$.

We assume the membrane to be initially dry and not yet clogged, hence we impose the initial conditions

$$h(x,0) = 0 \quad \text{and} \quad \lambda(x,0) = 1. \tag{4.61}$$

The gravity current has compact support, which we enforce by setting $h(x_f, t) = 0$ and requiring conservation of mass at the front,

$$c_n h^n \frac{\partial h}{\partial x}\bigg|_{(x_f,t)} = 0. \tag{4.62}$$

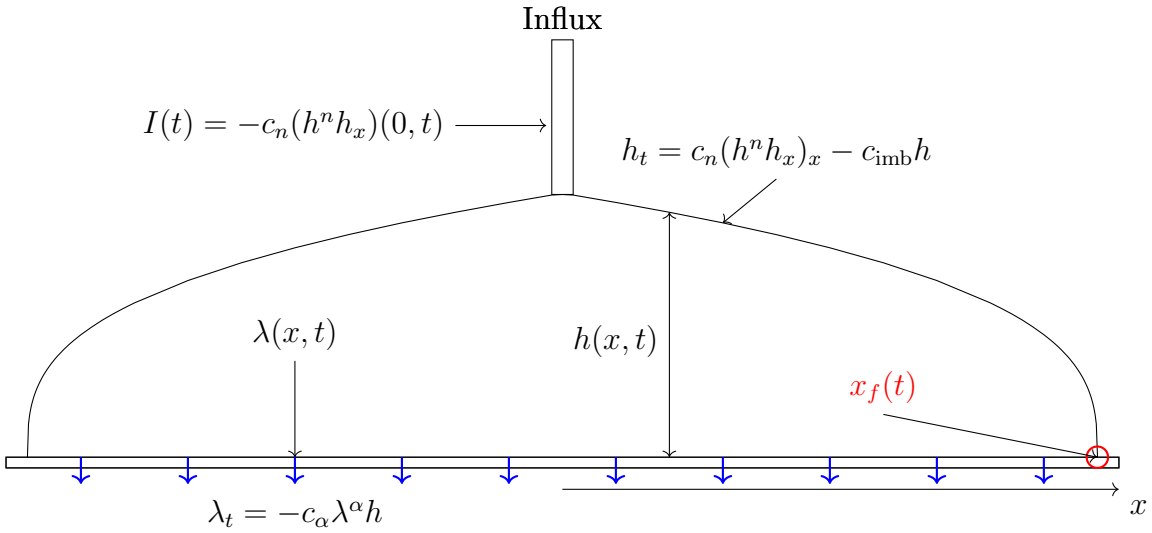

Figure 4.6: Visualisation of a solution to the full dimensional model (4.60). The solution to (4.60) is symmetric in x and so we only consider the solution for positive x. We are interested in inferring α from observations of $x_f(t)$.

Finally, the influx condition is given by

$$c_n h^n \frac{\partial h}{\partial x}\bigg|_{(0,t)} = -I(t) \quad \forall\, t > 0, \tag{4.63}$$

where $\partial h/\partial x = \lim_{x\to 0+}(h(x,t) - h(0,t))/x$ denotes the right-sided derivative. The full model is summarised and sketched in figure 4.6.

Nondimensionalisation

For the nondimensionalisation, we consider the case where the influx I is constant first. We have the influx condition

$$c_n h^n \frac{\partial h}{\partial x}\bigg|_{(0,t)} = -I, \tag{4.64}$$

and therefore choose the scaling $X = c_n H^{n+1}/I$ where $x = X\tilde{x}$. Using this transformation in the porous medium equation with drainage,

$$\frac{\partial h}{\partial t} = c_n \frac{\partial}{\partial x}\left(h^n \frac{\partial h}{\partial x}\right) - c_{\text{imb}}\lambda h, \tag{4.65}$$

we obtain the scaling $H = (I^2/(c_n c_{\text{imb}}))^{1/(n+2)}$, where $h = H\tilde{h}$ and $T = 1/c_{\text{imb}}$ with $t = T\tilde{t}$. Introducing the positive dimensionless parameter

$$\beta = \frac{c_\alpha}{c_{\text{imb}}}\left(\frac{I^2}{c_n c_{\text{imb}}}\right)^{1/(n+2)} \tag{4.66}$$

and dropping the tilde, we therefore obtain the system of equations

$$\frac{\partial h}{\partial t} = \left(h^n \frac{\partial h}{\partial x} \right) - \lambda h, \tag{4.67a}$$

$$\frac{\partial \lambda}{\partial t} = -\beta \lambda^\alpha h, \tag{4.67b}$$

subject to the initial conditions $h(x,0) = 0$, $\lambda(x,0) = 1$, the compact support-condition $h(x_f, t) = 0$, the conservation-of-mass condition

$$h^n \frac{\partial h}{\partial x}\bigg|_{(x_f,t)} = 0, \tag{4.68}$$

and the dimensionless influx condition

$$h^n \frac{\partial h}{\partial x}\bigg|_{(0,t)} = -1 \quad \forall t > 0. \tag{4.69}$$

For a variable influx $I(t)$, we can proceed analogously with the nondimensionalisation by using a reference scale for the influx.

4.3.2 Asymptotic results for constant influx

Our model contains two dimensionless parameters, the *filtration mode* α and the positive factor β. Note that we could rescale $\lambda = \beta^{1/\alpha}\tilde{\lambda}$. In the limit $\alpha \to \infty$ and $\alpha \to -\infty$, we would have $\lambda = \tilde{\lambda}$, and so we set w.l.o.g. $\beta = 1$ when considering these limiting cases.

The clogging parameter λ takes values in $[0,1]$. Hence, if $\alpha \to -\infty$, we know that λ^α is approaching infinity if $\lambda \neq 1$, thus the clogging will be very fast, and so we expect $\lambda \equiv 0$ in the limit of $\alpha \to -\infty$. This is the classical spreading without drainage problem, where we will generalise the approach of Huppert [61] to obtain a result that is valid for all n.

Conversely, for $\alpha \to \infty$, λ^α will be very small if $\lambda \neq 1$ and so we use $\lambda \equiv 1$ in the limit $\alpha \to \infty$. Therefore, we will only obtain a finite spreading radius, and we will determine the steady state and final spreading radius for all n, generalising a result by Pritchard et al. [97].

For the general case of $\alpha \in \mathbb{R}$, we will show that the position of the front and the height at $x = 0$ follow a power law each. We can use these power laws to determine a relationship between α and the position at the front, which will be unique for $\alpha > 2 + 1/(n+2)$, enabling a partial solution to the problem of finding α. All the results will be supported by numerical experiments.

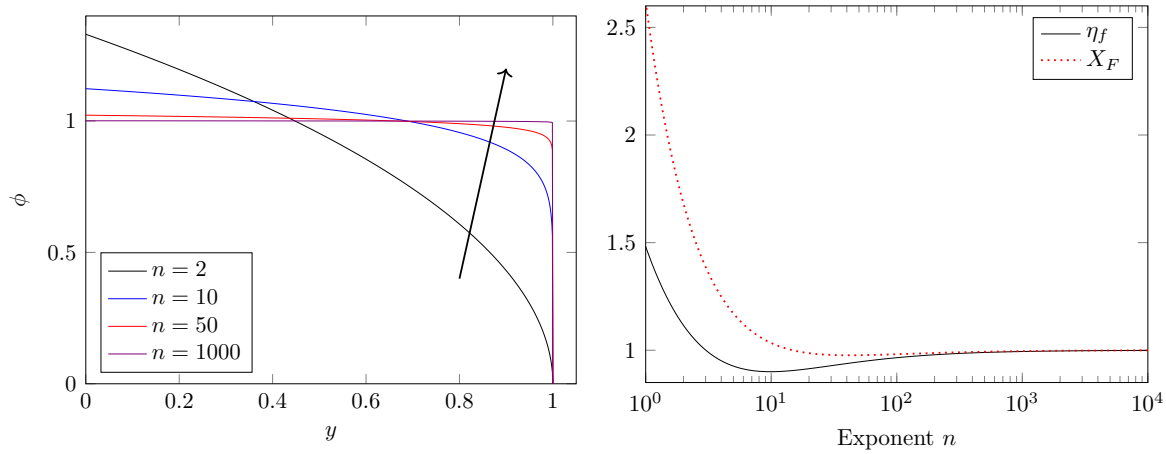

(a) (b)

Figure 4.7: (a) Numerical solutions to (4.74) for different values of n, the arrow indicates the increase in values of n. (b) Numerical evaluation of (4.75) to obtain η_F for different values of n ranging from 1 to 10^4. The steady-state spreading radius X_F for (4.77) was obtained from (4.79).

4.3.2.1 Spreading speed for no drainage

In the case of very fast clogging, that is, $\lambda \equiv 0$, we have to find a solution to the porous medium equation

$$\frac{\partial h}{\partial t} = \frac{\partial}{\partial x}\left(h^n \frac{\partial h}{\partial x}\right), \tag{4.70}$$

with the mass conservation condition (4.68) and constant influx condition (4.69) being equivalent to the volume condition

$$\int_0^{x_f(t)} h \, \mathrm{d}x = t. \tag{4.71}$$

Following Huppert [61], but letting n take any value greater than 1, we obtain a self-similar solution by introducing the scalings

$$\eta = x t^{-(n+1)/(n+2)} \quad \text{and} \quad h = \eta_F^{2/n} t^{1/(n+2)} \phi(y), \tag{4.72}$$

where $\eta_f = x_f(t) t^{-(n+1)/(n+2)}$ is the value of η at the front and $y = \eta/\eta_f$. An important consequence of this transformation is that the front of the current spreads as

$$x_f(t) \propto t^{(n+1)/(n+2)}. \tag{4.73}$$

The scalings (4.72) transform (4.70) into

$$(\phi^n \phi')' + \frac{n+1}{n+2} y \phi' - \frac{1}{n+2} \phi = 0, \tag{4.74}$$

subject to the boundary condition $\phi(1) = 0$ and the volume condition (4.71). We can then recover the value of η_f as

$$\eta_f = \left(\int_0^1 \phi \, \mathrm{d}y \right)^{-n/(n+2)}. \tag{4.75}$$

To solve (4.74), we use the same approach as in Section 4.2.2 since we are not aware of an analytical solution and expand ϕ around $y = 1$ as

$$\phi(y) = \left(\frac{n(n+1)}{n+2} \right)^{1/n} (1-y)^{1/n} + O\left((1-y)^{(n+1)/n} \right), \tag{4.76}$$

and use this as a starting condition for numerically obtaining ϕ. We plot solutions for ϕ for different values of n in figure 4.7a. We can then evaluate (4.75) numerically to obtain η_f; the results are shown in figure 4.7b. Note that the numerical results suggest $\eta_f \to 1$ as $n \to \infty$. We will show this mathematically in Section 4.3.3.

4.3.2.2 Steady state for constant drainage

In the case of no clogging, that is, $\lambda \equiv 1$, we expect the solution to the porous medium equation with absorption to reach a steady state where the influx and outflux balance. To obtain the steady-state solution, we solve the ODE

$$\frac{\mathrm{d}}{\mathrm{d}x} \left(h^n \frac{\mathrm{d}h}{\mathrm{d}x} \right) = h, \tag{4.77}$$

subject to the volume condition

$$\int_0^\infty h \, \mathrm{d}x = 1. \tag{4.78}$$

Using the ansatz $h = a\,(b - z)^k$, we obtain by a comparison of powers that $k = 2/n$ and $a = \left(\frac{n^2}{2n+4} \right)^{1/n}$. We can recover b from the influx condition to obtain the steady-state solution to (4.77)

$$h(x) = \left(\frac{n^2}{2n+4} \right)^{1/n} \left(\left(\frac{n}{2} \right)^{n/(n+2)} \left(\frac{2n+4}{n^2} \right)^{(n+1)/(n+2)} - x \right)^{2/n}, \tag{4.79}$$

and we obtain the finite spreading radius $X_F = \left(\frac{n}{2} \right)^{n/(n+2)} \left(\frac{2n+4}{n^2} \right)^{(n+1)/(n+2)}$ directly from the solution (4.79). The value of X_F is plotted in figure 4.7b. For $n \to \infty$, the steady-state spreading radius converges to 1.

4.3.2.3 Numerical methods

Since we are not aware of analytical solutions to the full model (4.67), we need to employ numerical methods. We are interested in the long-term behaviour of the solution, and so we introduce the mapping $\eta = x/x_f$ as in Section 4.2.3. We then obtain the transformed system for $\eta \in [0, 1]$ as

$$\frac{\partial h}{\partial t} - \frac{\dot{x}_f}{x_f}\eta\frac{\partial h}{\partial \eta} = \frac{1}{x_f^2}\frac{\partial}{\partial \eta}\left(h^n\frac{\partial h}{\partial \eta}\right) - \lambda h, \tag{4.80a}$$

$$\frac{\partial \lambda}{\partial t} - \frac{\dot{x}_f}{x_f}\eta\frac{\partial \lambda}{\partial \eta} = -\beta\lambda^\alpha h, \tag{4.80b}$$

subject to the boundary conditions $h(1) = 0$ and the transformed influx condition $(h^n h_x)(0, t) = -x_f(t)$. We use conservation of mass at the front (4.68) to obtain an equation for the spreading speed $\dot{x}_f$ by taking the limit of the flux, $h^n\partial h/\partial\eta$, divided by the height h for $\eta \to 1$,

$$\dot{x}_f = \lim_{\eta\to 1} h^{n-1}\frac{\partial h}{\partial \eta}. \tag{4.81}$$

For our numerical simulation, we use the method of lines with adaptive timesteps. For N interpolation points, we discretise h and λ in (4.80) at $\eta = 0/N, 1/N, \ldots (N-1)/N$ so that we can employ the boundary conditions $h(1) = 0$ and $\lambda(1) = 1$ implicitly. We typically choose around $N = 200$ interpolation points, which allows us to explore the spreading behaviour for large times up to $t = 10^{13}$.

4.3.2.4 Asymptotic results for the full problem

To study the asymptotic behaviour for $\alpha \in \mathbb{R}$ analytically, we choose the simplification $\beta = 1$ in (4.67) to obtain the system of PDEs

$$\frac{\partial h}{\partial t} = \frac{\partial}{\partial x}\left(h^n\frac{\partial h}{\partial x}\right) - \lambda h, \tag{4.82a}$$

$$\frac{\partial \lambda}{\partial t} = -\lambda^\alpha h, \tag{4.82b}$$

subject to the initial conditions $\lambda(x, 0) = 1,\ h(x, 0) = 0$ for $x \in \mathbb{R}$ and the boundary conditions $h(x_f, t) = 0$, $(h^n h_x)(x_f, t) = 0$, and $(h^n h_x)(0, t) = -1$ for $t > 0$. Motivated by numerical experiments, we assume that solutions to (4.82) are concave in x for h and monotonic in α. In other words, if (h_1, λ_1) solve (4.82) for α_1 and (h_2, λ_2) solve (4.82) for α_2 and $\alpha_1 < \alpha_2$ then $h_1 \geq h_2$.

Numerical solutions of (4.82) for $n = 3$ with $N = 200$ interpolation points, shown in figure 4.8, indicate that both the position of the front x_f and the height at the

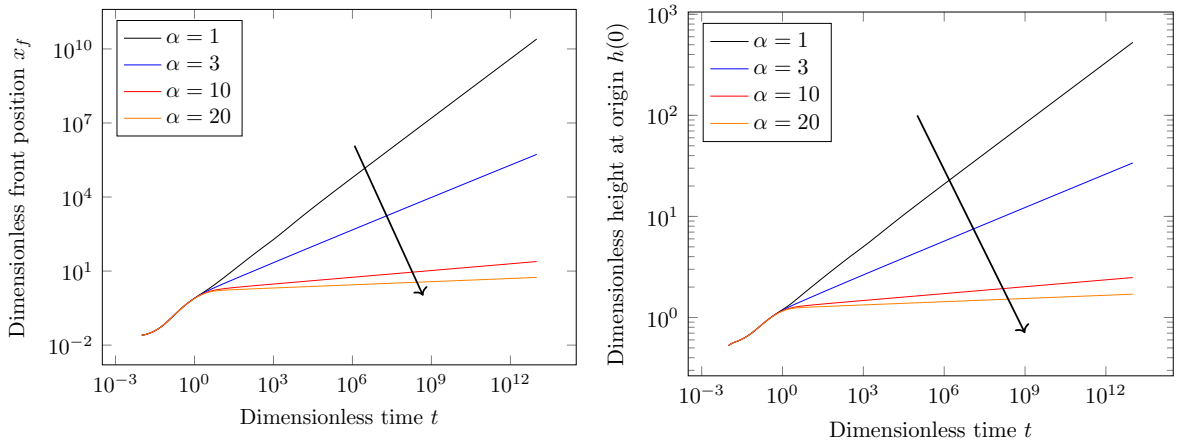

Figure 4.8: We show loglog plots of the (a) height at the origin and (b) position of the front for $n = 3$ and different values of α ($\beta = 1$), with the arrow used to indicate the increase in α. The results were obtained for $N = 200$ interpolation points and serve as an indication that both the height at the origin and the position of the front might follow a power law.

origin $h(0,t)$ follow a power law for large t. We therefore assume $x_f(t) \sim t^l$ and $h(0,t) \sim t^k$ and use the constant influx condition $(h^n h_x) = -1$ to suggest a relation between k and l as $l = (n+1)k$. We verify this assumption for different values of $n = 2, 3, 5$ and different values of α; the results are shown in figure 4.9.

To make progress with establishing a relationship between the exponent k for the height and the clogging mode α, we need to estimate the volume of the current and the total drainage asymptotically. Note that we can integrate (4.82a) w.r.t. x and t to obtain

$$\underbrace{\int_0^{x_f(t)} h \, \mathrm{d}x}_{=:V(t)} + \int_0^t \underbrace{\int_0^{x_f(t)} \lambda h \, \mathrm{d}x}_{=:D(t)} \, \mathrm{d}t = t. \tag{4.83}$$

This result states that the total influx is composed of the *volume* $V(t)$ and the integral of the instantaneous *drainage* $D(t)$. Hence, to balance the total influx t, either the volume term or the integral of the drainage (or both) must be of magnitude t asymptotically, as $t \to \infty$.

As we are assuming the solutions to (4.82) to be concave, we can bound the volume $V(t)$ of a current for sufficiently large t by

$$t \geq V(t) \gtrsim \frac{1}{2} t^{(n+2)k}, \tag{4.84}$$

where the lower bound is given by considering the area of the triangle obtained by connecting the origin, the position of the front $\sim (t^{(n+1)k}, 0)$ and the intersection with

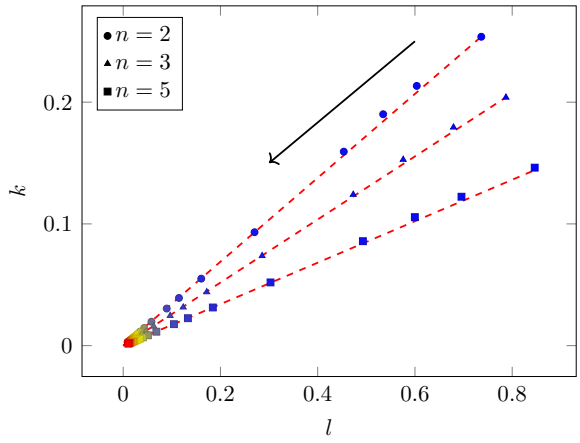

(a)

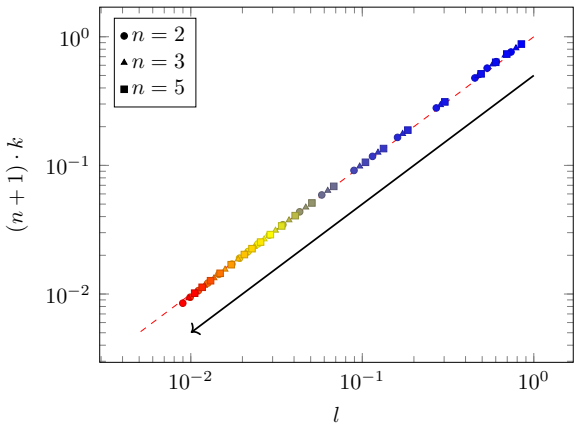

(b)

Figure 4.9: (a) We plot the value of k versus l for different values of α in the range of 1 to 100. The dashed red lines are obtained by interpolating between the results for the limiting cases of $\alpha = -\infty$ and $\alpha = \infty$. In (b), we obtain excellent agreement between the transformation $l = (n+1)k$ motivated by the influx condition and the numerical results. The dashed red line is obtained by plotting the indicator line (l, l). In both figures, the arrow is used to indicate the increase in values of α.

the y-axis $\sim (0, t^k)$. It follows that $k \leq 1/(n+2)$, and we can conclude that the no-drainage solution to (4.74) serves as an upper bound to solutions to (4.82), hence

$$h(x,t) \leq h(0,t) \lesssim t^{1/(n+2)} \quad \text{and} \quad x_f(t) \lesssim t^{(n+1)/(n+2)} \quad \forall\ \alpha \in \mathbb{R},\ n \geq 1. \tag{4.85}$$

Note that due to the bounds in (4.85), the current has to spread asymptotically as $t^{(n+1)/(n+2)}$ and grow asymptotically at the origin as $t^{1/(n+2)}$ if the volume term is of magnitude t. The spreading radius can asymptotically only be smaller, if the total drainage is of order t, which is equivalent for the drainage at a given time t to be greater than some constant asymptotically, i.e.

$$\int_0^{x_f(t)} \lambda h \, \mathrm{d}x \gtrsim c > 0. \tag{4.86}$$

To estimate the instantaneous drainage (4.86), we use the transform $\eta = x/x_f(t)$ from the fixed-interval numerics in Section 4.3.2.3 for λ,

$$\frac{\partial \lambda}{\partial t} - \frac{\dot{x}_f}{x_f}\eta\frac{\partial \lambda}{\partial \eta} = -\lambda^\alpha h. \tag{4.87}$$

Note that $\dot{x}_f/x_f \sim t^{-1}$ and for each η, $\partial\lambda/\partial\eta$ is bounded as $\lambda(\eta, 0) = 0$ and $\lambda(\eta, t) \to 0$ as $t \to \infty$ for $\eta < 1$. Therefore, using the lower bound on h in figure 4.10, we estimate λ asymptotically by solving

$$\frac{\partial \lambda}{\partial t} = -(1-\eta)\lambda^\alpha t^k, \tag{4.88}$$

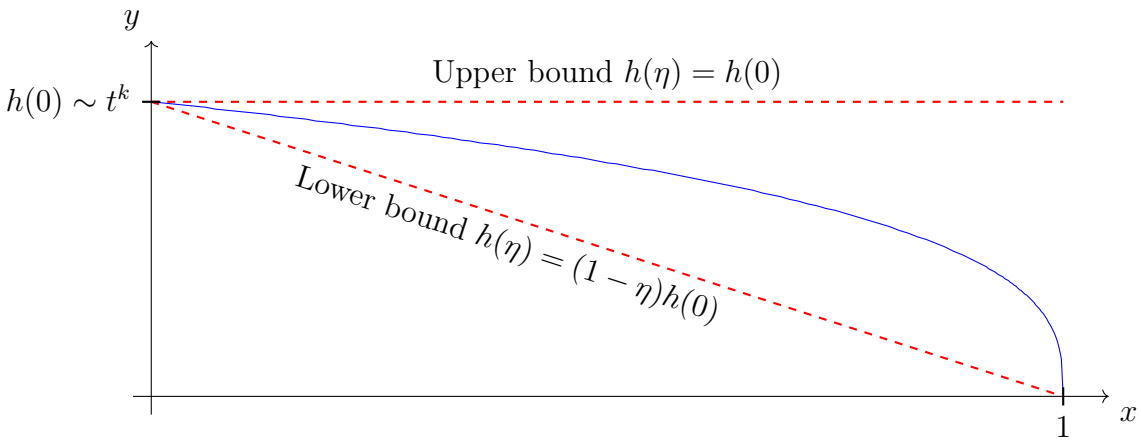

Figure 4.10: Schematic for justifying the upper bound on λ (4.88). We can use the lower bound on the height for the decrease in λ while we can use the upper bound for finding an upper bound on the drainage.

where $k \in [0, 1/(n+2)]$ is the order of height of h at $\eta = 0$. We can determine a solution to (4.88) subject to $\lambda(\eta, 0) = 1$ for $\alpha \neq 1$ as

$$\lambda(\eta, t) = \left(1 + \frac{(\alpha - 1)(1 - \eta)}{k+1} t^{k+1}\right)^{1/(1-\alpha)}, \tag{4.89}$$

and, for $\alpha = 1$,

$$\lambda(\eta, t) = \exp\left(-\frac{1-\eta}{k+1} t^{k+1}\right). \tag{4.90}$$

Note that, for $\alpha < 1$, the membrane will be blocked within a finite amount of time. For $\alpha > 1$, we can use (4.89) to obtain the asymptotic behaviour of λ as

$$\lambda(\eta, t) \sim t^{-(k+1)/(\alpha-1)}, \quad \eta < 1. \tag{4.91}$$

To estimate the drainage in (4.86), we use the upper bound on the height $h(\eta, t) \lesssim t^k$, which yields

$$D(t) = \int_0^{x_f(t)} \lambda h \, \mathrm{d}x \sim t^{-(k+1)/(\alpha-1)} t^{(n+2)k}. \tag{4.92}$$

For the drainage to be a constant, we can solve (4.92) for k or α, obtaining

$$k = \frac{1}{(n+2)\alpha - 1} \quad \text{or} \quad \alpha = \frac{n+3}{n+2} + \frac{1}{(n+2)k}. \tag{4.93}$$

We use the relation for α in (4.93) to transform the numerically obtained values for k for different n and α, the results are shown in figure 4.11.

We note that the relationship in (4.93) is only valid for $\alpha \geq 2 + 1/(n+2)$ due to the bound on the asymptotic order of the height $k = 1/(n+2)$ and the bound on the

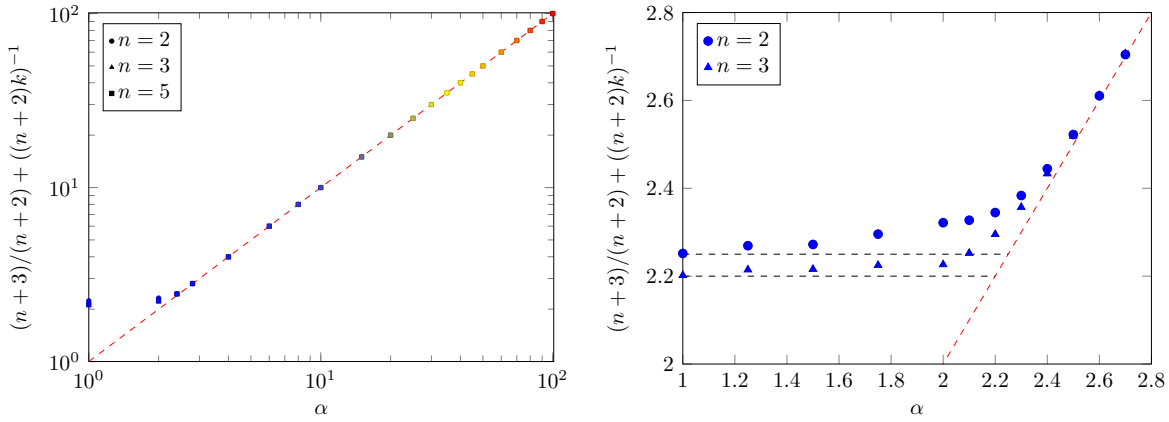

(a) (b)

Figure 4.11: (a) We plot the numerical results following the relation between α and k (4.93) for $t = 10^8$ and different values of α in the range of 1 to 100. We obtain excellent agreement between the theory and the numerical results, except for for $\alpha < 3$. In (b), we show the numerical results for different values of α in the range of 1 to 3. The dashed lines show the theoretically predicted values. The differences between the numerical values and the theoretically predicted values decrease with an increase in t, and so the remaining differences are suspected to be due to numerical limitations.

asymptotic order of the position of the front $l = (n+1)/(n+2)$. For $\alpha < 2+1/(n+2)$, the volume $V(t)$ therefore has to be of magnitude t and we predict the spreading position to follow the same power-law asymptoticially for $t \to \infty$ as in the case where there is no drainage.

The result (4.93) allows us to uniquely identify the filtration mode for $\alpha > 2 + 1/(n + 2)$. Note that we never used the assumption that $\beta = 1$, and so we expect the results to be valid for all $\beta > 0$. In the next section, we will devise a method to determine the filtration mode for $\alpha < 1$. To do so, we will show that the full model (4.67) exhibits a travelling wave solution. We will show that for $\alpha < 1$, the travelling wave will also create a no-drainage front, a position before which the fluid no longer leaks. The distance between the drainage front and the spreading front of the current will be characteristic of the filtration mode α.

4.3.3 A travelling wave solution

In this section, we show that we can find a travelling wave solution for all $\alpha \in \mathbb{R}$ to the full dimensionless problem (4.67) subject to the boundary conditions $h(x_f, t) = 0$, $(h^n h_x)(x_f, t) = 0$ and the initial conditions $h(x, 0) = 0$, $\lambda(x, 0) = 1$, provided we apply the correct influx $I(t)$ where $(h^n h_x)(0) = -I(t)$. A travelling wave solution to (4.67)

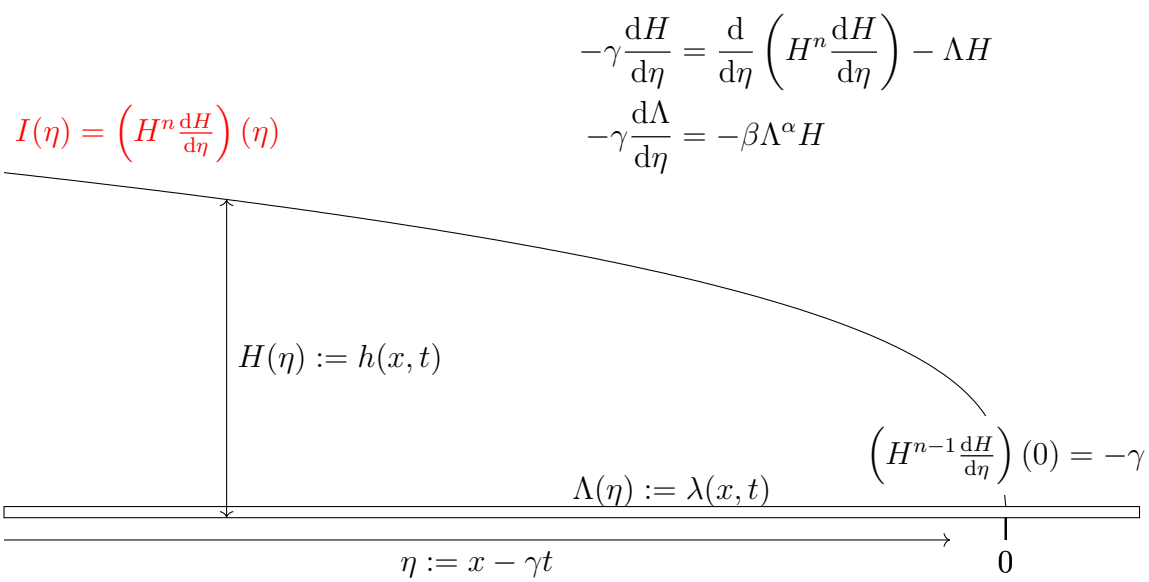

Figure 4.12: Visualisation of the modelling setup for the travelling wave solution.

takes the form

$$h(x,t) = H(x-\gamma t) \quad \text{and} \quad \lambda(x,t) = \Lambda(x-\gamma t), \tag{4.94}$$

where the *speed* $\gamma \in \mathbb{R}_+$ is a positive constant. We will show that the influx to be imposed to obtain a travelling wave solution follows a power law whose order is unique for $\alpha > 2 + 1/n$. For $\alpha < 1$, the width of the area where the current drains is only finite, creating a second *no-drainage front*. This no-drainage front will also exist for a constant influx, however, the distance between the no-drainage front and the front of the travelling wave will be constant. We will show that the distance is unique in $\alpha < 1$, providing a method to determine α in this instance. The existence of a no-drainage front resembles imbibition fronts that can be observed in the spreading of gravity currents on initially dry meshes where a capillary pressure has to be overcome (see for example Sayag and Neufeld [104]).

To show the existence of a travelling wave solution to (4.67), we use the ansatz (4.94), rescale $H = \gamma^{2/n}\hat{H}$, $\eta = \gamma\hat{\eta}$ and choose $\gamma = \beta^{-2/n}$, to obtain the system of ODEs

$$\left(\hat{H}^n H'\right)' - \Lambda\hat{H} + \hat{H}' = 0, \tag{4.95a}$$

$$\Lambda' - \Lambda^\alpha\hat{H} = 0, \tag{4.95b}$$

subject to the boundary conditions $\hat{H}(0) = 0$ and $\Lambda(0) = 1$. As for the numerical methods in Section 4.3.2.3, the speed of the front is given by taking the limit of the

flux $h^n h_x$ divided by h as $x \to x_f$, and so we obtain

$$(\hat{H}^{n-1}\hat{H}')(0) = -1. \tag{4.96}$$

Given that $\hat{H}(0) = 0$, we can immediately infer that $\hat{H}$ will not be Lipshitz continuous at the front, thus not guaranteeing existence and uniqueness. We can circumvent this problem by introducing the two variable transformations

$$\Phi = H^n \quad \text{and} \quad \xi = -\eta, \tag{4.97}$$

where the second transformation is employed to obtain a solution for positive ξ, so that we can use intuitive formulations such as "ξ large" etc. when describing the asymptotic behaviour of the solution Φ. With the transformation (4.97), we obtain the system of equations

$$\frac{1}{n}(\Phi')^2 + \Phi\Phi'' - \Phi' - n\Lambda\Phi = 0, \tag{4.98a}$$

$$\Lambda' + \Lambda^\alpha \Phi^{1/n} = 0, \tag{4.98b}$$

subject to the boundary conditions $\Lambda(0) = 1$, $\Phi(0) = 0$, and $\Phi'(0) = n$, making the problem Lipshitz continuous at 0, guaranteeing existence and uniqueness up to a potential blow-up. We also point out that we numerically solve (4.98) by using the approximation $\Phi(\epsilon) = n\epsilon + O(\epsilon^2)$ and $\Lambda = 1$ around $\xi = 0$ for small ϵ.

We will now reproduce the exact solution to the fast-clogging limit $\alpha \to -\infty$, that is, $\Lambda \equiv 0$, from [119], as this will provide a lower bound to the necessary influx for obtaining a travelling wave solution. For the slow-clogging limit $\alpha \to -\infty$, that is, $\Lambda \equiv -1$, we will propose a power law solution for large ξ, which then will be generalised for $\alpha > 1$.

4.3.3.1 Analytic solutions for the fast-clogging limit

We begin by considering the limiting case of $\alpha \to -\infty$, which we identify with $\Lambda \equiv 0$. In this instance, the set of equations (4.98) simplifies to

$$\frac{1}{n}(\Phi')^2 + \Phi\Phi'' - \Phi' = 0, \tag{4.99}$$

subject to the boundary conditions $\Phi(0) = 0$ and $\Phi'(0) = n$. We can verify by direct evaluation that

$$\Phi(\xi) = \max\{n\xi, 0\} \tag{4.100}$$

solves the equation (4.99), and the influx required to create this travelling wave solution is given by

$$I(\xi) = H(\xi)^n \frac{\partial H(\xi)}{\partial \xi} = \frac{1}{n}\Phi^{1/n}\frac{\partial \Phi}{\partial \xi} = (n\xi)^{1/n}\,. \tag{4.101}$$

We note that

$$\lim_{n\to\infty} n^{1/n} = \lim_{n\to\infty} \exp(\log(n)/n) = 1, \tag{4.102}$$

and so we obtain that, in the limit of $n \to \infty$, a constant influx is required to create a travelling wave. As expected, this agrees with two results from the previous sections, namely that, in the limit $n \to \infty$, we have $x_f(t) \propto t$ for the position of the front (equation (4.73)) and $\eta_F \to 1$ for the spreading constant (figure 4.7).

4.3.3.2 Asymptotic results for the slow-clogging limit

In the slow-clogging limit $\alpha \to \infty$, which corresponds to $\Lambda \equiv 1$, the system of equations (4.98) becomes

$$\frac{1}{n}(\Phi')^2 + \Phi\Phi'' - \Phi' - n\Phi = 0, \tag{4.103}$$

subject to the boundary conditions $\Phi(0) = 0$ and $\Phi'(0) = n$. We are not aware of a closed-form solution, but we can make progress by looking for a solution of the form $\Phi \sim \xi^k$ for large ξ. Balancing the terms in (4.103), we obtain $k = 2$ and a required influx of

$$I(\xi) \sim \frac{2}{n}\xi^{(n+2)/n}. \tag{4.104}$$

This corresponds to providing an influx of order $t^{(n+2)/n}$. We point out that for $n = 3$ the required influx of order $t^{5/3}$ is bigger than the limit $t^{3/4}$ established theoretically by Huppert [61] and experimentally confirmed by Maxworthy [84], for which we can expect a two-dimensional gravity current, albeit without considering drainage. Therefore, it is not clear whether the theoretical results will necessarily be transferable to experimental procedures.

4.3.3.3 Asymptotic results for the general case

Motivated by the power-law approach for $\Lambda \equiv 1$, we now choose the same approach for the general case where Λ is allowed to vary. We assume

$$\Phi \sim \xi^k \quad \text{and} \quad \Lambda \sim \xi^{-l} \tag{4.105}$$

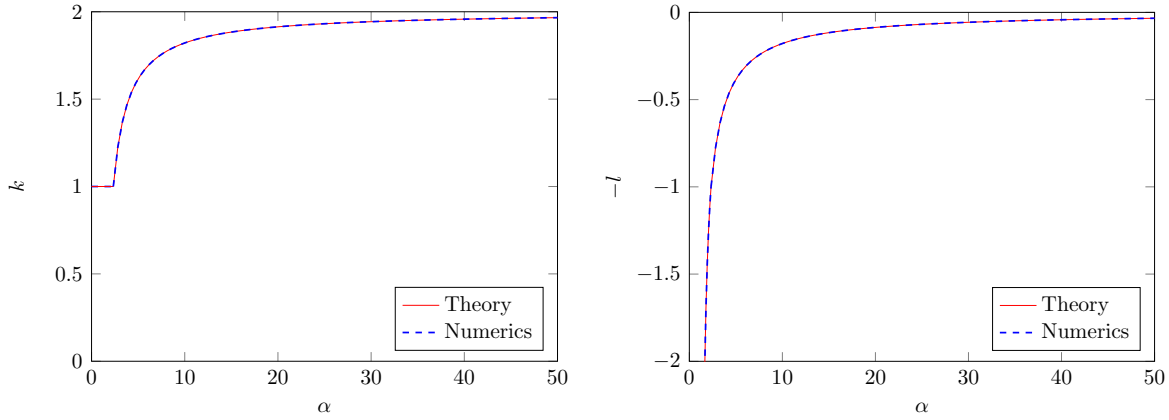

(a) (b)

Figure 4.13: Numerical validation for $N = 3$ of (4.107)–(4.110), (a) contains the results for Φ while (b) contains the results for λ. We obtain excellent agreement between the numerical results and the theoretical predictions. The change between the drainage driven scaling and the volume driven scaling occurs at $\alpha = 2+1/n$, both for k and l, although this is much more visible in (a) than in (b).

for large ξ, which corresponds to requiring an influx

$$I(\xi) \sim \xi^{((n+1)k-n)/n}. \tag{4.106}$$

From this, we see that it is sufficient to determine the power-law behaviour k of Φ to determine the leading order magnitude of the influx I. Balancing terms in (4.98), we obtain the values of k and l as

$$k = \frac{n(2\alpha - 3)}{n(\alpha - 1) + 1} \quad \text{and} \quad l = \frac{n + 2}{n(\alpha - 1) + 1}. \tag{4.107}$$

As the influx for the fast-clogging limit is of order $1/n$ (4.101) and so for any α, the influx has to be of order at least $1/n$, we can conclude from (4.106) that k has to be at least 1. Therefore, (4.107) is only valid for

$$\alpha \geq 2 + \frac{1}{n}, \tag{4.108}$$

and we automatically obtain $k = 1$ for $\alpha \leq 2 + 1/n$. We can validate this result, as we have asymptotically for $\alpha \leq 2 + 1/n$,

$$\frac{\mathrm{d}\lambda}{\mathrm{d}\xi} = -\lambda^{\alpha}\xi^{1/n}, \tag{4.109}$$

which has the solution

$$\lambda = \left(1 + \frac{\alpha - 1}{n + 1}\xi^{(n+1)/n}\right)^{1/(1-\alpha)} \tag{4.110}$$

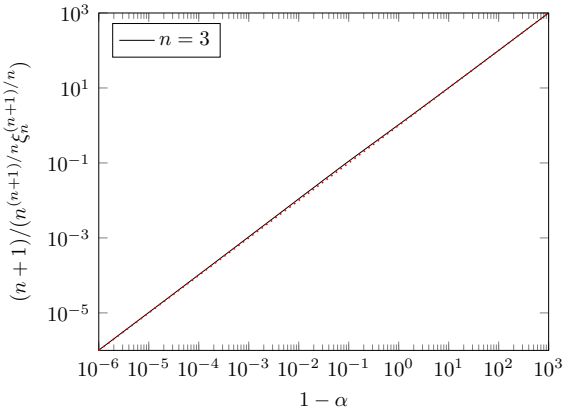

(a)

Figure 4.14: Comparison between the exact numerical solution to (4.111) and the approximation (4.113). Due to the excellent agreement, we can therefore use (4.113) to obtain a good estimate for α.

and we have $\lambda \sim \xi^{-1}$ for $\alpha = 2 + 1/n$. Hence, we know that the integral of $\lambda(\xi)$ from 0 to ∞ diverges for $\alpha = 2 + 1/n$ but converges for $\alpha < 2 + 1/n$. We show the excellent agreement between the numerical results and our theoretical predictions for $n = 3$ in figure 4.13, we obtain similar accuracy for the other values of n we tested (all integers in the range 1 to 100).

4.3.3.4 Computing the width of the drainage front for $\alpha < 1$

From the asymptotic solution (4.110), we can conclude that for $\alpha < 1$ we obtain $\lambda = 0$ for finite ξ. Therefore, we could aim to observe the position of the no-drainage front and determine α from the width of the region where the current drains. To do so, we note that for $\alpha < 1$ it is advisable to use the transformation $\Psi = \Lambda^{1-\alpha}$, which transforms (4.98) into the numerically more tractable

$$\frac{1}{n}(\Phi')^2 + \Phi\Phi'' - \Phi' - n\Psi^{1/(1-\alpha)}\Phi = 0, \tag{4.111a}$$

$$\Psi' + (1-\alpha)\Phi^{1/n} = 0, \tag{4.111b}$$

subject to the boundary conditions $\Psi(0) = 1$, $\Phi(0) = 0$, and $\Phi'(0) = n$, and use a root-finding method to determine the position of the no-drainage front ξ_n. We can find an approximation to ξ_n by using the solution $\Phi = n\xi$ for $\alpha \to -\infty$, which we expect will be a good approximation to the numerical solution. Then, we have that

$$\lambda = \left(1 + \frac{n^{(n+1)/n}(\alpha-1)}{n+1}\xi^{(n+1)/n}\right)^{1/(1-\alpha)}, \tag{4.112}$$

which we can solve for $\lambda = 0$ to obtain the no-drainage front ξ_n as

$$\xi_n = \left(\frac{n+1}{n^{(n+1)/n}(1-\alpha)} \right)^{n/(n+1)} . \tag{4.113}$$

We show the excellent agreement between the approximation (4.113) and the exact solution in figure 4.14. This result allows us to determine the filtration law for $\alpha < 1$ from the distance between the front and the no-drainage front.

4.3.4 Summary

In this section, we have introduced a variant of the generalised porous medium equation with absorption, where the reduction of the permeability factor λ governing the strength of the absorption follows a generalisation of the four blocking laws. This theoretical model is a generalisation of the work of the first section of this chapter, as we now allowed continuous filtration laws and considered a range of exponents in the porous medium equation.

We showed different approaches for determining the filtration mode α from the spreading speed of a gravity current. First, we showed that the long-term spreading speed is unique for $\alpha > 2 + 1/(n+2)$. Then, we showed that our model exhibits a travelling wave solution and that the influx necessary to generate the travelling wave is unique for $\alpha > 2 + 1/n$. We also used the theory to estimate the width of the drainage region for filtration modes $\alpha < 1$.

4.4 Conclusion

The overarching goal of this section was to investigate whether one can determine a filtration law from the spreading speed of a gravity current. The answer to this question is a partial yes. We showed that we can model the axisymmetric spreading of a particle-laden gravity current on a porous mesh by a combination of the classical gravity current theory and the theory developed in Chapter 3. Similarly, we showed that there are ways to determine the filtration mode α in the more general model of the porous medium equation with drainage and a generalisation of blocking laws.

Regarding the first section, we note that, despite the good agreement, there is a certain mismatch between our model and the experiments. For example, we observe particles accumulating at the front, which is a well-known phenomenon for particle-laden thin films [28] that is not accounted for in our model. During the experiments, we also observe no particles depositing close to the inlet, presumably due to shear

forces. However, our model assumes that particles will not move once they have touched the mesh. The resolution to this problem is twofold. First, it would be interesting to employ the theory of granular flows for a different modelling of the experiments. Second, it would be worthwhile to conduct experiments where particles do not move once they are retained by the mesh.

Regarding the second, more theoretical section, an obvious next question will be to find ways to determine α when $\alpha \in [1, 2 + 1/n]$. The asymptotic results relied on numerical evidence, and so it will be important to formally prove these results to gain certainty about the asymptotic behaviour. Going forward, it will also be interesting to allow for more general filtration laws of the form

$$\frac{\partial \lambda}{\partial t} = -f(\lambda)h, \tag{4.114}$$

with f, as in our case, motivated by a given application.

Chapter 5

Scaling-up of multi-capsule depth filtration systems by modelling flow and pressure distribution

5.1 Introduction

The central theme of this penultimate chapter is how we can combine empirical data with a theoretical model derived from first principles to accurately model industrial-sized filtration operations. Note that empirical data has always played an important role in a variety of constitutive laws to include information which is hard to compute from first principles, see for example the Lamé constants [59]. The inclusion of empirical data is not restricted to low-dimensional parameters as in the case of the Lamé constants, however. With an increase in computing power and an abundance of empirical data from measurements or high-fidelity direct numerical simulations, new ways of combining high-dimensional data with theoretical models are being explored [23, 81, 122]. As an example for this approach, we will combine flux–throughput data from laboratory-scale experiments with simple fluid mechanics to accurately model a filtration run of an industrial-sized multi-capsule depth filter, providing a novel method for scaling-up filtration processes.

Scaling-up of filtration processes from R&D to production level in the pharmaceutical industry is a complex undertaking with strong implications on the profitability of the corresponding drug development project [11, 24]. A key challenge lies in providing the appropriate filtration capacity for production-level batch sizes based on laboratory or testing-plant scale measurements [77]. This can, for example, be achieved by using dimensional analysis to scale-up filters used in the laboratory-scale process [127] or by using several filters of standardised size in parallel, for example in multi-capsule

depth filters [27].

Depth filtration is typically operated in dead-end configuration and differs from membrane filtration in that the filtered particles are predominantly retained within the entire depth of the filter and not only at the surface [101]. In the pharmaceutical industry, depth filtration is typically used to clarify process streams before a final sterile filtration [25, 117]. In order to process the feed from industrial-sized bioreactors (> 2000 L), a depth filter with a sufficiently large surface area is required, which is in general achieved by using several depth filters of some standardised size in parallel [118]. Typical depth filters are housed in disc-shaped capsules, which in turn are then connected in parallel and stacked horizontally on top of each other, principally to reduce the footprint of the filtration system, though other operational considerations may also play a role. It is such a stack of depth-filter capsules that we refer to as a *multi-capsule depth filter*.

The inlet to the multi-capsule depth filter is usually located at the bottom of the device, while the outlet can be positioned either at the bottom or the top. If the outlet is located at the bottom, the feed flows upwards while the filtrate flows downwards, hence it is called a *counter-current* configuration. If the outlet is located at the top, both the filtrate and feed flow upwards and it is called a *co-current* configuration.

If the depth filters in the capsules are identical, then the pressure differences across the capsules will not be equal, otherwise there would be no flow from one capsule inlet to the next one. Consequently, the different depth filters will clog up at different rates, which leads to a change in the pressure distribution within the system, which in turn leads to a change in the rates at which the filters clog up and so forth. To make accurate predictions about a scaled-up system, it is necessary to predict the pressure distribution within a given system of parallel filters for an entire filtration run, which must include the impact of clogging on the permeability of the individual filters. One option is to model the experimental data of the clogging of the filter using standard filtration laws, this approach has been employed in the scaling-up of a single filter from lab to industrial scale [99]. In this chapter, we introduce a more accurate approach that incorporates the experimental data directly into the theoretical model of the underlying fluid mechanics of the filtration system.

In Section 5.2, we will state the system of linear equations that describes the pressure distribution within a multi-capsule depth filter. We will then discuss how to incorporate experimental data and introduce the corresponding numerical method for predicting the pressure and flow distribution within a multi-capsule depth filter during a filtration run. In Section 5.3, we will validate the theoretical model for

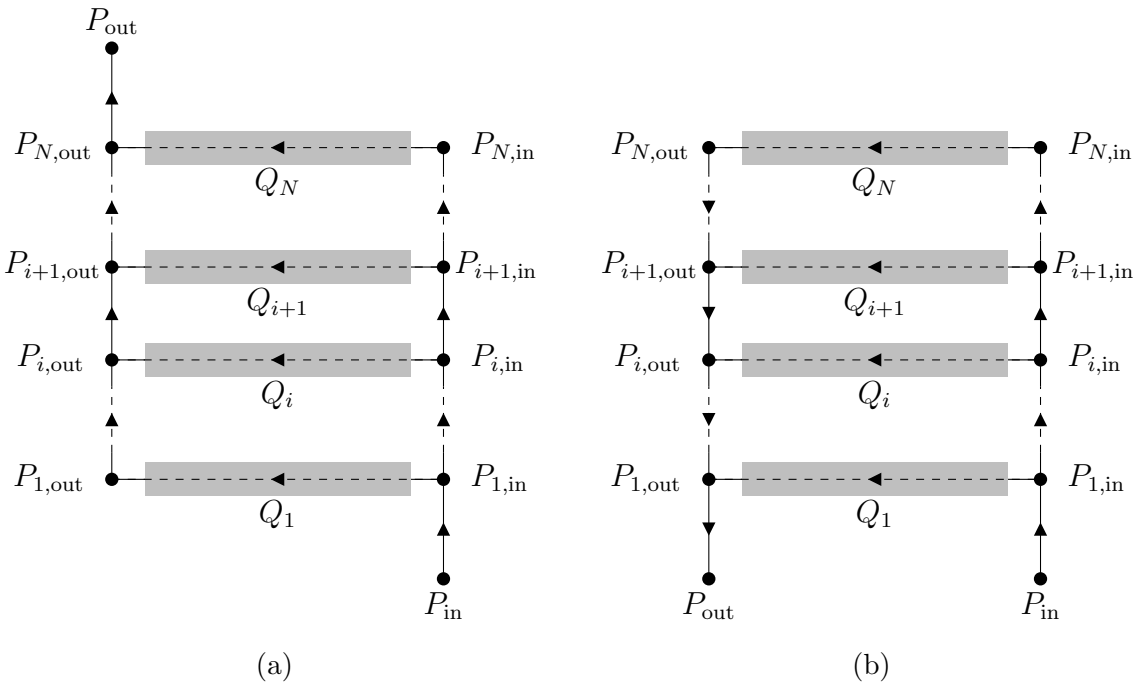

Figure 5.1: Schematic of a multi-capsule depth filter in (a) co-current and (b) counter-current configuration. Each capsule is represented by a horizontal line, with the shaded rectangles representing the depth filters. The fluid enters the device at the inlet, marked by P_{in}, and leaves it at the outlet, marked by P_{out}.

the pressure distribution against experimental measurements conducted in [27]. In Section 5.4, we show the excellent agreement between our predictions and the experimental measurements for an entire filtration run. Given that full-scale experiments on multi-capsule depth filters are very costly, we discuss how to use our faster and cheaper hybrid approach for different scaling-up problems in Section 5.5. The findings of this chapter have been published in [73].

5.2 Mathematical model

We consider schematic setups for the co-current and counter-current configuration with N capsules as in figure 5.1. The inlets and outlets of the capsules are connected in series, hence at a given inlet the fluid can either pass through the depth filter or move to the next capsule. Once the fluid has passed through a filter, it flows through the connecting pipes to the outlet of the entire device.

The pressure at the inlet is denoted by P_{in} and at the outlet by P_{out}. For capsule i, $1 \leq i \leq N$, we denote the pressure at the inlet by $P_{i,\text{in}}$ and at the outlet by $P_{i,\text{out}}$.

The flux through capsule i is denoted by Q_i, and the total flux through the system by $\mathcal{Q}$. We denote the head difference of capsule i relative to the inlet by h_i.

5.2.1 Constitutive relationships between fluid flow and pressure differences

We assume that the pressure in the system is composed of a hydrostatic and hydrodynamic part only. The inlet and outlet pressures $P_{i,\text{in}}$ and $P_{i,\text{out}}$ can be reduced to their hydrodynamic part only by setting

$$\tilde{P}_{i,\text{in}} = P_{i,\text{in}} - \rho g h_i \quad \text{and} \quad \tilde{P}_{i,\text{out}} = P_{i,\text{out}} - \rho g h_i, \tag{5.1}$$

where ρ denotes the density of the liquid and g the gravitational acceleration. In the following, we need only work with the hydrodynamic pressures, $\tilde{P}$, even if the capsules are stacked on top of each other or are located at different heights; we will drop the tilde in order to facilitate reading.

For practical filter operating regimes, the constitutive relation between the pressure difference, $\Delta P_i := P_{i,\text{in}} - P_{i,\text{out}}$, across and the flux Q_i through the ith filter is approximated well by Darcy's law

$$Q_i = \frac{k_i A_i}{\mu L_i} \Delta P_i, \tag{5.2}$$

where A_i denotes the surface area, k_i the permeability and L_i the depth of the filter, and μ denotes the dynamic viscosity of the liquid. We will abbreviate (5.2) by $Q_i = \kappa_i \Delta P_i$, where $\kappa_i = k_i A_i / \mu L_i$ is the *conductivity* of depth filter i. We expect the conductivity of the filter to decrease due to clogging. While the conductivity of the individual interconnected pores of the filter does not equal the conductivity of the entire filter (see Chapter 3), it is sufficient for our purposes to only consider the conductivity of the entire filter.

We assume laminar flow in the connecting pipes between two capsules as the relevant Reynolds number for the flow is of order 10^{-1} (using data[1]). For a straight pipe of uniform radius R and length L, the flux Q_P through the pipe is given by integrating the Poiseuille flow velocity profile across the cross-sectional area to obtain

$$Q_P = \int_0^R \int_0^{2\pi} \frac{\Delta P_P}{4\mu L} (R^2 - r^2) r \, \mathrm{d}\theta \, \mathrm{d}r = \frac{\pi R^4}{8\mu L} \Delta P_P, \tag{5.3}$$

[1]The kinematic viscosity ν is $\nu \approx 10^{-6} m^2/s$, the length scale between the filter and the filter capsule is of order $10^{-2} m$, the velocity is of order $10^{-3} m/s$ and the aspect ratio for the length is of order 10^{-2}.

where ΔP_P denotes the pressure difference applied across the pipe. For the potentially non-straight pipes connecting the different capsules, we therefore use a constitutive relation of the form

$$Q = r\Delta P \tag{5.4}$$

to determine the flux Q through the pipe for an applied pressure difference ΔP, where the constant conductivity r only depends on characteristics of the connecting pipes. We will denote the conductivity r of the connecting pipes between capsule i and $i+1$ by $r_{i,\text{in}}$ at the inlet and by $r_{i,\text{out}}$ at the outlet. The resistance between the inlet and the first capsule is denoted by r_{in} and the resistance between the outlet and the connecting capsule by r_{out}.

From an operational perspective, we require that the fluid occupies the entire device so that the fluid does not cavitate. Hence the pressures at the inlet and outlet must equal at least the hydrostatic pressure of the fluid in the device. For both setups we therefore require

$$P_{\text{in}} \geq \rho g \cdot \max\{h_1, \ldots, h_N\} \tag{5.5}$$

and for the counter-current configuration, we also require the same inequality to hold for P_{out}.

5.2.2 Derivation of the system of linear equations describing the pressure distribution and fluid flow within the multi-capsule depth filter

Darcy's law (5.2) and the Poiseuille relation (5.4) can be combined to form a system of linear equations for the inlet and outlet pressures $P_{i,\text{in}}$ and $P_{i,\text{out}}$, $1 \leq i \leq N$. This is similar to computing the pressure distribution within an interconnected membrane as in Chapter 3, we will state the equations in this section for completeness. The governing equations for the inlets of the capsules are given for $i = 1, \ldots, N-1$ by

$$r_{i,\text{in}} \left(P_{i,\text{in}} - P_{i+1,\text{in}}\right) = \sum_{l=i+1}^{N} Q_l \tag{5.6}$$

and

$$r_{\text{in}} \left(P_{\text{in}} - P_{1,\text{in}}\right) = \mathcal{Q} \tag{5.7}$$

for the inlet of the device.

Regarding the governing equations for the outlets of the capsules, we must distinguish between co-current and counter-current configuration. In the co-current

configuration we have for $i = 1, \ldots, N-1$

$$r_{i,\text{out}} \left(P_{i,\text{out}} - P_{i+1,\text{out}} \right) = \sum_{l=1}^{i} Q_l \tag{5.8}$$

and

$$r_{\text{out}} \left(P_{N,\text{out}} - P_{\text{out}} \right) = \mathcal{Q} \tag{5.9}$$

at the outlet. For the counter-current configuration we have for $i = 1, \ldots, N-1$

$$r_{i,\text{out}} \left(P_{i+1,\text{out}} - P_{i,\text{out}} \right) = \sum_{l=i+1}^{N} Q_l \tag{5.10}$$

and

$$r_{\text{out}} \left(P_{1,\text{out}} - P_{\text{out}} \right) = \mathcal{Q} \tag{5.11}$$

at the outlet. Darcy's law (5.2) reads as

$$\kappa_i \left(P_{i,\text{in}} - P_{i,\text{out}} \right) = Q_i \tag{5.12}$$

for $i = 1, \ldots, N$ and we have conservation of flux

$$\sum_{i=1}^{N} Q_i = \mathcal{Q}. \tag{5.13}$$

We can use (5.12) to replace each Q_i in the set of equations (5.6)–(5.11), to give $2N$ equations for $2N + 2$ unknowns. Specifying two of the three parameters P_{out}, P_{in} or $\mathcal{Q}$ via a combination of equations (5.12) and (5.13) results in a linear system with $2N$ equations for $2N$ unknowns for which a unique solution exists, see Chapter 3 for details.

5.2.3 Simulating an entire filtration run

During a filtration run, fouling will change the permeability of the capsules. Given that the flow distribution is in general non-uniform within a multi-capsule depth filter, the permeabilities of the different capsules will decrease at different rates during the filtration run, which in return changes the flow and pressure distribution. To model this evolution over time, we assume that the permeability k_i of capsule i, and thus its conductivity κ_i, at a given time t depend only on the throughput V_i^t, that is, the total volume of fluid processed by capsule i up to time t, and that this relationship is sufficiently smooth.

To simulate the filtration run, we use an explicit Euler-scheme with constant (small) timestep Δt. At each time t, we compute the pressure distribution by solving the linear system described by equations (5.6) –(5.11) with corresponding conductivities $\kappa_1^t, \ldots, \kappa_N^t$. The total throughput $V_i^{t+\Delta t}$ through capsule i at time $t+\Delta t$ is then computed by

$$V_i^{t+\Delta t} = V_i^t + \Delta t \; \kappa_i^t \; (P_{i,\text{out}} - P_{i,\text{in}}) \,. \tag{5.14}$$

The conductivity of capsule i at time $t+\Delta t$, $\kappa_i^{t+\Delta t}$, can then be computed by

$$\kappa_i^{t+\Delta t} = \kappa(V_i^{t+\Delta t}), \tag{5.15}$$

where the κ–V relationship is given either by some function in closed form or using experimental data as described in Section 5.3.2.1. We repeat the entire process until some final condition, for example, $P_{\text{in}} - P_{\text{out}}$ exceeds some threshold value, is satisfied.

5.2.4 Least-squares fitting for computing experimental parameters

To compare the results of our simulations with the measurements from a filtration run, the initial conductivities of the membranes and the conductivities of the pipes have to be determined. The capsules in the multi-capsule depth filter are identical, the connecting pipes therefore have the same geometry, and so we will work with the assumption that the initial conductivities of the membranes and the conductivities of the pipes are the same. Hence, $\kappa_1 = \ldots = \kappa_N$, $r_{1,\text{in}} = \ldots = r_{N-1,\text{in}}$, and $r_{1,\text{out}} = \ldots = r_{N-1,\text{out}}$. In order to compute the values, we define the vector-valued function

$$\mathbf{F}(\kappa, r_{\text{in}}, r_{\text{out}}) = (\mathbf{P}_{\text{in}}, \mathbf{P}_{\text{out}}), \tag{5.16}$$

where the vectors $\mathbf{P}_{\text{in}}, \mathbf{P}_{\text{out}}$ are the solutions to the linear system arising from equations (5.6)–(5.13), as described in Section 5.2.2, subject to the inlet and outlet pressures being given. We also define Q as the flux through the system based on $\mathbf{P}_{\text{in}}, \mathbf{P}_{\text{out}}$ and κ being known. Let $\mathbf{M}$ denote the vector containing the measurements from the experiments. We then compute the parameters by minimising the functional

$$G := \|\mathbf{F} - \mathbf{M}\|^2 + |Q - Q_0|^2 \tag{5.17}$$

using nonlinear least-squares approximation. To uniquely define the solution of the minimisation problem, we additionally provide some reference flux Q_0.

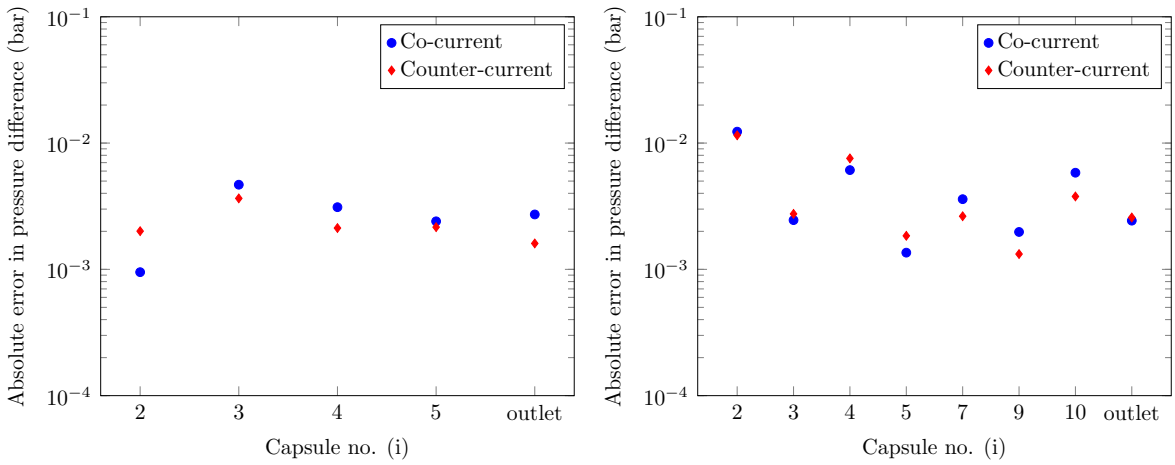

Figure 5.2: Validating the model (5.6)–(5.11). We plot the average error between the predicted and measured pressure taken from Collins et al. [27] at each capsule for a (a) five-capsule depth filter and a (b) ten-capsule depth filter based on clean-water flow tests with $100, 200$ and 300 litres per square metre per hour (LMH). We display the absolute error as the measured pressures are all around 1 bar.

5.3 Validation of the mathematical model

In this section, we validate our theory by comparing the predictions of our mathematical model with measurements taken by Collins et al. [27]. Here, clean-water flow tests that do not change the permeability were first conducted to measure the flow and pressure distribution within a multi-capsule depth filter. Following this, full filtration runs with dissolved yeast were conducted to simulate a filtration run with a mammalian cell culture.

5.3.1 Comparison with clean-water flow tests

In a clean-water flow test, water is supplied at a constant flux as a feed, thus no clogging occurs and so the flow and pressure distribution are constant (after a short start-up transition). In the first set of experiments in [27], clean-water flow tests were conducted with multi-capsule depth filters with five and ten capsules, each in co-current and counter-current configuration. Regarding the experiments with five capsules, the authors measured the pressure at the inlet side of the filters of each capsule and the outlet side of capsules 1 and 5. For the experiments with ten capsules, the authors measured the pressure at the inlet side of the filters 1–$5, 7, 9, 10$ and the outlet side of capsules 1 and 10. The measurements in each experiment were taken

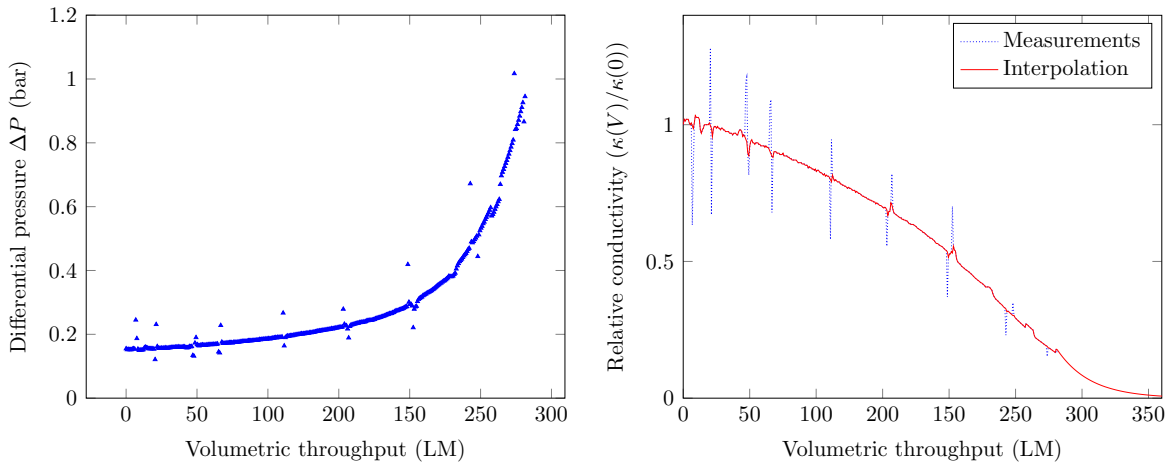

(a) (b)

Figure 5.3: In (a), we plot the measured differential pressure applied across a single capsule when challenged with a homogenised/whole-yeast mixture at 300 LMH, the data is taken from Collins et al. [27]. These measurements are used to obtain the relative conductivity in dependence of the throughput, the results are shown in (b). As the data contains outliers due to resets of the pump, we apply a smoothing method and extend the interpolated function by assuming an exponential decay law.

for fluxes of 100, 200 and 300 litres per square metre per hour (LMH).

These experimental values were used to determine the parameters κ, r_{in}, and r_{out} by assuming the values were the same for each capsule as described in 5.2.4. The results for the co-current and counter-current configuration with five capsules are shown in figure 5.2a and the corresponding results for ten capsules are shown in figure 5.2b. As the measured pressures were all around 1 bar, we plot the absolute errors in pressure between the measurements and our predictions. In the figures, the absolute error for the outlet represents the absolute error between the prediction and the measurement for the outlet of the bottom capsule (co-current configuration) or for the outlet of the top capsule (counter-current configuration). We do not plot the error for capsule 1 and the outlet of the system, as their values were used as boundary conditions.

The model accurately fits the data with absolute and relative errors being generally in the range of 10^{-3} to 10^{-2} bar.

5.3.2 Comparison with an entire filtration run

In the second set of the experiments, two ten-capsule depth filters, one in co-current and one in counter-current configuration, were challenged with a mixture of ho-

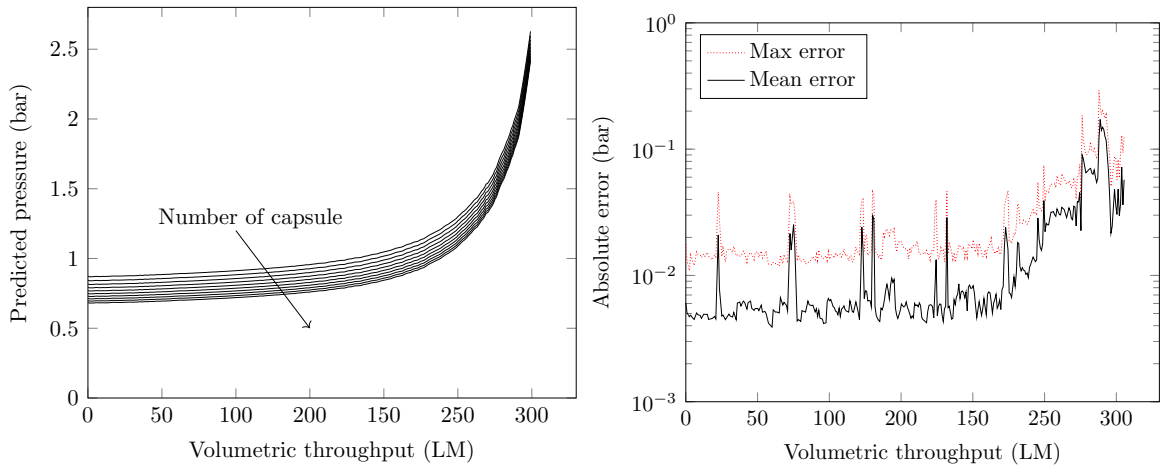

(a) (b)

Figure 5.4: (a) We plot the prediction of the pressures at the measuring points for a ten-capsule depth filter in counter-current configuration. The maximum absolute and the mean error between the predictions and the measurements are shown in (b).

mogenised yeast and whole yeast at 300 LMH until a threshold pressure was attained, in order to simulate a filtration run with a mammalian cell culture. In this instance, we expect the depth filters to clog at different rates due to the difference in fluxes and thus for their permeablities to change at different rates as well, which in turn changes the pressure distribution within the multi-capsule depth filter.

In order to precisely predict the pressure distribution within the multi-capsule depth filter during the filtration run, we have to quantify how the conductivity κ changes with throughput V. We first discuss how to obtain the κ–V relationship and then use this to compare our predictions against the measurements.

5.3.2.1 Computing change in permeability due to clogging

To obtain experimental data on the change in permeability due to clogging, a single capsule was challenged with the same mixture of homogenised yeast and whole yeast used for the filtration run at 300 LMH while the differential pressure $\Delta P(V)$ across the capsule, depending on the throughput V, was recorded, see figure 5.3a.

As we assume that the permeability k of a capsule only depends on the throughput V, i.e. $k = k(V)$, we use Darcy's law (5.2) to infer

$$\kappa(V) = \frac{Q}{\Delta P(V)}, \tag{5.18}$$

where $\kappa(V) = -k(V)A/\mu L$ is the conductivity of the filter.

The recorded ΔP–V data for an experiment at constant flux can thus be used to determine $\kappa(V)$, the result for the relative conductivity $\kappa(V)/\kappa(0)$ is shown in figure 5.3b.

As the measurements contain outliers, we apply a smoothing method where we require consecutive measurements to deviate by at most ten percent. This smoothing is depicted by the line in figure 5.3b; the experimental results are depicted by dots. As the measurements were stopped once the threshold differential pressure of 1 bar was surpassed, we extended the function by assuming an exponential decay law. We can use the resulting κ–V relationship as a function in numerical methods by linearly interpolating between consecutive measurements.

5.3.2.2 Comparison of predictions and measurements

We combined our model with the clogging model described in Section 5.3.2.1 and compared our predicted results for the pressures with those measured at the inlet of the capsules 1–5, 7–10, and at the outlet of the top and bottom capsule, both for the co-current and counter-current configuration. In order to assess the quality of our predictions, we plot for a given throughput the maximum absolute error, that is, the maximum absolute error between any of the predicted and measured pressures and the mean error. This is defined as the mean over all absolute errors between the predicted and measured pressures and is very similar to the median error.

The results of the simulation for the counter-current configuration are depicted in figure 5.4. The predicted pressure rises gradually at the beginning before rising rapidly towards the end. The model accurately predicts the measured pressures, the spikes in the error measurements are due to the spikes in the clogging data (figure 5.3a).

The results for the co-current configuration (figure 5.5) show a similar gradual rise at the beginning before the rapid rise at the end; the maximum and mean error for the predictions are better than those for the counter-current configuration.

5.4 Insights and predictions from the model

In this section, we will show that our model can be used to obtain insights about the flow distribution within a multi-capsule depth filter during a filtration run and how the performance of such a multi-capsule depth filter can be predicted using data from only a few experiments.

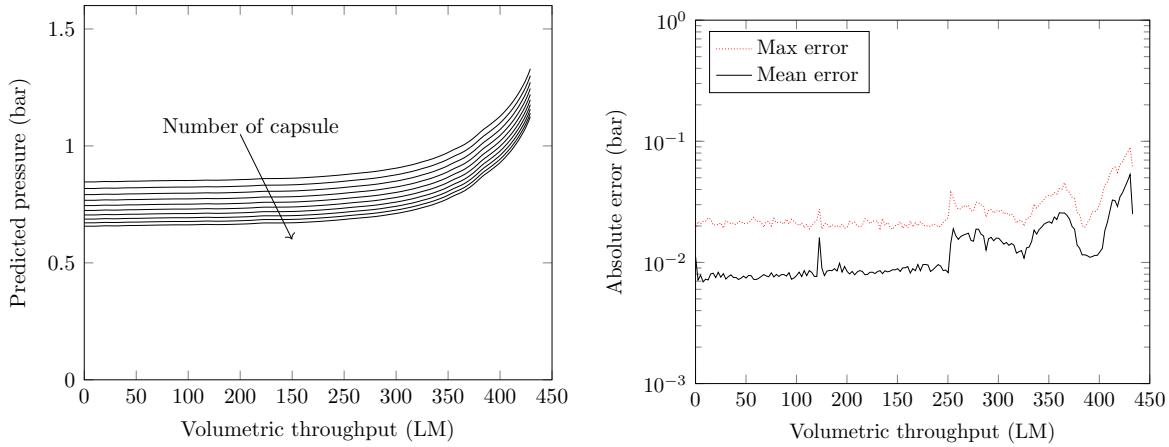

(a) (b)

Figure 5.5: (a) We plot the prediction of the pressures at the measuring points for a ten-capsule depth filter in co-current configuration. The maximum absolute and the mean error between the predictions and the measurements are shown in (b).

5.4.1 Calculating the normalised differential pressure

An important concept for multi-capsule depth filters is the normalised differential pressure (NDP), which is computed by dividing the pressure difference across a given capsule by the pressure difference across the first capsule from the bottom. In the case where the permeability of each capsule is the same, it indicates the volume of fluid that is processed by each capsule relative to the first capsule. An NDP close to 1 for all capsules is desirable, signifying a homogeneous usage of the processing capacity.

To compute the NDP, Collins et al. [27] used a linear interpolation between the pressure at the bottom and top outlet of the stack in order to estimate the pressure at the outlet of the other capsules. Thus their calculated values of the NDP differ from the NDP we obtain based on our model, as can be seen in figure 5.6.

Since the pressure differences between the outlets are uniform, the linear interpolation tends to overestimate the NDP for capsules further up in the stack.

5.4.2 Predicting the NDP for a multi-capsule depth filter with an arbitrary number of capsules

The predicted NDP in our mathematical model depends only on the parameters for the pressure loss due to friction in the pipe, $r_{i,\text{in}}$, $r_{i,\text{out}}$, and the conductivities κ_i of the capsules. If the same capsules are used within the stack, we need only the three parameters $r_{\text{in}}, r_{\text{out}}$ and κ to predict the pressure distribution within a multi-capsule

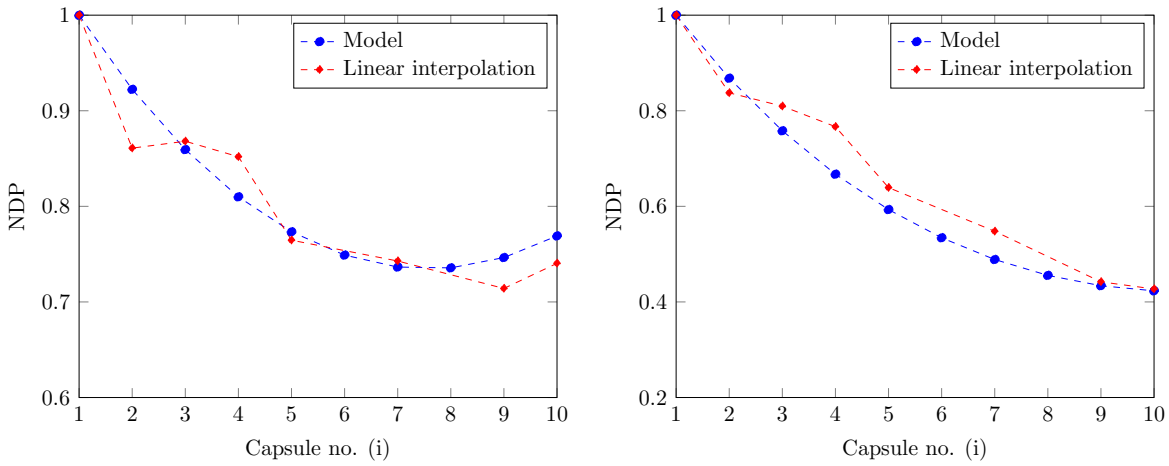

Figure 5.6: Comparison of the predicted normalised differential pressure (NDP) based on a linear interpolation and model (5.6) –(5.11) for ten capsules in (a) co-current and (b) counter-current configuration. Note the difference in scalings on the y-axis.

depth filter of any given number of capsules. Furthermore, if we know the clogging behaviour of a single capsule, we can also predict the performance of a multi-capsule depth filter during an entire filtration run with high accuracy.

As a strategy to precisely predict the filtration capacity of a multi-capsule depth filter, one would conduct clean water flow tests with a multi-capsule depth filter with two capsules to obtain the parameters $r_{\text{in}}, r_{\text{out}}$, and κ. To account for the difference in viscosity between the feed used in the experiment and water, the parameters $r_{\text{in}}, r_{\text{out}}$, and κ would have to be multiplied by the ratio of the water viscosity and the feed viscosity, $\mu_{\text{water}}/\mu_{\text{feed}}$. Finally, one can account for modelling the change in permeability due to clogging as described in section 5.3.2.1.

To illustrate the idea of predicting the capacity of a multi-capsule depth filter based on the parameters $r_{\text{in}}, r_{\text{out}}$, and κ, we used the values obtained by the measurements for the five-capsule depth filters to predict the NDP for ten-capsule depth filters. The results for the co-current and counter-current configuration are shown in figure 5.7 and show a very good agreement.

5.5 Conclusion

In this chapter, we derived a system of linear equations describing the flow and pressure distribution within a multi-capsule depth filter based on Darcy's law and the assumption of laminar flow. The corresponding system is dependent on three

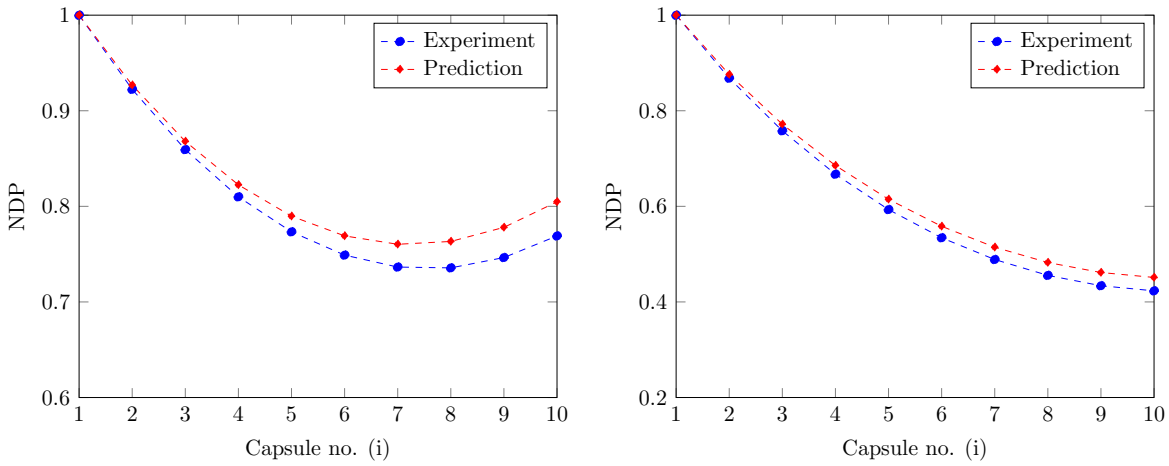

Figure 5.7: Comparison of the inferred normalised differential pressure (NDP) based on the experiments for a ten-capsule (a) co-current and (b) counter-current depth filter against the predicted NDP based on the experiments of the corresponding five-capsule depth filters. Note the difference in scalings on the y-axis.

parameters, the conductivities of the filter and the resistance in the pipes before and after the filter, which can be inferred from a clean-water flow test in any given multi-capsule depth filter and can then be used to predict the flow and pressure distribution for multi-capsule depth filters with any given number of capsules in a clean-water flow test. The predictions presented in this chapter are in good accordance with experimental data.

We then combined this model with fouling data from experiments to derive a numerical method that simulates an entire filtration run. Again, the predictions were in good accordance with the experimental data.

The methods outlined in this chapter can be applied to a wide range of scaling-up problems in dead-end filtration systems where filters are used in parallel but can also be extended to cope with filters being connected in series. The method of combining experimental measurements with a model can also be adapted to any filtration system with multiple connected filters to describe their performance during an entire filtration run, provided the key assumption, that the permeability of a given capsule only depends on its throughput, is satisfied. This method has the advantage of delivering highly accurate results while freeing the experimentalist of having to approximate the observed clogging behaviour using models.

Chapter 6

Conclusion and future work

6.1 Conclusions

In this thesis, we have studied the problem of membrane filtration from four different angles.

In Chapter 2, we revisited the theory of compressible cake filtration to understand why the conventional law for cake filtration is appropriate for most engineering applications. Based on the asymptotic analysis of the constant-pressure filtration problem, we showed that the quasi-static caking model is a suitable model for the physically relevant concentration regimes. While the conventional and quasi-static caking models behave qualitatively similar for constant-pressure filtration, we showed that the difference between the models should surface qualitatively in constant-flow-rate filtration settings, albeit for applied pressure gradients that are far greater than those applied during typical filtration operations. This chapter illustrates how the analysis of a more realistic but also more complicated model can help to understand when and why a simplified model can be sufficient.

In Chapter 3, we modelled filtration as a stochastic process by accounting for the quantised nature of the particles. We showed that the observed decline in flux during a constant-pressure filtration is in fact the outcome of a stochastic process, but treating it as a deterministic process is justified, because the difference between the measurement and the expected outcome of the stochastic process is very small for typical membranes. The concept of membrane filtration as a stochastic process was then formalised to multi-particle feeds as well as interconnected membranes, and we showed that the ideas can also be used to efficiently compute filtration coefficients.

In Chapter 4, we considered the problem of inferring the underlying filtration law from the spreading of a particle-laden gravity current on a membrane. In the first half of the chapter, we combined the theory derived in Chapter 3 with the

classical theory of gravity currents to model the experiments conducted by Box [22]. Using a parameter sweep with least-squares approximation, we showed that it is possible to identify the filtration law in this instance. In the second half of the chapter, we generalised the inverse problem by considering a variant of the porous medium equation with absorption based on a generalisation of the conventional fouling laws. We showed that the spreading speed of a solution is asymptotically unique for filtration modes $\alpha > 2 + 1/(n+2)$. For filtration modes $\alpha < 1$, we showed that the distance between the front and the imbibition front uniquely determines the filtration law and we provided a good approximation analytically.

In Chapter 5, we introduced a method for the scaling-up of a multi-capsule depth filters by combining simple fluid mechanics with experimental measurements of the underlying filtration. We demonstrated that our model provides additional insights into the performance of a multi-capsule depth filter and accurately predicts the behaviour during a filtration run. We then discussed how the proposed method can be generalised to a wide-range of scaling-up problems for depth filters.

6.2 Outlook and future work

Membrane filtration as a scientific discipline is not a young one by most standards, given that the conventional filtration laws have been known since at least 1936 [49]. Nevertheless, there is still a vast range of open problems and opportunities to improve upon existing knowledges. This is in no small part due to the fact that the problems underlying membrane filtration allow for a variety of (mathematical) approaches, as we have hoped to show in this thesis. The following brief review is therefore by no means anywhere near exhaustive with regards to future research avenues in membrane filtration, but rather hopes to provide specific extensions to the work discussed in this thesis.

Despite the relative maturity of the field of fluid-driven compressions, its application to membrane filtration remains an interesting topic. In recent years, it has become increasingly easier to manufacture membranes with porosity gradients [71], which has motivated research into finding porosity gradients that maximise the efficiency of the filter [31]. So far, these works neglect the effects of fluid-driven compression, and so an interesting avenue for future research is to understand what the initial porosities of membranes should be so that it is optimal under compression.

We expect that research into the stochastic effects in membrane filtration will be increasingly important. For a start, the problem of not only determining the expected

value but also the distribution for the flux at a given time could be of interest in systems where the number of pores is small, such as microfluidic filters [35]. Another interesting avenue would be to extend the model to account for retention rates as well to evaluate which interconnected structures provide the lowest probabilities for unwanted particles such as viruses to pass through. The computational complexity of the stochastic model for interconnected membranes remains a problem for widespread adaptation. Given that it is increasingly possible to describe the microstructure of a membrane in high detail [3], research into homogenisation models, avenues for parallelisation, and deterministic–stochastic hybrid models could be of interest.

While the method discussed in Chapter 4 is probably not the most practicable way of determining a filtration law, it offers several other interesting viewpoints. First, it allows us to answer the forward problem of how a gravity current might spread in a porous medium, given that we have determined its filtration in a dead-end flow setup, and so this work could be of interest in the spreading of reactive fluids in porous media [69]. Second, the work also serves as a reminder to look for additional ways of determining filtration laws, be they optical or by using MRI to provide additional insights into membrane filtration that could ultimately lead to better membranes.

Data-driven modelling is an emerging field that we expect will have a big impact on the research in membrane filtration. With machine-learning models already being used to speed up the computation of complex fluid dynamics simulations [75], we expect that these approaches will be applied in membrane filtration as well, given the high-dimensionality of the input data (feed composition, membrane material, applied pressures, etc.) and the relative wealth of experimental data. The downside of this black-box approach is that the associated uncertainties cannot be classified, and so we expect that tractable mathematical models will not only be needed to provide insights but also certainty.

Bibliography

[1] D. J. Acheson. *Elementary Fluid Dynamics*. Oxford Applied Mathematics and Computing Science Series. Clarendon Press, 1990.

[2] J. M. Acton, H. E. Huppert, and M. Grae Worster. Two-dimensional viscous gravity currents flowing over a deep porous medium. *Journal of Fluid Mechanics*, 440:359–380, 2001.

[3] P. Altschuh, Y. C. Yabansu, J. Hötzer, M. Selzer, B. Nestler, and S. R. Kalidindi. Data science approaches for microstructure quantification and feature identification in porous membranes. *Journal of Membrane Science*, 540:88–97, 2017.

[4] P. Apel. Track etching technique in membrane technology. *Radiation Measurements*, 34(1-6):559–566, 2001.

[5] D. G. Aronson. Regularity properties of flows through porous media. *SIAM Journal on Applied Mathematics*, 17(2):461–467, 1969.

[6] H. J. Arpe. *Ullmann's Encyclopedia of Industrial Chemistry, poly(vinyl esters) to reduction*. Ullmann's Encyclopedia of Industrial Chemistry. Wiley, 1993.

[7] L. F. Athy. Density, porosity, and compaction of sedimentary rocks. *AAPG Bulletin*, 14, 1930.

[8] K. Atsumi and T. Akiyama. A study of cake filtration - Formulation as a Stefan problem. *Journal of Chemical Engineering of Japan*, 8(6):487–492, 1975.

[9] D. M. Audet and A. C. Fowler. A mathematical model for compaction in sedimentary basins. *Geophysics Journal International*, 110:577–590, 1992.

[10] L. C. Auton and C. W. MacMinn. From arteries to boreholes: Steady-state response of a poroelastic cylinder to fluid injection. *Proceedings of the Royal Society A*, 473:20160753, 2017.

[11] P. Ball. Scale-up and scale-down of membrane-based separation processes. *Membrane Technology*, 117:10–13, 2000.

[12] R. S. Barhate and S. Ramakrishna. Nanofibrous filtering media: Filtration problems and solutions from tiny materials. *Journal of Membrane Science*, 296:1–8, 2007.

[13] S. I. Barry and G. K. Aldis. Comparison of models for flow induced deformation of soft biological tissue. *Journal of Biomechanics*, 23(7):647–654, 1990.

[14] G. K. Batchelor. *An Introduction to Fluid Dynamics*. Cambridge Mathematical Library. Cambridge University Press, 2000.

[15] B. Berkowitz, A. Cortis, M. Dentz, and H. Scher. Modeling non-Fickian transport in geological formations as a continuous time random walk. *Reviews of Geophysics*, 44(2005):1–49, 2006.

[16] Y. Bernabé, U. Mok, and B. Evans. Permeability-porosity relationships in rocks subjected to various evolution processes. *Pure and Applied Geophysics*, 160:937–960, 2003.

[17] Y. Bessiere, N. Abidine, and P. Bacchin. Low fouling conditions in dead-end filtration: Evidence for a critical filtered volume and interpretation using critical osmotic pressure. *Journal of Membrane Science*, 264:37–47, 2005.

[18] M. A. Biot. Theory of elasticity and consolidation for a porous anisotropic solid. *Journal of Applied Physics*, 26:182–185, 1955.

[19] G. R. Bolton, D. LaCasse, M. J. Lazzara, and R. Kuriyel. The fiber-coating model of biopharmaceutical depth filtration. *AIChE Journal*, 51(11):2978–2987, 2005.

[20] R. T. Bonnecaze, M. A. Hallworth, H. E. Huppert, and J. R. Lister. Axisymmetric particle-driven gravity currents. *Journal of Fluid Mechanics*, 294:93–121, 1995.

[21] W. R. Bowen and Q. Gan. Properties of microfiltration membranes: Flux loss during constant pressure permeation of bovine serum albumin. *Biotechnology and Bioengineering*, 38(7):688–696, 1991.

[22] F. Box. Personal communication.

[23] S. L. Brunton, J. L. Proctor, and J. N. Kutz. Discovering governing equations from data by sparse identification of nonlinear dynamical systems. *PNAS*, 113(15):3932–3937, 2016.

[24] M. A. Cacciuttolo, E. Shane, C. Oliver, and E. Tsao. Scale-up considerations for biotechnology-derived products. In M. Levin, editor, *Pharmaceutical Process Scale-Up*, Drugs and the Pharmaceutical Sciences, chapter 4. Taylor & Francis, 2001.

[25] C. Charcosset. Membrane processes in biotechnology: An overview. *Biotechnology Advances*, 24(5):482–492, 2006.

[26] E. Y. Chi, S. Krishnan, T. W. Randolph, and J. F. Carpenter. Physical stability of proteins in aqueous solution: Mechanism and driving forces in nonnative protein aggregation. *Pharmaceutical Research*, 20(9):1325–1336, 2003.

[27] M. Collins, H. Lari, S. Anderson, R. Leibnitz, A. Kumar, and R. Kuriyel. Investigating flow distribution and its effects on scale-up. *BioProcess International*, 7(9):46–52, 2009.

[28] B. P. Cook. Theory for particle settling and shear-induced migration in thin-film liquid flow. *Physical Review E*, 78:045303, 2008.

[29] O. Coussy. *Poromechanics*. Wiley, 2004.

[30] M. P. Dalwadi, M. Bruna, and I. M. Griffiths. A multiscale method to calculate filter blockage. *Journal of Fluid Mechanics*, 809:264–289, 2016.

[31] M. P. Dalwadi, I. M. Griffiths, and M. Bruna. Understanding how porosity gradients can make a better filter using homogenization theory. *Proceedings of the Royal Society A*, 471:20150464, 2015.

[32] A. B. de Haan and H. Bosch. *Industrial Separation Processes: Fundamentals*. De Gruyter Textbook. De Gruyter, 2013.

[33] R. de Lara and J. Benavente. Use of hydrodynamic and electrical measurements to determine protein fouling mechanisms for microfiltration membranes with different structures and materials. *Separation and Purification Technology*, 66(3):517–524, 2009.

[34] B. Ding, C. Li, M. Zhang, F. Ji, and X. Dong. Effects of pore size distribution and coordination number on the prediction of filtration coefficients for straining from percolation theory. *Chemical Engineering Science*, 127(July):40–51, 2015.

[35] E. Dressaire and A. Sauret. Clogging of microfluidic systems. *Soft Matter*, 13:37–48, 2016.

[36] C. Duclos-Orsello, W. Li, and C.-C. Ho. A three mechanism model to describe fouling of microfiltration membranes. *Journal of Membrane Science*, 280(1-2):856–866, 2006.

[37] C. M. Elliott, M. A. Herrero, J. R. King, and J. R. Ockendon. The Mesa problem: Diffusion patterns. *IMA Journal of Applied Mathematics*, 37:147–154, 1986.

[38] R. W. Field, D. Wu, J. A. Howell, and B. B. Gupta. Critical flux concept for microfiltration fouling. *Journal of Membrane Science*, 100(3):259–272, 1995.

[39] G. Foley. A review of factors affecting filter cake properties in dead-end microfiltration of microbial suspensions. *Journal of Membrane Science*, 274:38–46, 2006.

[40] J. M. Foster, C. P. Please, A. D. Fitt, and G. Richardson. The reversing of interfaces in slow diffusion processes with strong absorption. *SIAM Journal on Applied Mathematics*, 72(1):144–162, 2012.

[41] A. C. Fowler and X.-S. Yang. Fast and slow compaction in sedimentary basins. *SIAM Journal on Applied Mathematics*, 59(1):365–385, 1998.

[42] M. Gironès, R. G. H. Lammertink, and M. Wessling. Protein aggregate deposition and fouling reduction strategies with high-flux silicon nitride microsieves. *Journal of Membrane Science*, 273(1-2):68–76, 2006.

[43] J. Gratton and F. Minotti. Self-similar viscous gravity currents: Phase-plane formalism. *Journal of Fluid Mechanics*, 210, 1990.

[44] I. M. Griffiths, A. Kumar, and P. S. Stewart. A combined network model for membrane fouling. *Journal of Colloid and Interface Science*, 432:10–18, 2014.

[45] I. M. Griffiths, A. Kumar, and P. S. Stewart. Designing asymmetric multilayered membrane filters with improved performance. *Journal of Membrane Science*, 511:108–118, 2016.

[46] É. Guazzelli, J. F. Morris, and S. Pic. *A Physical Introduction to Suspension Dynamics*. Cambridge Texts in Applied Mathematics. Cambridge University Press, 2011.

[47] B. Guo, Z. Zheng, M. A. Celia, and H. A. Stone. Axisymmetric flows from fluid injection into a confined porous medium. *Physics of Fluids*, 28:022107, 2017.

[48] M. E. Gurtin and R. C. MacCamy. On the diffusion of biological populations. *Mathematical Biosciences*, 33:35–49, 1977.

[49] P. H. Hermans and H. L. Bredee. Principles of the mathematical treatment of constant-pressure filtration. *Journal of the Society of Chemical Industry*, 55:1–4, 1936.

[50] J. Hermia. Constant pressure blocking filtration laws - Application to power-law non-Newtonian fluids. *Institution of Chemical Engineers. Transactions*, 60(3):183–187, 1982.

[51] M. A. Herrero and J. L. Vazquez. The one-dimensional nonlinear heat equation with absorption: Regularity of solutions and interfaces. *SIAM Journal on Mathematical Analysis*, 18(1):149–167, 1987.

[52] J. G. Herterich, D. Vella, R. W. Field, N. P. Hankins, and I. M. Griffiths. Tailoring wall permeabilities for enhanced filtration. *Physics of Fluids*, 27:053102, 2015.

[53] J. G. Herterich, Q. Xu, R. W. Field, D. Vella, and I. M. Griffiths. Optimizing the operation of a direct-flow filtration device. *Journal of Engineering Mathematics*, 104:195–211, 2017.

[54] D. R. Hewitt, J. S. Nijjer, M. Grae Worster, and J. A. Neufeld. Flow-induced compaction of a deformable porous medium. *Physical Review E*, 93:023116, 2016.

[55] D. R. Hewitt, D. T. Paterson, N. J. Balmforth, and D. M. Martinez. Dewatering of fibre suspensions by pressure filtration. *Physics of Fluids*, 28:063304, 2016.

[56] C.-C. Ho and A. L. Zydney. Effect of membrane morphology on the initial rate of protein fouling during microfiltration. *Journal of Membrane Science*, 155(2):261–275, 1999.

[57] C.-C. Ho and A. L. Zydney. A combined pore blockage and cake filtration model for protein fouling during microfiltration. *Journal of Colloid and Interface Science*, 232(2):389–399, 2000.

[58] A. J. Hogg, M. A. Hallworth, and H. E. Huppert. On gravity currents driven by constant fluxes of saline and particle-laden fluid in the presence of a uniform flow. *Journal of Fluid Mechanics*, 539:349–385, 2005.

[59] P. Howell, G. Kozyreff, and J. Ockendon. *Applied Solid Mechanics*. Cambridge Texts in Applied Mathematics. Cambridge University Press, 2009.

[60] E. H. Hsu and L. T. Fan. Experimental study of deep bed filtration: A stochastic treatment. *AIChE Journal*, 30(2):267–273, 1984.

[61] H. E. Huppert. Propagation of two-dimensional and axisymmetric viscous gravity currents over a rigid horizontal surface. *Journal of Fluid Mechanics*, 121:43–58, 1982.

[62] H. E. Huppert. Gravity currents in nature and industry. In *15th Australasian Fluid Mechanics Conference*, 2004.

[63] H. E. Huppert and J. A. Neufeld. The fluid mechanics of carbon dioxide sequestration. *Annual Review of Fluid Mechanics*, 46:255–274, 2014.

[64] E. L. Ince. *Ordinary Differential Equations*. Dover Books on Mathematics. Dover Publications, 1956.

[65] E. Iritani and N. Katagiri. Developments of blocking filtration model in membrane filtration. *KONA Powder and Particle Journal*, 2016(33):179–202, 2016.

[66] E. Iritani, Y. Mukai, Y. Tanaka, and T. Murase. Flux decline behavior in dead-end microfiltration of protein solutions. *Journal of Membrane Science*, 103(1-2):181–191, 1995.

[67] E. Iritani, H. Sumi, and T. Murase. Analysis of filtration rate in clarification filtration of power-law non-Newtonian fluids-solids mixtures under constant pressure by stochastic model. *Journal of Chemical Engineering of Japan*, 24(5):581–586, 1991.

[68] T. Jiang, M. D. Kennedy, W. G. J. van der Meer, P. A. Vanrolleghem, and J. C. Schippers. The role of blocking and cake filtration in MBR fouling. *Desalination*, 157:335–343, 2003.

[69] P. B. Kelemen, J. Matter, E. E. Streit, J. F. Rudge, W. B. Curry, and J. Blusztajn. Rates and mechanisms of mineral carbonation in peridotite: Natural processes and recipes for enhanced, in situ CO2 capture and storage. *Annual Review of Earth and Planetary Sciences*, 39:545–576, 2011.

[70] A. Klenke. *Wahrscheinlichkeitstheorie*. Springer-Lehrbuch Masterclass. Springer Berlin Heidelberg, 2008.

[71] W. Kools. Method of manufacturing membranes and the resulting membranes, October 8 2009. US Patent App. 12/386,115.

[72] A. U. Krupp, I. M. Griffiths, and C. P. Please. Stochastic modelling of membrane filtration. *Proceedings of the Royal Society A*, 473:20160948, 2017.

[73] A. U. Krupp, C. P. Please, A. Kumar, and I. M. Griffiths. Scaling-up of multicapsule depth filtration systems by modeling flow and pressure distribution. *Separation and Purification Technology*, 172:350–356, 2017.

[74] S. M. Kumar and S. Roy. Filtration characteristics in dead-end microfiltration of living Saccharomyces cerevisiae cells by alumina membranes. *Desalination*, 229:348–361, 2008.

[75] L. Ladický, S. Jeong, B. Solenthaler, M. Pollefeys, and M. Gross. Data-driven fluid simulations using regression forests. *ACM Transactions on Graphics*, 34(6):1–9, 2015.

[76] K. A. Landman, L. R. White, and M. Eberl. Pressure filtration of flocculated suspensions. *AIChE Journal*, 41(7):1687–1700, 1995.

[77] M. E. Laska, R. P. Brooks, M. Gayton, and N. S. Pujar. Robust scale-up of dead end filtration: Impact of filter fouling mechanisms and flow distribution. *Biotechnology and Bioengineering*, 92(3):308–320, 2005.

[78] K. P. Lee, T. C. Arnot, and D. Mattia. A review of reverse osmosis membrane materials for desalination - Development to date and future potential. *Journal of Membrane Science*, 370(1-2):1–22, 2011.

[79] F. Li, Q. Tian, B. Yang, L. Wu, and C. Deng. Effect of polyvinyl alcohol addition to model extracellular polymeric substances (EPS) on membrane filtration performance. *Desalination*, 286:34–40, 2012.

[80] J. Li, R. D. Sanderson, G. Y. Chai, and D. K. Hallbauer. Development of an ultrasonic technique for in situ investigating the properties of deposited protein during crossflow ultrafiltration. *Journal of Colloid and Interface Science*, 284:228–238, 2005.

[81] J. Ling, R. Jones, and J. Templeton. Machine learning strategies for systems with invariance properties. *Journal of Computational Physics*, 318:22–35, 2016.

[82] Y. Liu, Z. Zheng, and H. A. Stone. The influence of capillary effects on the drainage of a viscous gravity current into a deep porous medium. *Journal of Fluid Mechanics*, 817:514–559, 2017.

[83] C. W. MacMinn, E. R. Dufresne, and J. S. Wettlaufer. Large deformations of a soft porous material. *Physical Review Applied*, 5:044020, 2016.

[84] T. Maxworthy. Gravity currents with variable inflow. *Journal of Fluid Mechanics*, 128:247–257, 1983.

[85] L. McDowell-Boyer, J. R. Hunt, and N. Sitar. Particle transport through porous media. *Water Resources Research*, 22(13):1901–1921, 1986.

[86] S. Mondal and S. De. Generalized criteria for identification of fouling mechanism under steady state membrane filtration. *Journal of Membrane Science*, 344(1-2):6–13, 2009.

[87] M. Mulder. *Basic Principles of Membrane Technology*. Springer, 1996.

[88] P. J. Murray, C. M. Edwards, M. J. Tindall, and P. K. Maini. From a discrete to a continuum model of cell dynamics in one dimension. *Physical Review E*, 80:031912, 2009.

[89] R. Nassar, S. T. Chou, and L. T. Fan. Modelling and simulation of deep-bed filtration: A stochastic compartmental model. *Chemical Engineering Science*, 41(8):2017–2027, 1986.

[90] J. A. Neufeld, D. Vella, H. E. Huppert, and J. R. Lister. Leakage from gravity currents in a porous medium. Part 1. A localized sink. *Journal of Fluid Mechanics*, 666:391–413, 2011.

[91] K. N. Nordstrom, E. Verneuil, W. G. Ellenbroek, T. C. Lubensky, J. P. Gollub, and D. J. Durian. Centrifugal compression of soft particle packings: Theory and experiment. *Physical Review E*, 82:041403, 2010.

[92] J. Olivier, J. Vaxelaire, and E. Vorobiev. Modelling of cake filtration: An overview. *Separation Science and Technology*, 42(8):1667–1700, 2007.

[93] K. H. Parker, R. V. Mehta, and C. G. Caro. Steady flow in porous, elastically deformable materials. *Journal of Applied Mechanics*, 54:794–800, 1987.

[94] L. E. Payne. *Improperly posed problems in partial differential equations*. CBMS-NSF Regional Conference Series in Applied Mathematics. Society for Industrial and Applied Mathematics, 1975.

[95] S. S. Pegler, H. E. Huppert, and J. A. Neufeld. Fluid injection into a confined porous layer. *Journal of Fluid Mechanics*, 745:592–620, 2014.

[96] C. Pirat, A. Naso, J.-L. Meunier, P. Maissa, and C. Mathis. Transition to spatiotemporal chaos in a two-dimensional hydrodynamic system. *Physical Review Letters*, 94:134502, 2005.

[97] D. Pritchard, A. W. Woods, and A. J. Hogg. On the slow draining of a gravity current moving through a layered permeable medium. *Journal of Fluid Mechanics*, 444:23–47, 2001.

[98] M. Rahimi, S. S. Madaeni, M. Abolhasani, and A. A. Alsairafi. CFD and experimental studies of fouling of a microfiltration membrane. *Chemical Engineering and Processing: Process Intensification*, 48:1405–1413, 2009.

[99] P. Rajniak, S. C. Tsinontides, D. Pham, W. A. Hunke, S. D. Reynolds, and R. T. Chern. Sterilizing filtration - Principles and practice for successful scale-up to manufacturing. *Journal of Membrane Science*, 325(1):223–237, 2008.

[100] B. V. Ramarao and C. Tien. Approximate analysis of fine-particle retention in the cake filtration of suspensions. *Industrial & Engineering Chemistry Research*, 44:1424–1432, 2005.

[101] S. Ripperger, W. Gösele, C. Alt, and T. Loewe. *Filtration, 1. Fundamentals*. Wiley-VCH Verlag GmbH & Co. KGaA, 2000.

[102] P. Sanaei and L. J. Cummings. Flow and fouling in membrane filters: Effects of membrane morphology. *Journal of Fluid Mechanics*, 818:744–771, 2017.

[103] P. Sanaei, G. W. Richardson, T. Witelski, and L. J. Cummings. Flow and fouling in a pleated membrane filter. *Journal of Fluid Mechanics*, 795:36–59, 2016.

[104] R. Sayag and J. A. Neufeld. Propagation of viscous currents on a porous substrate with finite capillary entry pressure. *Journal of Fluid Mechanics*, 801:65–90, 2016.

[105] A. Shapiro, P. G. Bedrikovetsky, A. Santos, and O. O. Medvedev. A stochastic model for filtration of particulate suspensions with incomplete pore plugging. *Transport in Porous Media*, 67(1):135–164, 2007.

[106] J. A. Sherrat and J. D. Murray. Models of epidermal wound healing. *Proceedings of the Royal Society B*, 241:29–36, 1990.

[107] S. E. Shreve. *Stochastic Calculus for Finance*. 2004.

[108] J. E. Simpson. Gravity currents in the laboratory, atmosphere, and ocean. *Annual Review of Fluid Mechanics*, (14):213–234, 1982.

[109] D. E. Smiles. A theory of constant pressure filtration. *Chemical Engineering Science*, 25:985–996, 1970.

[110] J. L. Sommer and A. Mortensen. Forced unidirectional infiltration of deformable porous media. *Journal of Fluid Mechanics*, 311:193–217, 1996.

[111] P. B. Sørensen, P. Moldrup, and J. AA. Hansen. Filtration and expression of compressible cakes. *Chemical Engineering Science*, 51(6):967–979, 1996.

[112] M. J. Spannuth, J. A. Neufeld, J. S. Wettlaufer, and M. Grae Worster. Axisymmetric viscous gravity currents flowing over a porous medium. *Journal of Fluid Mechanics*, 622:135–144, 2009.

[113] L. A. Spielman. Particle capture from low-speed laminar flows. *Annual Review of Fluid Mechanics*, 9:297–319, 1977.

[114] S. Tarafdar, A. Dey, and B. S. Gupta. A multiple state stochastic model for deep-bed filtration. *Chemical Engineering Technology*, 15:44–50, 1992.

[115] K. Terzaghi. *Erdbaumechanik auf bodenphysikalischer Grundlage. - Leipzig (usw.), Deuticke 1925. XV, 399 S.* F. Deuticke, 1925.

[116] N. Tufenkji and M. Elimelech. Deviation from the classical colloid filtration theory in the presence of repulsive DLVO interactions. *Langmuir*, 20(25):10818–10828, 2004.

[117] R. Van Reis and A. Zydney. Membrane separations in biotechnology. *Current Opinion in Biotechnology*, 12(2):208–211, 2001.

[118] R. van Reis and A. Zydney. Bioprocess membrane technology. *Journal of Membrane Science*, 297:16–50, 2007.

[119] J. L. Vazquez. *The Porous Medium Equation: Mathematical Theory*. Oxford Mathematical Monographs. Clarendon Press, 2007.

[120] D. Vella and H. E. Huppert. Gravity currents in a porous medium at an inclined plane. *Journal of Fluid Mechanics*, 555:353–362, 2006.

[121] D. Vella, J. A. Neufeld, H. E. Huppert, and J. R. Lister. Leakage from gravity currents in a porous medium. Part 2. A line sink. *Journal of Fluid Mechanics*, 666:414–427, 2011.

[122] H. Ye, R. J. Beamish, S. M. Glaser, S. C. H. Grant, C.-h. Hsieh, L. J. Richards, J. T. Schnute, and G. Sugihara. Equation-free mechanistic ecosystem forecasting using empirical dynamic modeling. *PNAS*, 112(13):1569–1576, 2015.

[123] T.-H. Young, L.-P. Cheng, D.-J. Lin, L. Fane, and W.-Y. Chuang. Mechanisms of PVDF membrane formation by immersion-precipitation in soft (1-octanol) and harsh (water) nonsolvents. *Polymer*, 40:5315–5323, 1999.

[124] H. Yuan, A. Shapiro, Z. You, and A. Badalyan. Estimating filtration coefficients for straining from percolation and random walk theories. *Chemical Engineering Journal*, 210:63–73, 2012.

[125] Z. Zheng, I. M. Griffiths, and H. A. Stone. Propagation of a viscous thin film over an elastic membrane. *Journal of Fluid Mechanics*, 784:443–464, 2015.

[126] Z. Zheng, S. Shin, and H. A. Stone. Converging gravity currents over a permeable substrate. *Journal of Fluid Mechanics*, 778:669–690, 2015.

[127] M. Zlokarnik. Dimensional analysis and scale-up in theory and industrial application. In M. Levin, editor, *Pharmaceutical Process Scale-Up*, Drugs and the Pharmaceutical Sciences, chapter 1. Taylor & Francis, 2001.